PAUL SCHERRER INSTITUT

PSI

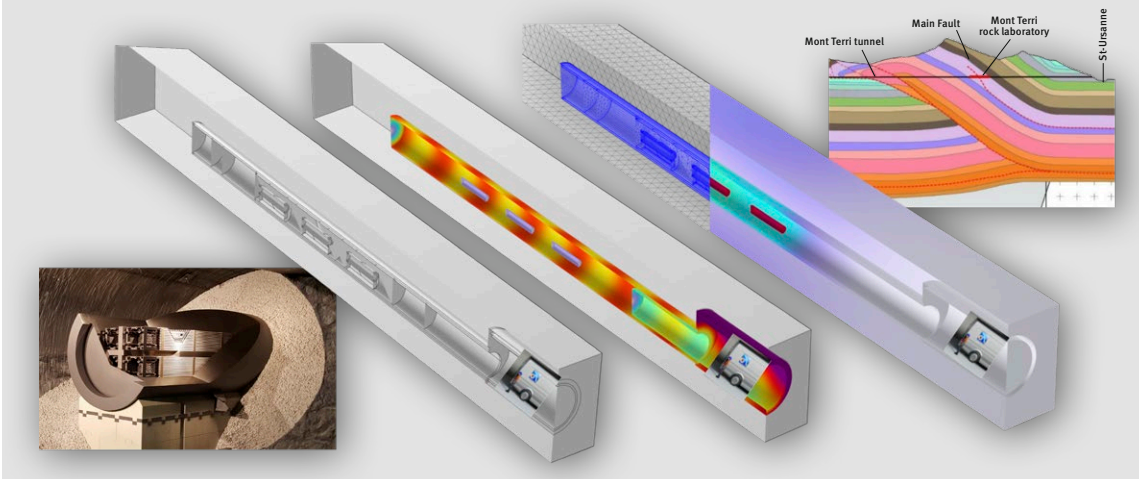

Progress Report 2023

Laboratory for Waste Management :: Nuclear Energy and Safety Department

Cover
3D Numerical modelling of thermal pulse in FE experiment at the Mont Terri Rock Laboratory using physics informed Machine Learning approach. See Chapter 2 for further details.

PAUL SCHERRER INSTITUT

Progress Report 2023

Laboratory for Waste Management
Nuclear Energy and Safety Department

See also our web-page
http://www.psi.ch/les/

Preface

The mission of the Laboratory for Waste Management (LES) is to carry out a comprehensive research and development (R&D) programme in support of Swiss radioactive waste disposal options. In particular, LES maintains and further develops the world-leading expertise in repository geochemistry, radionuclide migration, and design optimisation of engineered barrier systems based on experimental studies and numerical simulations.

The laboratory serves an important national role by supporting the Swiss Federal Government and Nagra in their tasks to safely dispose of radioactive wastes from medical, industrial and research applications as well as from nuclear power plants. The research activities of LES cover fundamental aspects of repository geochemistry, radionuclide transport and retardation in geological and technical barriers. The project portfolio of LES is a balanced combination of experimental activities conducted in dedicated laboratories for handling radioactive isotopes, field experiments and computer simulations. This work is directed towards repository implementation, and the results are used by Nagra in their comprehensive performance assessments studies. The finalisation of the documentation for the general licence application and the implementation of a repository in the next decades require expertise in model-based assessments of the *in situ* repository conditions for specific repository design. The long-term strategy of LES is thus to develop experimental and modelling expertise necessary for coupled description of relevant repository processes to assist safety- and economy-driven design optimisation of geological disposal in Switzerland.

Together with other laboratories in the Department of Nuclear Energy and Safety, LES maintains best practices and standards in laboratory management and data processing according to the ISO9001:2015 certified Integrated Quality Management System. This certification covers research and scientific services for agencies in the area of nuclear waste disposal and environmental sciences.

The present report summarises the research activities and results achieved in 2023. It gives a detailed overview of research projects, personnel management, national and international collaborations, and individual contributions achieved by scientists in the four research groups at PSI and the Mineralogy group at the University of Bern.

We gratefully acknowledge the support of our work by the PSI management, Nagra, and numerous research programmes within National and European funding agencies (e.g. SNSF, Swiss Nuclear, Eurad), as well as national and international industrial partners.

Table of Contents

1 OVERVIEW

Churakov S.V.

1.1 Introduction

This chapter provides an overall progress summary of activities in the Laboratory for Waste Management (LES) conducted from January 1st, 2023 to December 31th, 2023. The following chapters are organised thematically according to the six overarching research topics. These topics are multidisciplinary in nature and include contributions from different research groups at LES and the Mineralogy Group in the Institute of Geological Sciences at the University of Bern.

1.2 General

The site selection process for geological disposal of radioactive waste in Switzerland has entered its final stage. As announced at a media conference in September 2022, Nagra is planning to submit the general licence application (Rahmenbewilligungs-gesuch – RBG) for the geological disposal of Spent Fuel/High Level Waste (SF/HLW) and Low/Intermediate Level Waste (L/ILW) in the "Nördlich Lägern" region at the end of 2024. The proposal for the repository location is justified based on dedicated laboratory and field studies conducted in the period 2019-2022. The detailed analysis of geological and hydrological data, including diffusion and sorption measurements on the samples extracted from the site-specific drill cores, completed in 2023, provided a basis for site- and formation-specific databases of diffusion and sorption parameters used for the performance assessment calculations and demonstration of repository safety.

The development of the scientific databases used in the probabilistic and deterministic safety assessment was thus the major focus of the LES research program in 2023. The corresponding datasets were derived based on mechanistic sorption models, and the *in situ* and laboratory measurements served for model benchmarking and validation. This is an unique and explanatory approach in which scientific results are directly integrated in the safety assessment.

Following the period of very intensive site-specific explorations leading to the submission of the RBG, the preparation for implementation phase is expected to start. During the implementation phase, the underground exploration studies will be continued to confirm the findings obtained during the site exploration campaign. Further, the implementation phase foresees the optimisation of the repository design and includes a detailed specification of the materials to be used for the repository implementation. In this context, LES' national role is to maintain know-how in the field of waste disposal geochemistry and relevant aspects of material sciences. By the time of concluding the repository construction phase, some building materials currently considered as the basis for the repository design might not be conveniently available for economical or technological reasons. Accordingly, LES maintains knowhow and continues research on the main pillars of repository safety, namely the mechanistic description of radionuclide interaction with repository barriers and the processes in the repository near field. Present and future research activities focus on the chemical evolution of the repository near field, sorption competition phenomena, the behaviour of redox-sensitive radionuclides, the role of mineral surface-induced redox reactions, and the transfer of sorption models and data from dispersed to compacted systems. In preparation for the implementation phase, LES puts strong emphasis on the further development of advanced capabilities for reactive transport simulations. These capabilities are particularly important for understanding the long-term evolution of *in situ* repository conditions, and the interaction between repository barriers causing an alteration of their retention and transport properties. Such expertise is the essential basis for the optimisation of repository design.

Significant progress has been made in development of high fidelity simulations and the process-based multiscale modelling of complex physical phenomena in repository systems. Particularly challenging in this context is the parameter transfer between models at different scales, and efficient process coupling in complex 3D models. LES is taking a leading role in the development of so-called data driven surrogate models based on modern algorithms developed in the field of artificial intelligence and machine learning. In this context Deep Neural Networks (DNN) are applied for improvement of numerical performance of coupled codes by use of surrogate models for geochemical simulations and process parameter transfer. These developments are fostered through international collaboration supported with web based collaborative tools (https://www.geoml.ai) maintained by the LES team. Several demonstrations of surrogate model development and digital twins are provided at (https://www.geoml.eu).

Together with 52 other mandated research agencies, LES participates in the Joint European Research Proposal COFUND-EJP NFRP-2018-6: *"European Joint Research Programme in the management and disposal of radioactive waste Eurad"*. LES contributes to eight individual work packages (WPs):

FUTURE: Fundamental understanding of radionuclide retention (WP Lead and Task lead)

DONUT: Modelling of process couplings and numerical tools applied to performance assessment (Task co-Lead)

ACED: Assessment of chemical evolution of ILW and HLW disposal cells (Task Lead)

GAS: Mechanistic understanding of gas transport in clay materials (Contributor)

CORI: Cement organics radionuclide interactions (Contributor)

UMAN I+II: Uncertainty management multi-actor network (Contributor)

MAGIC: Chemo-Mechanical AGIng of Cementitious materials (Task Lead)

MODATS: Monitoring equipment and data treatment for safe repository (Contributor)

Within the EURATOM NFRP-2019-2020-10 RIA call, LES participates in the project *"Pre-disposal management of radioactive waste, PREDIS"*. This 4-year EU project was approved in spring 2020 and started on September 1st, 2020. The consortium includes 47 partners from 18 Member States. In this project, LES has a leading role in the development of a model based digital twin for the evolution of cementitious waste packages during extended intermediate storage scenarios.

The EURATOM projects PREDIS and Eurad are each entering their final project year. It is anticipated that European collaboration in waste disposal will continue under the umbrella of the joint program Eurad-II in the period 2024-2029. The corresponding project initiative was submitted by the programme coordinator, Andra, in November 2023.

The reactive transport codes developed at LES are versatile and applicable in broad cross-disciplinary applications. Complementary to geochemical applications, the codes are also used in collaborative research projects including thermohydraulic applications for nuclear reactors, desalination membranes, and pharmaceutical applications. Ongoing collaboration with GlaxoSmithKline Vaccines, Belgium (GSK), a science-led pharmaceutical company, focused on research, development and manufacturing of innovative pharmaceutical products has been continued. With support of Swissnuclear, further development of multiscale simulation codes for the modelling of boiling phenomena and crud formation in nuclear reactors is ongoing.

Several LES scientists have retired recently. To retain the core expertise of LES, and to more fully align the LES research portfolio to future oriented research questions, a number of both junior and senior experts have been recruited.

Dr. Romana Boiger has joined the Transport mechanisms group in February 2022. She is a mathematician by training, with several years of experience in application of machine learning and surrogate modelling for complex numerical simulations.

Prof. John Provis has taken the Group Leader position of the Cement Systems group in August 2023. He is an internationally recognised expert in materials science of alternative and conventional cements for construction and waste immobilisation (see section 4.6).

Dr. Anke Neumann has taken the Group Leader position of the Clay Sorption Mechanisms group in January 2024. She is a well-known expert in redox geochemistry of phyllosilicates, and pollutant dynamics in near environmental systems.

Scientific exchange is an essential component of research and development programmes. Particularly important in this context is the cross dissemination of knowledge in neighbouring fields. LES actively maintains collaborations with national and international research institutes in the field of waste management and environmental research. The main multi- and bi-lateral cooperations with external institutions and universities are summarised in Table 1.1.

Participation in international research projects and independent acquisition of project funding for PhD and postdoc projects is an essential driving force for developing state-of-the-art research capabilities, knowledge transfer and education of young generation scientists. Ongoing MSc/BSc/PhD projects and postdoc fellowships approved or started in 2023 at PSI and at the University of Bern are listed below, along with ongoing ones.

J. Ban (PhD student): *"Fe-doped hydrotalcites in Mg-cements"*. Start date: September 2023 (Funding: SNSF).

S. E. Bayram (PhD student): *"Synthesis and characterisation of metal-doped C-S-H phases"*. Start date: February 2023 (Funding: PSI-Research Grant).

M. Baur (MSc Student/UBern): *"Pore scale reactive transport modelling"*. Start date: August 2022.

P. Ingold (PhD student/UBern): *"Pollutant dynamics of bottom ash landfills"*. Start date: February 2021 (Funding: Industry).

A. Katheras (PhD student): "*Molecular scale understanding of Tc and Pu sorption by magnetite*". Start date: October 2020 (Funding: BMBF, Germany).

M. Mahrous (PhD student): *"Resolving dissolution-precipitation processes in porous media: Pore-scale Lattice Boltzmann modelling combined with synchrotron-based X-ray characterisation"*. Start date: March 2018 (Funding: SNSF).

S. Mingione (PhD Student/EMPA/UBern): "*Impact of process conditions on xonotlite quality and different components in xonotlite-based products on the high-T properties of these materials"*. Start date: October 2021 (Collaboration with EMPA; Funding: Industry).

H. Peng (PhD student): *"In situ chemical tomography and modelling of reactive transport processes in porous media"*. Start date: November 2021 (Funding: PSI-Cross).

Y. Qian (PhD student): *"Adsorption of redox sensitive radionuclides on Fe-bearing clay minerals"*. Start date: November 2019 (Funding: HORIZON 2020, Eurad).

Y. Zhe (visiting PhD Student): *"Redox sensitive sorption of Cr(VI) in clay-iron systems"*. Duration: December 2021 - October 2023 (Funding: NNSFC exchange program).

X. Wei (visiting PhD Student) *"Co-migration of clay colloids and radionuclides"*. Duration: September 2022 - August 2023 (Funding: Sino-Swiss-NNSFC exchange program).

V. Stotskyi (PhD student): *"Molecular scale understanding of competitive cation adsorption on swelling clay minerals"*. Start date: May 2021 (Funding: SNSF).

Dr. F. Di Lorenzo (postdoc): *"Molecular scale understanding of competitive cation adsorption on swelling clay minerals"*. Start date: June 2021 (Funding: SNSF).

Dr. G. Hu (postdoc): "*Data driven and physics based TH-model for repository near-field*". Start date: February 2022 (Funding: HORIZON 2020, Eurad).

Dr. A. Mokos (postdoc): *"Boiling crisis in nuclear reactor"* and "*Microstructural changes in cementitious materials*" Start date: March 2021 (Funding: Swissnuclear, EURAD-MAGIC).

Dr. A. Rajyaguru (postdoc): *"In situ chemical tomography and modelling of reactive transport processes in porous Media"*. Start date: August 2021 (Funding: PSI-Cross).

Dr. D. Wang (postdoc): *"Atomic-scale understanding of redox behaviors of Fe-doped hydrotalcites in Mg-cements"*. Start date: July 2023 (Funding: PSI-Fellow, EU).

Tab. 1.1: National and international co-operations.

Co-operations
National Nagra* (Major financial contribution, various technical working groups) Swissnuclear* (Reactor safety, material aging)
Multinational NEA Thermodynamic Database Project EURATOM HORIZON2020 (Eurad) EURATOM HORIZON2020 (PREDIS) Mont Terri Projects* (diffusion retardation, clay-cement interaction)
Universities University of Bern*, Switzerland (mineralogy, petrography, water chemistry, C-14 AMS, circular economy & environmental remediation) EPFL, Switzerland (cement systems) Université de Bourgogne, Dijon, France (molecular modelling in cement systems) ETH*, Zurich, Switzerland (GEMS; redox phenomena in cements) Hiroshima University, Japan (clay-cement interaction) University of Luxembourg* (porous media) Lanzhou University, School of Nuclear Engineering and Technology; Sino-French Institute of Nuclear Engineering and Technology; China Institute for Radiation Protection China (diffusion, retention) University of Leeds, UK (materials analysis) University of Sheffield, UK (cements science)
Research Centres CEA*, France (chemistry of near and far field) Eawag, Switzerland (Gas MS analytics) EMPA*, Switzerland (cement) IRE, HZDR*, Germany (XAS, TRLFS, atomistic modelling, reactive transport) INE, KIT*, Germany (near and far field; TRLFS) FZJ, Germany (sorption/diffusion of Ra, reactive transport, thermodynamics of solid solutions) SCK/CEN, Belgium (clay and cement systems) UFZ*, Germany (reactive transport, clay systems)
Industrial Partners GlaxoSmithKline* Nanocem Congineer Cosylab

**formal co-operation agreements*

Several PhD projects have successfully been completed in 2023:

P. Chen (PhD student): "*Technetium retention and migration in clay systems in presence of iron"*. Defence date October 2nd, 2023 (Funding: CNSF).

P. Krejci (PhD student): "*Diffusion of sorbed cations in clays: Development, improvement and application of new and existing models"*. Defence date March 3rd, 2023 (Funding: SNSF).

J. Owusu (PhD student): "*Numerical simulations of gas transport in argillaceous rocks: A molecular dynamics and pore-scale simulation study"*. Defence date August 14th, 2023 (Funding: EU-HORIZON 2020).

F. Sarraf (PhD Student/EMPA/UBern): "*Fabrication of dense polymer derived mullite ceramics by fused deposition modelling (FDM) method*". Defence date September 8th, 2023 (Collaboration with EMPA; Funding: SNSF).

The organisational chart of LES comprises four research groups located at PSI (Fig. 1.1). A fifth research group is located at the Institute of Geological Sciences (IfG) at the University of Bern. The mineralogy group at IfG is complementing the expertise in the field of mineral dissolution kinetics, structural studies of high porous materials and X-ray diffraction-based structure refinement and the geochemistry of conventional waste disposal. In particular, the mineralogy group hosts the Competence Centre for Secondary Raw Materials conducting applied research in the field of environmental geochemistry and secondary raw materials.

The LES annual report 2023 is organised in seven thematic research projects addressing specific aspects of repository geochemistry and radionuclide transport:

Chapter 2: Geochemical evolution of repository systems

Chapter 3: Retention and transport in clay systems

Chapter 4: Cementitious repository for radioactive waste

Chapter 5: Thermodynamic models and databases

Chapter 6: Landfills geochemistry and metal recovery

Chapter 7: Fundamental aspects of mineral reactivity and structural transformations

The following section provides an overview of LES activities contributing to the Sectoral Plan for Deep Geological Disposal, repository near and far field, reactivity of barrier systems and code benchmarking.

1.3 Sectoral plan for deep geological disposal

Diffusion measurements of tritiated water (HTO), $^{36}Cl^-$ and $^{22}Na^+$ tracers on > 130 samples from the deep-borehole drilling campaign (TBO) of Nagra in the Mesozoic sediments of Northern Switzerland were carried out at LES in order to provide a sound data basis for assessing mobility of dose-critical elements in relevant geological units. These data were used to develop an improved empirical relationship for description of effective diffusion coefficients as function of total clay content in the repository host rocks (see section 3.3).

1.4 Repository near field

1.4.1 Repository chemistry and thermodynamic databases

Thermodynamic data are the basis for geochemical modelling of repository *in situ* conditions, for pore waters, radionuclide solubility, sorption, and transport used in the safety assessments. The latest update of the PSI/Nagra chemical thermodynamic database was released in 2023. The database is used in defining the chemical systems for calculating solubility limits, sorption, diffusion, pore water models and host rock mineralogy for repository performance case evaluations. The thermodynamic database and the integral modelling tools are extended via participation in an internally consistent thermodynamic database Thereda that focuses on the solubility of radionuclides and other radioactive waste disposal relevant processes in highly saline systems. Both databases share the core datasets of standard state thermodynamic properties for elements and species related to low solubility solids. The Thereda basis set has been made compatible with the GEMS based framework, extending applicability of our modelling tools to the systems with saline pore water (see section 5.4)

Further collaboration in the Soreda project is aimed to develop a sorption database of radionuclides, relevant for the safety case of a deep geological repository, taking into account the minerals of argillaceous host rocks and buffer materials, such as clay minerals, quartz, carbonates and iron-bearing minerals. The most important and distinctive feature of the database is the physicochemical feasibility of its constituent sorption models due to the consideration of spectroscopically confirmed surface complexes (see section 5.5).

Cement-waste interactions, and internal degradation of cement, lead to chemical evolution of *in situ* conditions in a cementitious repository. These changes strongly affect the retention and transport of radionuclides. It is common practice to define four stages of cement evolution, characterised by the changes in pH and the stability of specific cement phases assembly. Accordingly, the retention capacity is influenced by the cement phase composition and stability across these stages. Based on literature and in-house experimental data (see section 4.4) an update of the cement sorption database for more than 30 elements, under oxidising and reducing conditions, and for all four stages of cement degradation under repository conditions has been conducted. The updated Nagra-PSI cement sorption database provides a substantial contribution to national and international efforts in the safety assessment of cementitious waste repositories (see section 4.2).

1.4.2 Clay systems

Most diffusion measurements for dose limiting radionuclides in rocks and bentonite are performed for standard temperature of 25 °C. Extrapolations to different temperatures are obtained using the Arrhenius equation. The applicability of such relationships in complex porous media has not been demonstrated experimentally. In charged porous media the diffusion of cations and anions is not only governed by well-studied geometric factors, but also by the thermodynamic partitioning of ionic species between the bulk aqueous phase and the Donnan volume near the basal clay surfaces. The exact dependence of these thermodynamic equilibria on temperature is unknown. To quantify these aspects, diffusion of $^{57}Co^{2+}$ in compacted illite model systems and samples from the TBO deep-drilling campaign has been investigated under elevated temperatures relevant to *in situ* repository conditions (see section 3.4).

Complexation of transition metals with organic ligands can substantially modify their sorption and mobility. Zn(II) is a good chemical analogue of divalent cationic transition metals for sorption/diffusion studies in soils and clays. The effect of the negatively charged organic ligand oxalate (Ox), and the uncharged ligand 1,10-phenanthroline (Phen), on Zn(II) mobility and retention in Na^+-conditioned illite du Puy (Na-IdP) was investigated by in-diffusion and batch sorption experiments. Increased ligand concentrations lead to lower mass transfer rates of Zn, but have different effects on the retention. The Zn sorption increases in presence of Phen but decreases in the presence of Ox, suggesting stronger complexation in the aqueous phase. The details of sorption mechanisms have been further revealed by X-ray absorption spectroscopy (XAS). It was found that Zn(II) forms ternary illite-Phen-Zn(II) and illite-Zn(II)-Ox complexes (see section 3.2).

Several studies of radionuclide retention and transport in clays and argillaceous materials are performed in the framework of the EURAD programme WP FUTURE. The investigations include the effect of cation loading

on anion accessible porosity, redox controlled uptake of Tc and Se by Fe bearing clay minerals, and sorption reversibility of transition metals on the edges of clay minerals (see section 3.5).

Experimental and theoretical studies of Ni^{2+} and Lu^{3+} uptake on synthetic saponite are conducted to improve molecular scale understanding of competitive cation adsorption on phyllosilicates. Synthetic Mg-saponite, used as the reference model in the study, belongs to the family of trioctahedral smectites. The combination of ab initio molecular simulations and XAS spectroscopy provides detailed information about the thermodynamics and geometry of surface complexes and can be used for improvement of mechanistic sorption model for transition metals on 2:1 smectites (see section 3.6).

Significant quantities of gas are expected to emerge in a repository, either resulting from corrosion of metallic materials or due to degradation of organic waste compounds. Diffusive transport of gaseous molecules in engineered barrier materials and host rocks is one of the most important parameters controlling the gas pressure build up and saturation state of the repository nearfield. Molecular diffusion of gas in saturated and partially swelling clays is investigated by theoretical atomistic simulations within the EURAD WP-GAS. Combining the theoretical results and experimental observations, a generic equation predicting gas diffusivity in real clay rock was formulated. Further effect of gas saturation on swelling behaviour of bentonite was evaluated (see section 2.6).

The development of an advanced model for diffusion of aqueous species (water tracers, anions, cations) in clays, taking into account the mobility of the adsorbed species, has been completed in the framework of an SNSF funded PhD project. The model accounts for diffusion and equilibrium partitioning of ions between three compartments including the bulk-like water in large pores, the diffuse double layer formed near charged surfaces of clay minerals, and the Stern layer comprising surface complexation of ions. Such a coupled consideration of sorption and diffusion allows description of the ionic strength dependence of differently charged cationic species in clay systems at different degrees of compaction (see section 2.3).

1.4.3 Cement systems

Corrosion of activated steel is a potentially important ^{14}C release mechanism in a repository. The ^{14}C mobility and retention depend strongly on the chemical properties of its carrier. Compound-specific ^{14}C release due to corrosion of activated steel in an alkaline environment is investigated in the framework of the international project LOMIR. This long-term corrosion experiment with an irradiated stainless steel sample from a nuclear reactor was set up in 2016. The gas and liquid phase are periodically sampled. The ultra-low concentrations of individual ^{14}C-compounds in both solution and gas phase are determined using compound-specific radiocarbon analysis based on chromatographic separation techniques combined with accelerator mass spectrometry (AMS) measurements and determination of total organic and inorganic carbon (TOC and TIC respectively). A complete mass balance of the ^{14}C in the experiment could thus be calculated after each sampling. After 2470 days of corrosion under anoxic alkaline conditions, a total of 0.003 % of the initial ^{14}C inventory has been released to the solution and gas phases. Several ^{14}C-bearing low molecular weight molecules including carbonates (25%, $^{14}CO_3^{2-}$) and five different ^{14}C-bearing carbonic acids (75%): formic acid, acetic acid, oxalic acid, malonic acid, and lactic acid, are quantified in the liquid phase. The $^{14}CH_4$ is measured to be the dominant ^{14}C-containing species in the gas phase. The experiment is continuing to confirm the long term ^{14}C-release rate (see section 4.3).

In the framework of the EURAD project MAGIC, LES and Empa are performing chemo- mechanical characterisation of cement samples undergoing laboratory-accelerated degradation due to interactions with Opalinus clay pore water. A key goal of this study is to provide quantitative information on the time dependence of poro-mechanical evolution, as well as chemical and microstructural transformation under conditions relevant to the Swiss geological repository. The non-destructive sample characterisation includes ultrasonic measurements of elastic properties, X-ray tomography, and diffusion experiments with non-reactive tracers. Post mortem analysis includes chemical characterisation and inspection of the microstructure by SEM with EDX mapping. The experimental data obtained in this study are used for calibration and testing of pore scale microstructure evolution models (see section 4.5).

To assess the interplay of microstructure evolution and mechanical properties of cement phase under chemical perturbations research groups from LES, SCK CEN and CNRS work jointly on multiscale modelling of cement degradation. Pore scale lattice Boltzmann simulations are applied to investigate the chemical degradation and microstructure evolution of cement paste due to cement carbonation. The obtained temporal microstructural evolution is the basis for assessment of mechanical properties based on multi-scale homogenisation. The numerical homogenisation approach is further benchmarked versus analytical models (see section 2.5).

In collaboration with the HOLCIM Foundation, the reaction process of alkali-silica reaction (ASR) is

investigated by ab initio molecular dynamics. The modelling is applied to reveal the ASR dissolution-precipitation mechanism at an atomistic scale, and to reveal the factors controlling the ASR swelling (see section 7.5).

1.4.4 Interface processes

Corrosion of steel under reducing conditions typical of an underground repository leads to formation of nanoparticulate magnetite (Fe_3O_4). Such magnetite nanoparticles can provide an important contribution on redox mediated uptake of redox sensitive radionuclides in the repository near field. Particularly important for such processes is the information on redox active iron on the mineral surface. So, surface structure and stability of magnetite nanoparticles were investigated by ab initio simulation. In the framework of an international project on retention of radionuclides by minerals, the surface stability and the speciation of magnetite is investigated by ab initio calculations. The modelling reveals stability fields for various surface terminations as a function of pH and Eh conditions. The obtained surface stability phase diagrams are the basis for further investigations of radionuclide absorption on the magnetite surface (see section 7.4).

A cement based liner is used to support the mechanical stability of repository tunnels. This liner is expected to react with bentonite and surrounding host rocks. The reference scenarios are based on simulations for ambient conditions. However, the *in situ* temperature in the repository is expected to be in the range 40-60°C. Moreover, significantly higher temperatures are anticipated in the early stage of repository evolution due to the initial thermal pulse caused by decay heat in SF/HLW. In order to assess the effects of temperature, kinetic constraints and porosity coupling (on solute transport), several model variants were evaluated for which the temperature pulse, kinetic control of mineral reactions or coupling of mineral volume changes to porosity were selectively switched off and on in a systematic manner. This allowed comparing the results from the reference model considering reactive processes at constant temperatures. Among other factors, higher temperature accelerate the kinetically controlled reactions of the silica aggregate and leads to faster degradation of the liner, which can occur within the first hundred years. The rapid degradation of cementitious materials lowers the pH of the porewater to below pH 10 and reduces the pH difference to adjacent clay media. The decreased pH contrast between clay and cement materials slows down or even suppresses clay/cement interaction and related porosity changes (see section 2.2).

1.5 Model development and code benchmarking, thermodynamic databases, and Digital Twins

To assess the safety of a deep geological repository for radioactive waste in clay rock, solid-liquid distribution coefficients (K_d values) for various radionuclides, rock composition and pore water chemistry are needed. The ClaySor module is the GEMS implementation of 2SPNE SC/CE sorption model used for derivation of the sorption database for the safety analysis. Recently the model was extended to take into account the parameter uncertainty estimates and made consistent with the latest update of the thermodynamic database (see section 5.2).

Radionuclide transport in porous clay media is a complex phenomenon taking into account both retention and mobility of radionuclides. In the previous years, the development of the sorption and diffusion databases was conducted using different and partially inconsistent models. The major challenges are related to the consistent description of electrostatics phenomena in the so called diffuse double layer. Whereas retention of radionuclides is mainly controlled by immobile surface complexes, the diffusive transport is mainly affected by ion enrichment or depletion in the diffuse double layer. The development in last years led to a "quantum leap" in a consistent description of sorption and diffusion. Implementation of the ClaySorDif model in GEMS is a self-consistent unification of classical 2SPNE SC/CE with the electrostatic surface mobility model used for interpretation of diffusion experiments. The new implementation of ClaySorDiff in GEMS allows for consistent modelling of sorption and diffusion using one and the same sorption and thermodynamic data set. This is a unique development revolutionising the future interpretation of experimental data (see section 5.3).

High-fidelity 3D numerical simulations of coupled phenomena are time-consuming. For such systems, inverse modelling of the experiments is particularly challenging since several hundreds of physical simulations might be needed. In the framework of the PSI-funded CROSS project *"In situ 4D micro X-ray chemical imaging and a digital twin of miniaturized counter-diffusion experiments: co-precipitation of metals with carbonates in porous media"*, digital twins of laboratory experiments with increased realism are developed to accompany and augment the experimental observations as well as to measure specific quantities of interest via inverse modelling. A surrogate of a capillary cross diffusion experiment has been developed and used for the investigation of transport parameters by reactive transport modelling. (see section 2.4).

The application fields of artificial intelligence (AI) and machine learning methods (ML) are growing at a very fast pace. Several numerical studies heavily rely on AI to improve the performance of numerical simulations and assist the data analysis.

Convolutional neural networks were applied to assess the lithology and mineral content of the drill cores from deep exploration campaign solely from analysis of photographic core images, aiming to support and expedite the subsurface geological exploration. The AI-based algorithm performs with 97% accuracy on classification of cores with respect to the corresponding geological formations. Prediction of the mineralogical content provides the same level of accuracy as the dedicated regression models (Multimin) based on the multidimensional core log data analysis (see section 2.8).

In the context of nuclear energy production, waste management and nuclear safeguards, the precise quantification of spent nuclear fuel inventory is important for safety, efficiency and sustainability. Physics Informed Neural Networks were considered to solve the Bateman equation describing the evolution of isotope inventory in nuclear fuel assembly. Numerical simulation shows an excellent agreement with physics-based simulations and measurements. Considering an order of magnitude reduction of computational costs, the employment of surrogate models offers a promising avenue to enhance computational efficiency in assessing nuclear fuel behaviour and associated risks (see section 2.10).

The models and codes developed at LES are highly versatile and find further applications in different neighbouring fields. Pore Scale Lattice Boltzmann simulations are used in computational fluid dynamics applications to assess boiling flow in fuel-assembly affected by crud or multiphase fluid flow in desalination membranes (see section 2.9).

In the framework of Eurad project MODATS, data driven numerical models are developed and validated to assist the monitoring and long-term assessment of Thermal-Hydraulic conditions in the HLW repository near field. The sensors data from the Full Emplacement experiment at the Mont Terri underground research laboratory are used to develop a Digital Twin for a set of HLW canisters disposed in Opalinus Clay. The model combines the 3D system information coming from the sensor and physical simulations of heat transport (see section 2.11).

1.6 Environmental impact of conventional waste disposal, secondary raw material recycling and fundamental aspects of mineral reactivity

The research of the Mineralogy Group at the University of Bern covers fundamental and applied aspects of mineral dissolution and precipitation, chemical factors of crystal structure stability and temperature driven phase transitions in minerals. The dedicated laboratories operated by the Mineralogy Group are equipped with powder and single crystal diffractometers for structural studies of minerals, and with an atomic force microscope for *in situ* characterisation of mineral surfaces. The experimental studies are widely supported by modelling activities.

The Competence Centre for Secondary Raw Materials (German: Fachstelle Sekundärrohstoffe, FSSR) is embedded in the Mineralogy group and conducts applied research in the field of environmental geochemistry and secondary raw materials. The core competencies of the FSSR include the topics of recycling management and disposal quality of conventional non-radioactive waste. The sustainable implementation of recycling technologies is waste type specific and requires detailed knowledge of chemical and phase composition of the materials, their long-term leaching behaviour and process couplings controlling material degradation. To close material cycles and conserve primary raw material reserves, new approaches and processes are needed to use secondary raw materials on a larger scale and in new areas.

In Switzerland, the recovery of non-ferrous metals from bottom ash of municipal solid waste incineration prior to landfilling has been legally required for more than 10 years according to the state of the art technology. Today's processing technologies and the resulting metal recovery have reached a high level of efficiency. In the near future, decisions on the implementation of specific bottom ash processing technologies will be made in several waste incineration plants. To support the decision making process with operational performance data, a comparative study of the different processing technologies was carried out on behalf of the Swiss Federal Office for the Environment. The comparison includes treatment technologies from dry and wet discharge with different process stages: conventional technologies such as crushing, grinding, eddy current separators and density separation tables as well as electrodynamic processes for the liberation of metals from the bottom ash components (see section 6.2).

Every year, Switzerland produces approximately ca. 80-90 Mio. tonnes of mineral waste. Recycling of mineral wastes can contribute to a substantial reduction of carbon footprint in construction materials. Calcium oxide rich mineral wastes such as wood- and paper ash, as well as construction/demolition wastes with high cement paste content, offer the greatest potential to substitution of limestone in clinker production. However, both wood- and paper ash are enormously reactive and can hydrate within a very short time and carbonate via CO_2-uptake from the air. They should therefore be considered as *CO_2-neutral* raw materials. *CO_2-neutral* raw materials are materials which are largely *CO_2-free* at initial stage, but incorporate CO_2 from the air within short timescales during their use, storage and processing into an alternative raw material. Proper accounting of *climate-neutral* CO_2 in clinker production on the raw material side would create additional incentives to use secondary CaO-sources in clinker production and could represent a decisive turning point in the utilisation of mineral waste (see section 6.3).

The Swiss waste disposal ordinance defines an aftercare period of 50 years for the monitoring of landfill sites for bottom ash. Therefore, reliable predictions for long term behaviour of Type D landfills where bottom ash is deposited are challenging. A large body of field characterisation and monitoring data has been collected and used to develop hydro-geochemical model of landfill site evolution. The model takes into account chemical equilibrium between domains with distinct hydrodynamic transport properties, and semi-quantitatively explains the chemical and hydraulic behaviour of landfill discharge systems (see section 6.4).

1.7 Fundamental aspect of structural transformations in minerals

Several studies address temperature-dependent structural transformations and dehydration processes in microporous minerals. In collaboration with colleagues from the University of Silesia in Poland, a new phase in the apatite mineral group has been discovered and refined (see section 7.2). In collaboration with the University of Urbino Carlo Bo, the dehydration and hydration behaviour of a natural zeolite with YUG framework type was investigated as a function of water vapour pressure and temperature by in situ single crystal X-ray diffraction (see section 7.3).

Dynamic tilting in perovskite structures is responsible for their peculiar physical properties, such as superconductivity, ferroelectricity and photo-activity. An extensive analysis of the structural data for perovskites reported in recent scientific literature has been conducted to facilitate identification of the dynamic tiling phenomena. To simplify structural analysis of such systems, space groups for simple perovskites ABX_3 with dynamical octahedral tilting have been derived (see section 7.6).

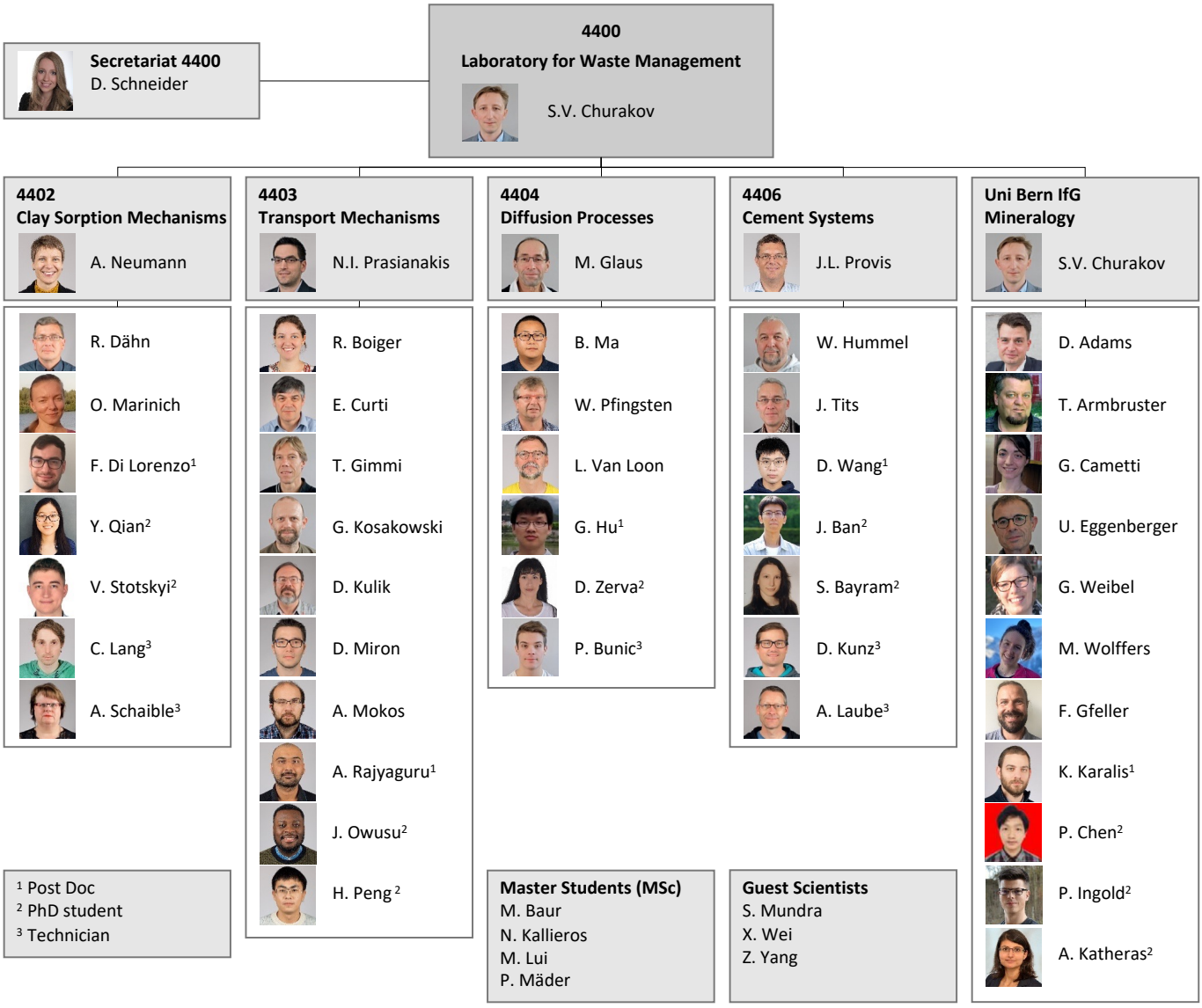

Fig. 1.1: Organisational chart of LES.

2 GEOCHEMICAL EVOLUTION OF REPOSITORY SYSTEMS

Prasianakis N.I., Churakov S.V., Curti E., Gimmi T., Kosakowski G., Kulik D., Pfingsten W., Boiger R., Miron D., Mokos A., Karalis K., Grolimund D. (PSD), Hu G. (postdoc), Rajyaguru A. (postdoc), Owusu J. (PhD student), Peng H. (PhD student), Ballester I. (bachelor thesis)

2.1 Introduction

Cross scale thermal-hydraulic-mechanics-chemistry (THMC)-numerical models and simulation tools are essential for describing the long-term evolution of multi-barrier repository systems and in geotechnical engineering. Such models are the basis for the safety assessment and cross comparison of different repository designs conducted as a part of the site selection process in the Sectoral Plan for Deep Geological Disposal (SGT) Stage 3, and the following general license application.

The research activities described in this chapter cover three main topics relevant for repository near field evolution: 1) numerical modelling of the evolution of the technical barriers and their respective interfaces, e.g. cement evolution and cement-clay interaction; 2) fundamental understanding of transport and retention of radionuclides through multiscale modelling and upscaling techniques; 3) the benchmarking of coupled codes as well as the development and coupling of state-of-the-art reactive transport codes with thermodynamic modelling tools and databases.

LES is participating in several EURAD Work Packages (WP). Within the EURAD WP DONUT several multiscale codes and their couplings are developed. One of the striking developments is the growing application of artificial intelligence (AI) and machine learning methods (ML). The EURAD community is using ML for a) accelerating numerical simulations, b) improving the efficiency of multiscale and multiphysics couplings, c) uncertainty quantification and sensitivity analysis. Benchmarking is currently performed to test a variety of ML techniques relevant to geochemical and reactive transport simulations in the framework of radioactive waste disposal, aiming at providing basic guidelines about the benefits and limitations of using ML techniques (Lead: N.I. Prasianakis). Joint efforts across more than ten research organisations across Europe are ongoing. Three major geochemical solvers (PHREEQC, ORCHESTRA and GEMS) are applied to model the chemical systems of interest. Results from most of the partners have been produced and the first comparison allows assessment of the efficiency of each machine learning method. During the benchmarking, a concise framework for producing training datasets as well as for measuring the accuracy of the ML methods has been developed. The benchmarking is currently in its final stage.

Within the EURAD WP GAS, molecular dynamics simulations and pore scale modelling are used to investigate gas transport in clays. The combination of modelling and analysis of the available data allows derivation of functional relationships for predicting macroscopic gas transport parameters in a broad range of *in situ* conditions (PhD project of Jerry Owusu). In EURAD WP ACED, the geochemical evolution of waste packages has been investigated, including the gas release due to waste degradation processes. Within the EURAD WP MODATS, sensor data from the Full Emplacement (FE) experiment (Mont Terri) are used to develop a digital twin for the FE experiment, while in the EURAD WP UMAN the near-field uncertainties associated with radioactive waste disposal and spent fuel, and how they relate to risk and safety, have been assessed. Finally, in the EURAD WP MAGIC the chemo-mechanical aging of cementitious materials is investigated.

Relevant to the evolution of a high level waste repository, a number of activities are focused on description of repository processes as part of documentation for the general license application of HLW repository. This included a synthesis report on vitrified waste degradation (Curti 2022), contributions to a comprehensive report on spent fuel dissolution (Johnson et al. 2023), and a report on the bentonite porewater chemistry (Curti 2023).

The CROSS project "*In situ* 4D micro-X-ray chemical imaging and a digital twin of miniaturized counter-diffusion experiments: co-precipitation of metals with carbonates in porous media" has continued in 2023. The overarching research goal of the project is to elucidate the role of trace metals (Ni, Zn, Pb) in polymorph stabilisation and growth kinetics of calcium carbonate in porous media (silica gel, mineral powders). The diffusion of solutes in microcapillaries has been experimentally investigated, and a digital twin of microfluidic diffusion experiments has been developed for a real time inverse-modelling based machine learning technique (PhD project of Haonan Peng).

Machine learning is playing an increasing role in various scientific projects. Transfer learning and convolutional neural networks have been applied for drill core lithology classification and mineral content regression. The produced tool aims to facilitate the

processing of the drill cores available from Nagra drilling campaigns and to support the upscaling of core data to the field scale. In another project, machine learning has been used to evaluate the spent nuclear fuel (SNF) inventory during nuclear reactor operation, which is important for safety, efficiency and sustainability. The decay heat was calculated using surrogate models and compared to full physical model results.

Several ongoing projects on multiscale multiphysics computational fluid dynamics (CFD) embark on the advanced modelling tools actively developed in LES. In the realms of a collaborative project with the Laboratory for scientific computing and modelling at PSI (LSM-PSI) and under the umbrella of the Swissnuclear funding agency through the project "*Numerical prediction of boiling crisis considering surface characteristics*", the fundamental understanding of boiling processes from atomistic to reactor scale is pursued. For the first time it was possible to simulate boiling processes within CRUDs and observe multiphase flow at the pore-level.

Finally, in 2023, work has continued on two industrial projects with the pharmaceutical company GlaxoSmithKline Vaccines, Belgium (GSK) (PI: N.I. Prasianakis). GSK is a science-led global healthcare company focused on the research, development and manufacturing of innovative pharmaceutical medicines, vaccines and consumer healthcare products. The project benefits from the in-house development of advanced multiscale simulation codes and machine learning relevant to accelerated computing and data analysis.

2.2 Reactive transport modelling of material interface evolution in the HLW near-field

Reactive transport calculations are used to study the evolution of clay and cement-based materials in the near-field of SF/HLW repository considering a thermal pulse from heat output of spent fuel canisters (Kosakowski, 2023). The models implement the near-field geometry and materials according to the updated repository dimensions foreseen for the general licence application as summarised in Curti et al. (2023) and shown in Fig. 2.1. Specifically, investigations include the chemical evolution of a cement-based tunnel support system, which comprises tubbing elements and an annular gap filling material, and its impact on the bentonite and the Opalinus Clay.

The modelling methodology is based on the approach used for reactive transport calculations reported in Cloet et al. (2018) for assessing the evolution of a cementitious backfill. All calculations are conducted with the OpenGeoSys-GEMS coupled code (Kosakowski & Watanabe, 2014). As in previous studies (Berner et al., 2013; Bradbury et al., 2014; Cloet et al., 2018), it is assumed that the solute/heat transport is largely dominated by diffusion in a fully saturated near-field; i.e. re-saturation of the near-field, advective transport of water in liquid (solutes and heat) and gaseous state are not included in the calculations.

The chemical system setup is based on that used in Cloet et al. (2018). Chemical evolution is modelled with GEMS3K using PSI/Nagra TDB (thermodynamic database) 12/07 (Thoenen et al., 2014), CEMDATA 18 (Lothenbach et al., 2019), crystalline C-S-H phases and other mineral phases imported from Thermoddem DB (Blanc et al., 2012) and a new ZEOLITE DB (Ma & Lothenbach, 2020, 2021). Kinetic data for dissolution/precipitation reactions were taken from the Thermoddem DB (Marty et al., 2015).

The models consider the temperature pulse caused by the decay of radionuclides within spent fuel canisters, which amounts to an initial heat output of 1500 W for a single canister. The temperature evolution calculated by Senger et al. (2014) at different points of a cross-section of the near-field were used as boundary conditions (e.g. boundary 1 in Fig. 2.1) in the heat transport calculations. An average temperature of 317 K (44.85 °C) was used as an initial condition, and the near-field was defined as the 50 m radius around the canister. The heat transport was coupled to solute transport via temperature-dependent diffusion coefficients. Temperature is considered for calculation of chemical equilibria and the kinetic control of mineral dissolution/precipitation.

In order to assess the effects of temperature, kinetic constraints and porosity coupling (on solute transport), several model variants were evaluated, in which temperature pulse, kinetic control of mineral reactions or coupling of mineral volume changes to porosity were selectively switched off and on in a systematic manner. This allowed comparison of the results from the reference model, considering reactive processes at constant temperatures.

Compared to former calculations at 298.15 K (25 °C) described in Bradbury et al. (2014) and Berner et al. (2013), the geochemical evolution of the near-field was accelerated when the base temperature for all model scenarios was increased to 317 K (44.85 °C). Diffusion coefficients and corresponding mass fluxes increase significantly at higher temperatures. In addition, kinetic precipitation/dissolution rates also increase strongly at higher temperatures. Fig. 2.2 shows a mineralogical profile across the near-field in the radial direction, calculated for the reference scenario that considers a temperature pulse, kinetic control of mineral reactions and back-coupling of transport to porosity changes.

In this setup, the retrograde solubility of carbonates with temperature induces a significant additional carbonate flux from the Opalinus Clay toward the near-field. As carbonate solubility is lowered with an increase in the pH, carbonate is precipitated at the high-pH front originating from the annulus grout. Due to the limited availability of free calcium in the Opalinus Clay, the carbonation front moves rapidly into the annulus grout, where calcium is easily leached from C-S-H and other cement phases, and calcite precipitated (Fig. 2.2). The dissolution of C-S-H phases also releases large amounts of silica, which precipitates as quartz in the model. As the dissolution of quartz is kinetically controlled, excess silica in the solution will be transported towards the Opalinus Clay.

In the long term, carbonates and, to a lesser degree, quartz accumulate near the annulus grout/Opalinus Clay interface. In addition, for the investigated reference system, the grout layer is completely altered (carbonated) within less than one thousand years.

Due to the increased temperatures, the internal degradation of cement materials by kinetically controlled silica aggregate dissolution is faster and can occur within the first hundred years. Fig. 2.3 shows the calculated time-dependent evolution of C-S-H composition for tubbing concrete in contact with the annulus grout as function of temperature and $Ca^{2+} + H^{+}$ activity. The arrows indicate the direction of evolution with time. Arrow A indicates an increase in temperature at early times that causes movement along phase boundaries, i.e. two phases co-exist in varying quantities. After the initial temperature increase, arrow B shows that the dissolution of siliceous aggregate changes the composition toward Si-rich C-S-H phases (low Ca/Si ratio). Once the C-S-H phases are in equilibrium with quartz, arrow C indicates movement of C-S-H composition along the C-S-H/quartz boundary according to the temperature (first increasing, and later decreasing).

The rapid degradation of cementitious materials lowers the pH of the porewater to below pH 10 and reduces the pH difference from adjacent clay media. The decreased pH contrast between clay and cement materials slows down or even suppresses clay/cement interaction and related porosity changes.

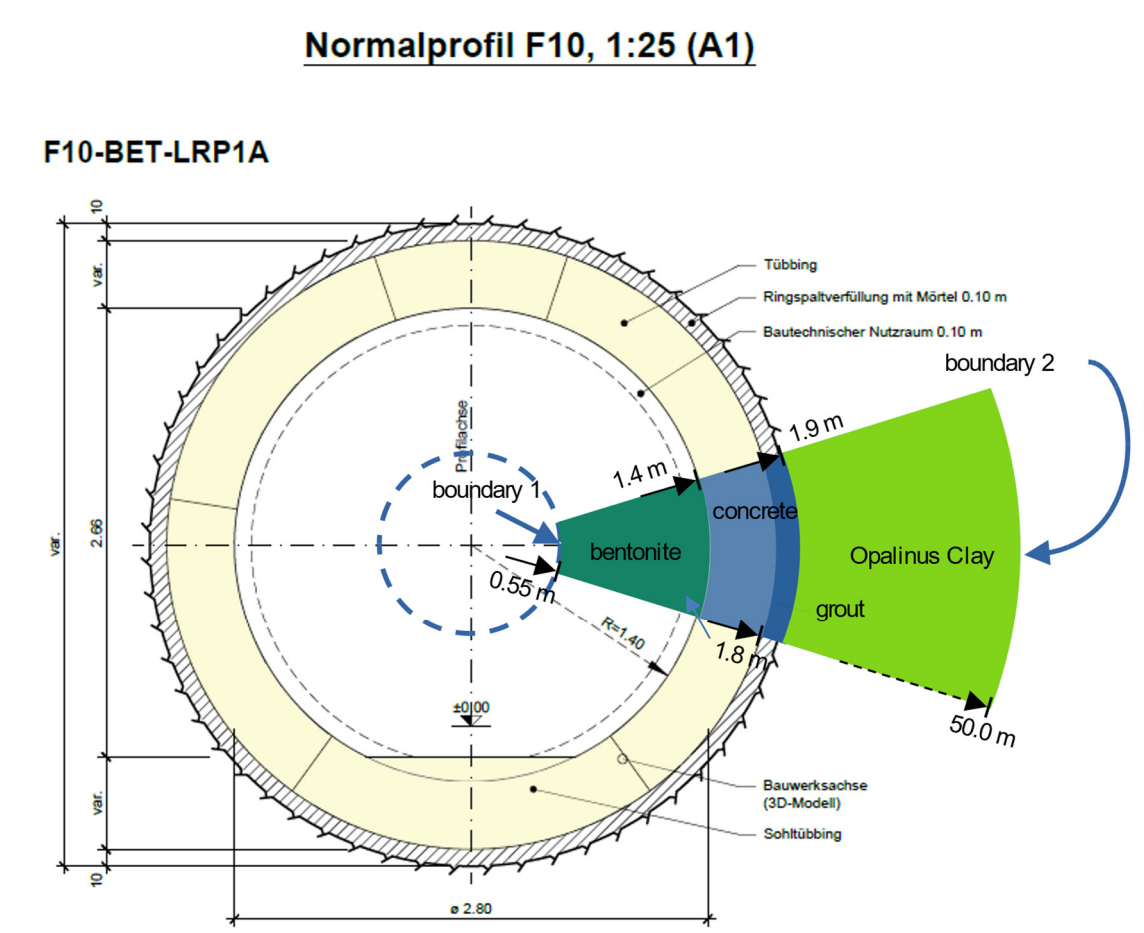

Fig. 2.1: HLW near-field dimensions and numerical representation. The size of the Opalinus Clay is not to scale compared to the near-field materials.

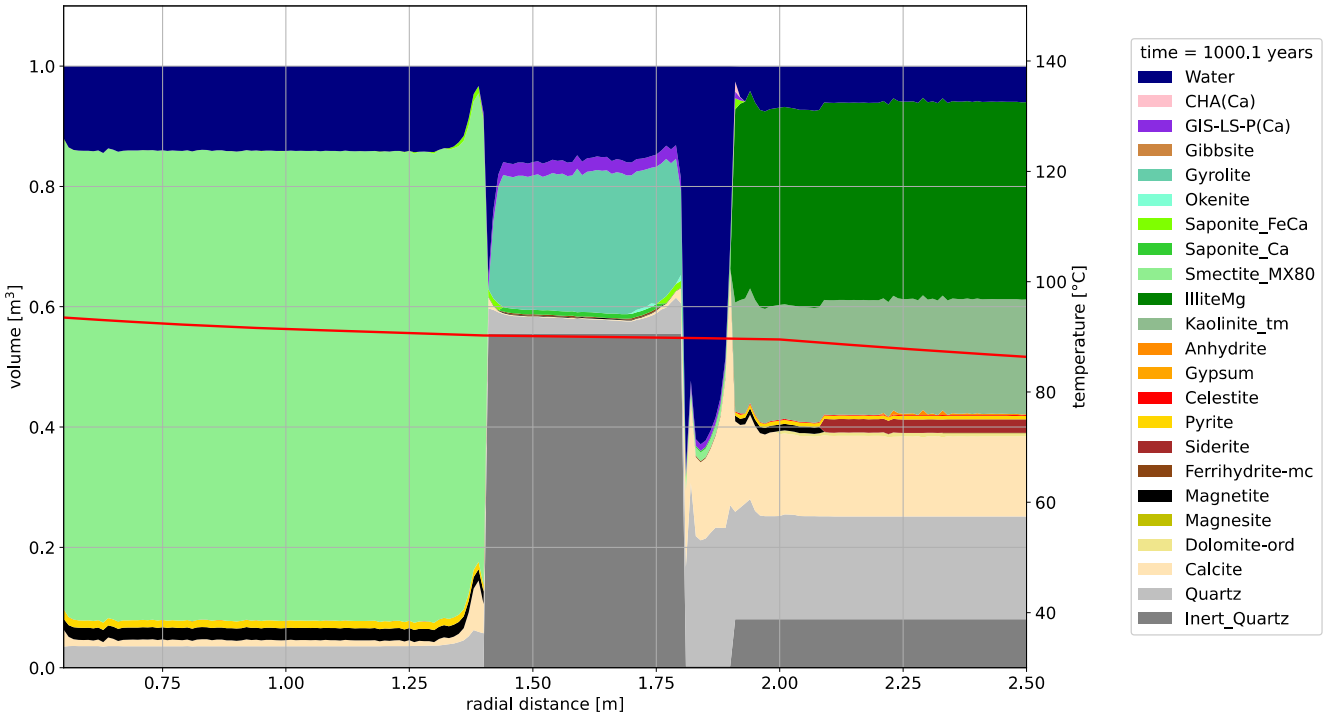

Fig. 2.2: Spatial mineralogical profile in volumetric units (left axis) for the reference model variant for HLW near-field with temperature increase, after 1000 years of simulation time. The red line denotes the temperature with values given in the right-hand vertical axis.

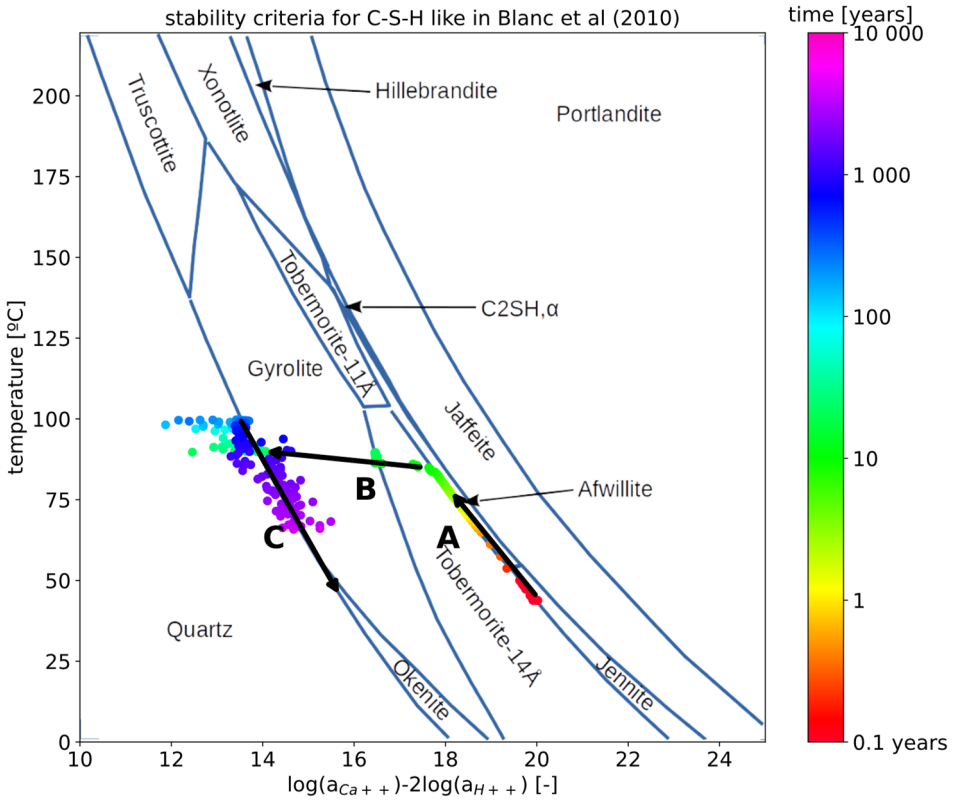

Fig. 2.3: Evolution of C-S-H composition in the reference model for tubbing concrete in contact with the annulus grout, depending on temperature and Ca^{2+} + H^{+} activity. For explanation of arrows A, B and C, see text.

2.3 Retention and transport in clay systems: diffusion modelling of cations, anions and neutral tracers through Opalinus Clay and bentonite

In his PhD thesis, Krejci (2023) has developed an advanced model for diffusion of differently charged ions (water tracers, anions, cations) in clays, taking into account the mobility of the adsorbed species. From previous studies (e.g., Glaus et al. 2021, Krejci et al. 2021), it became clear that the diffusion of cations and anions in clays under different conditions (e.g., porewater salinity, degree of compaction), especially Cs, cannot be described satisfactorily by a simple porewater diffusion model, nor by a so-called dual porosity model that considers diffusion in a diffuse or Donnan layer in addition to diffusion in the 'free' porewater. The advanced model (D-S-I model) considers diffusion in the 'free' porewater and a Donnan layer, and additionally in the Stern layer (a region near the surfaces where cations are more strongly and more specifically bound), and in interlayers.

The difficulty in applying such models lies mainly in the assignment of model parameters. For bentonite, a microstructure model for different dry densities was developed based on literature data (clay stack sizes, interlayer hydration states). The microstructure model provides the fractions of external porosity and interlayer porosity as a function of the bulk dry density of the bentonite, and also the distribution of average water layers (one, two or three) in interlayers that varies with the bulk dry density. Different local diffusion coefficients (diffusive mobilities) were attributed to the different pore environments, based on literature values from experiments and molecular dynamics simulations. For bentonite, the microstructure model and the transport parameters are well constrained. This is less so for Opalinus Clay, as this sedimentary rock is a complex mixture of different minerals with heterogeneities at different scales. The overall sorption of the D-S-I model was matched to published results of cation exchange models. Finally, for both materials, information from diffusion of a neutral tracer (HTO) and of an anion (Cl^-) had to be used. The HTO data were needed to define tortuosities, which were then equally applied to the cations. The Cl data were needed to quantify so-called interlayer-equivalent external pores (external pores with small widths).

The new D-S-I model with a single set of parameters led to, e.g., a satisfactory prediction of effective diffusion coefficients of Na, Sr and Cs in bentonite at three different dry densities (Fig. 2.4). Deviations from the experimental data are mostly small (except for Cs at the highest bulk dry density). The model is comparably robust with respect to the chosen parameters, as the default set of parameters (blue open symbols) and an alternative set of parameters (orange open symbols) lead to very similar results in most cases.

The D-S-I model allowed derivation of the relative contributions of different diffusion pathways for different cations. Fig. 2.5 illustrates that at the given densities of bentonite, the free porewater essentially does not contribute at all to the overall diffusion, and that diffusion through the interlayers and external interlayer-like pores mainly dominates, as expected. Stern layer diffusion is relevant for Cs and Sr, but less so for Na, while Donnan layer diffusion is not important for Cs in bentonite, and only of minor importance for Na and Sr. The situation is different for Opalinus Clay, for which data from Mont Terri samples at two different ionic strengths are compared (Fig. 2.6). Here, Donnan layer diffusion is the dominant pathway for Na and especially for Sr at both ionic strengths, while Stern-layer diffusion dominates for Cs and is important for Na, but less so for Sr. Because there is little smectite (in the form of illite/smectite mixed-layer minerals), the interlayer pathway is not relevant, but the

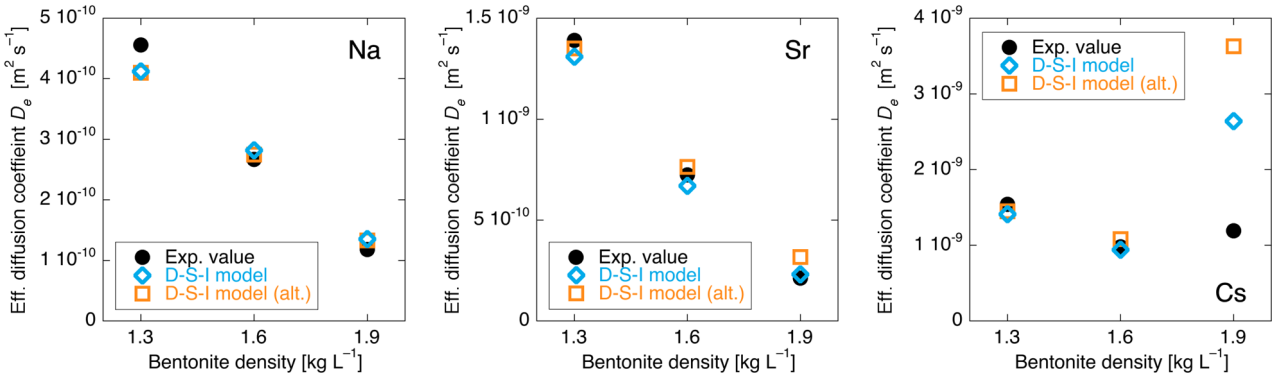

Fig. 2.4: Effective diffusion coefficients D_e in bentonite at three bulk dry densities predicted with the D-S-I model (blue and orange open symbols are the standard and alternative set of parameters, respectively) compared to those from experiments (black dots) for Na (left), Sr (middle) and Cs (right).

contribution of external interlayer-equivalent pores should not be neglected (and is especially relevant for anion exclusion). In Opalinus Clay, some diffusion in the 'free' porewater occurs for all ions; it becomes more important at higher ionic strengths, at the expense of diffusion in the Donnan layer.

2.4 Towards Experimental Digital Twins: An Integrated Physics-based Machine-Learning Framework for Inverse Modelling of Microfluidic Mass Transport Processes

In the framework of a PSI-funded CROSS project "In situ 4D micro-X-ray chemical imaging and a digital twin of miniaturized counter-diffusion experiments: co-precipitation of metals with carbonates in porous media", digital twins of laboratory experiments are developed. Experimental digital twins are numerical models of increased realism that can be used to accompany an experiment, augment the experimental observations, as well as measure specific quantities of interest via inverse modelling. Typically, high-fidelity 3D numerical simulations are time-consuming and cannot be used for the inverse modelling of these experiments, where several hundreds of physical simulations might be needed. To overcome this computational bottleneck and to achieve real-time simulations, a machine learning-based computational framework has been developed. A microfluidic channel diffusion experiment is considered as a showcase for the successful digital twin development. The experimental setup is composed of two reservoirs connected by a sub-millimetre capillary tube containing a high-porosity porous medium. In-situ chemical imaging via combined microscopic transmission, fluorescence, and diffraction at the Swiss Light Source (SLS, Paul Scherrer Institute) allowed determination of the concentrations of chemical species along the channel, at several time intervals, in a non-destructive way during the evolution of the experiment.

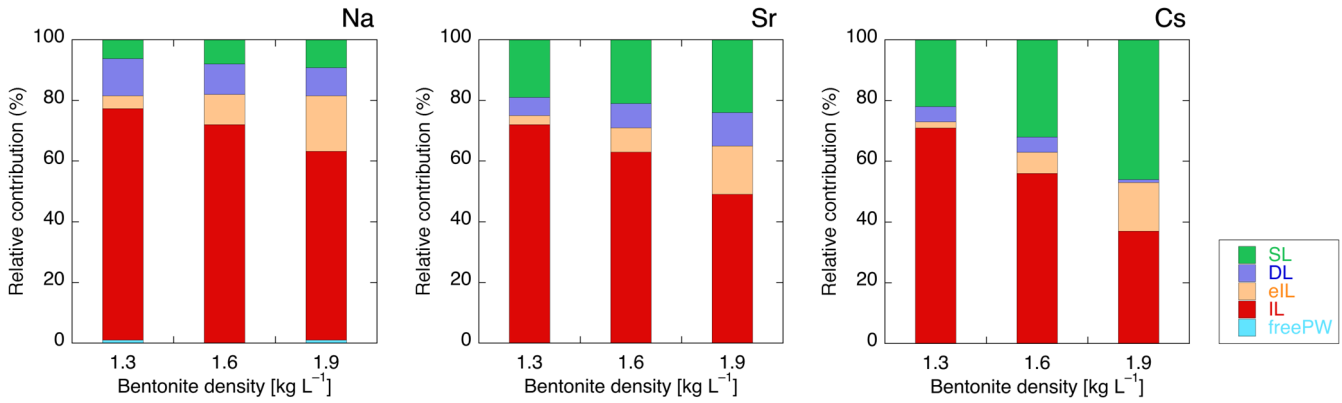

Fig. 2.5: Relative contributions of different diffusion pathways (freePW: free porewater, IL: interlayers, eIL: external interlayer-like, DL: Donnan layer, SL: Stern layer) on the effective diffusion coefficients D_e for Na (left), Sr (middle) and Cs (right) in bentonite at three different bulk dry densities.

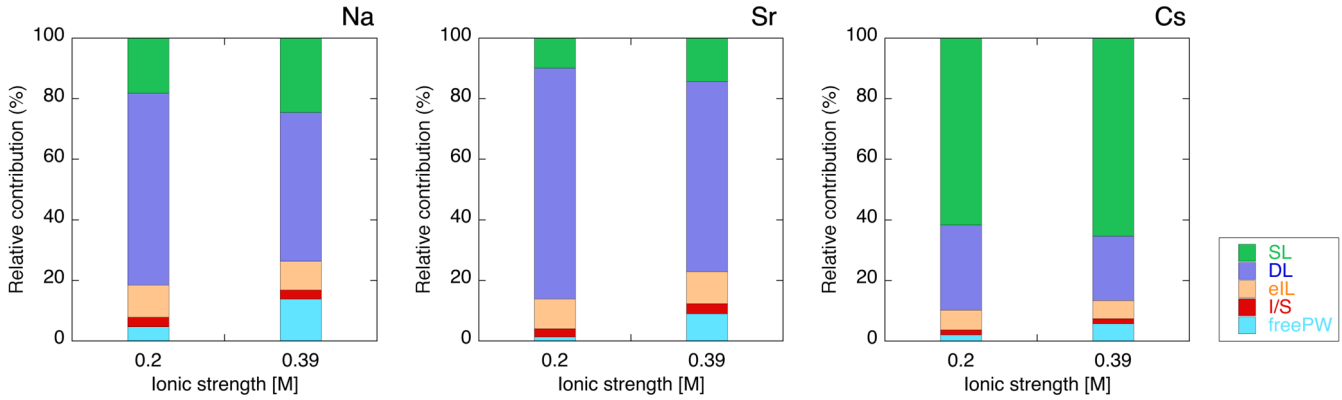

Fig. 2.6: Relative contributions of different diffusion pathways (freePW: free porewater, IL: interlayers, eIL: external interlayer-like, DL: Donnan layer, SL: Stern layer) on the effective diffusion coeffcients D_e for Na (left), Sr (middle) and Cs (right) in Opalinus Clay at two different ionic strengths.

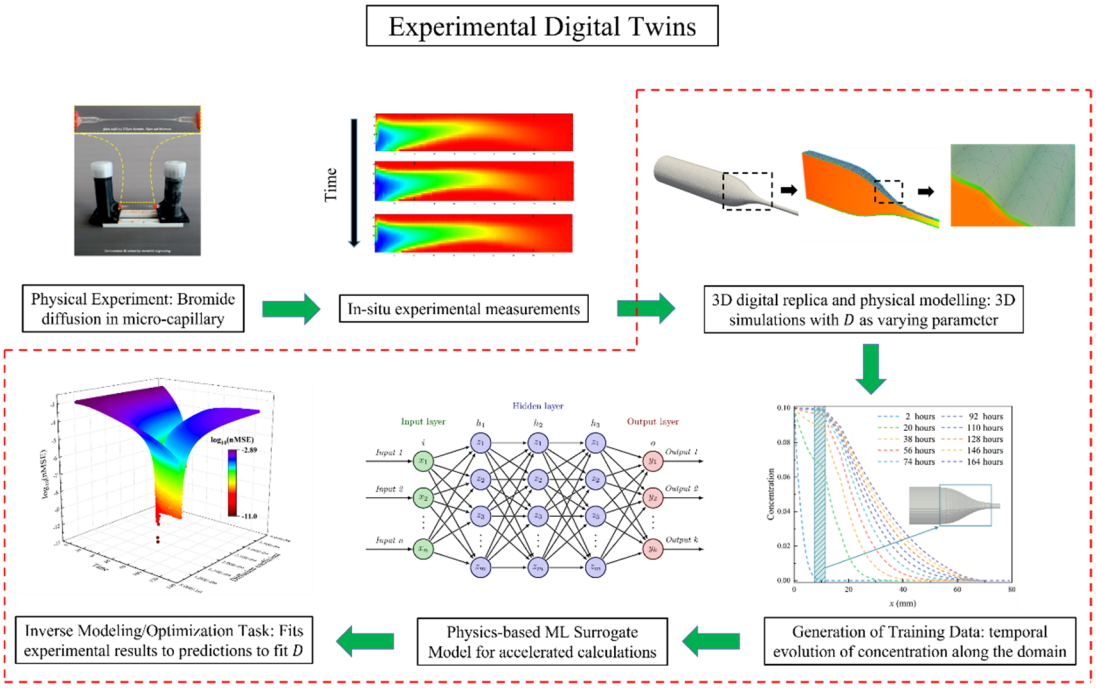

Fig. 2.7: The concept of the digital twin of a diffusion experiment is shown. Using machine learning, the inverse modelling and optimisation processes are accelerated by several orders of magnitude.

The trained model is used for inverse modelling based on the Global Optimisation methods and is tested against numerically modelled concentration profiles as well as real experimental data, to determine species diffusivity. A schematic of the concept is shown in Fig. 2.7. The first results suggest that the time to solution is accelerated by several orders of magnitude.

2.5 Pore level simulations of cementitious materials degradation.

Within the EURAD-MAGIC (Chemo-Mechanical AGIng of Cementitious materials) project, the degradation of cementitious materials is investigated. The chemical and structural evolution of cementitious materials at pore scale is simulated using an in-house 3D multi-component Lattice Boltzmann (LB) code. The modelling focuses on the kinetic dissolution of portlandite ($Ca(OH)_2$) at the pore-scale. The simulation code keeps track of both solid and liquid concentrations of Ca^{2+}, using a reaction equation to simulate the dissolution of Ca^{2+}. The reaction is calibrated with experimental results. Fig. 2.8 shows three snapshots from an extracted 2D slice out of the 3D computational domain, showing the gradual dissolution of portlandite. The model has been also extended to consider the dissolution to the C-S-H phases in cement. An innovative adaptive time-stepping technique has been implemented to provide a significant acceleration of the code. The mechanical alteration of the resulting degraded structures is then evaluated by the project partners SCK-CEN (Belgium) and LAM^3 (University of Lille, France) using numerical and analytical homogenisation techniques.

For the geochemical reactions, the code is coupled with an artificial neural network, also running on a GPU, which acts as a surrogate model for the native geochemical solvers. The NN has been trained on a dataset containing 90'000 equilibrated systems generated with the geochemical modelling software GEM-Selektor (Kulik, Wagner et al. 2013) to cover broad range of conditions relevant for C-S-H dissolution/precipitation reactions. The modelling results have been presented in the 2023 Goldschmidt conference (Mokos, Peng et al. 2023) and reported in EURAD MAGIC Deliverables D16.7 and D16.8.

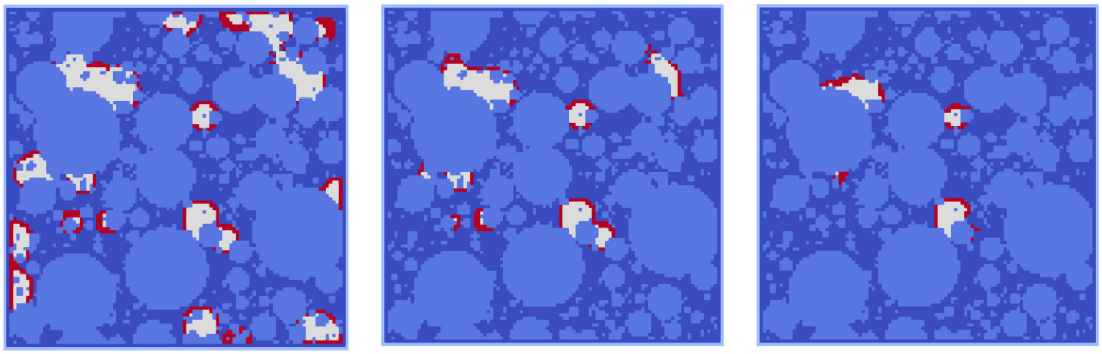

Fig. 2.8: Time series of 2D snapshots through the 3D simulation domain showing gradual portlandite dissolution (red and white nodes, with red currently dissolving). (left) is the beginning of the simulation, (centre) after 49.4%, and (right) after 76% of the portlandite solid nodes on the system have dissolved.

2.6 Determination of diffusion coefficients in smectite clays by combining molecular dynamics and pore scale simulations

Within the framework of EURAD WP GAS (Mechanistic understanding of GAS transport in clay materials), the mobility of gas molecules in geological barriers is investigated from an atomistic scale up to the pore level scale. The extremely low hydraulic conductivity of smectite-rich clay rocks makes them ideal as host rocks for nuclear waste repositories and gas storage. In these clays, the primary mechanism governing the movement of solutes and fluids is diffusion. Traditional methods for understanding solute transport oversimplify the intricate micro to nanoscale pore structure of clay by treating it as a continuous medium. To address the impact of molecular-scale interactions between solutes and mineral surfaces, as well as the complexity of the pore structure, extensive studies on water diffusion have been conducted. For this, large-scale molecular dynamics simulations have been combined with pore-scale random walk simulations. Initially, the local diffusion coefficients of water in smectite clays were determined through molecular dynamics simulations, considering the pore size and the influence of proximity to clay surfaces. These local diffusion coefficients were then applied to a pore-scale smectite clay model, where random walk simulations were conducted to calculate the effective diffusion coefficient. To validate the approach, the results of the pore-scale simulations were compared with those from large-scale molecular dynamics simulations using the same structural model. The findings emphasise the importance of considering local diffusivity within the representative elementary volume (REV) to gain a comprehensive understanding of transport mechanisms in porous materials, especially when dealing with chemically reactive surfaces like clay minerals (Owusu J., 2023b)

The combination of molecular dynamics, random walk and lattice Boltzmann simulations revealed the molecular mechanism of gas diffusion under partially and fully saturated conditions as function of pore size distribution and temperature (Owusu et al., 2022). Analysing the molecular scale diffusion trajectories of Ar, CH_4, CO_2, H_2 and He, it was possible to derive a general relationship between the molecular diffusivity, pore size and effective radius of gas molecules under saturated conditions (Fig. 2.9, left). Furthermore, taking into account geometric factors that were experimentally measured with HTO, it was possible to formulate a semi-empirical relationship for diffusivity of gases in clay rocks based on their effective radius or, if available, self-diffusion of a gas tracer in bulk water (Fig. 2.6, middle). Gas transport parameters in partially saturated clay pores, and the partition coefficient of gas molecules between low density, gas rich, and high density, water rich phases were derived by equilibrium and non-equilibrium molecular dynamics simulations (Owusu et al., 2023a). Interestingly, the presence of dissolved gas leads to an increase in the swelling pressure, caused by higher gas solubility under elevated pressure. For the first time, the nonequilibrium molecular dynamics simulations conducted for partially saturated clay pores provide the viscosity and slip length for advective transport in the gas phase, including surface absorbed water films, which are important parameters in macroscopic and pore scale gas transport modelling (Owusu et al., 2023a). Molecular scale insight into gas transport mechanisms reveals the conditions for the transition between molecular (bulk like) and Knudsen (surface collision controlled) diffusion of gas in confined space (Fig. 2.9, right).

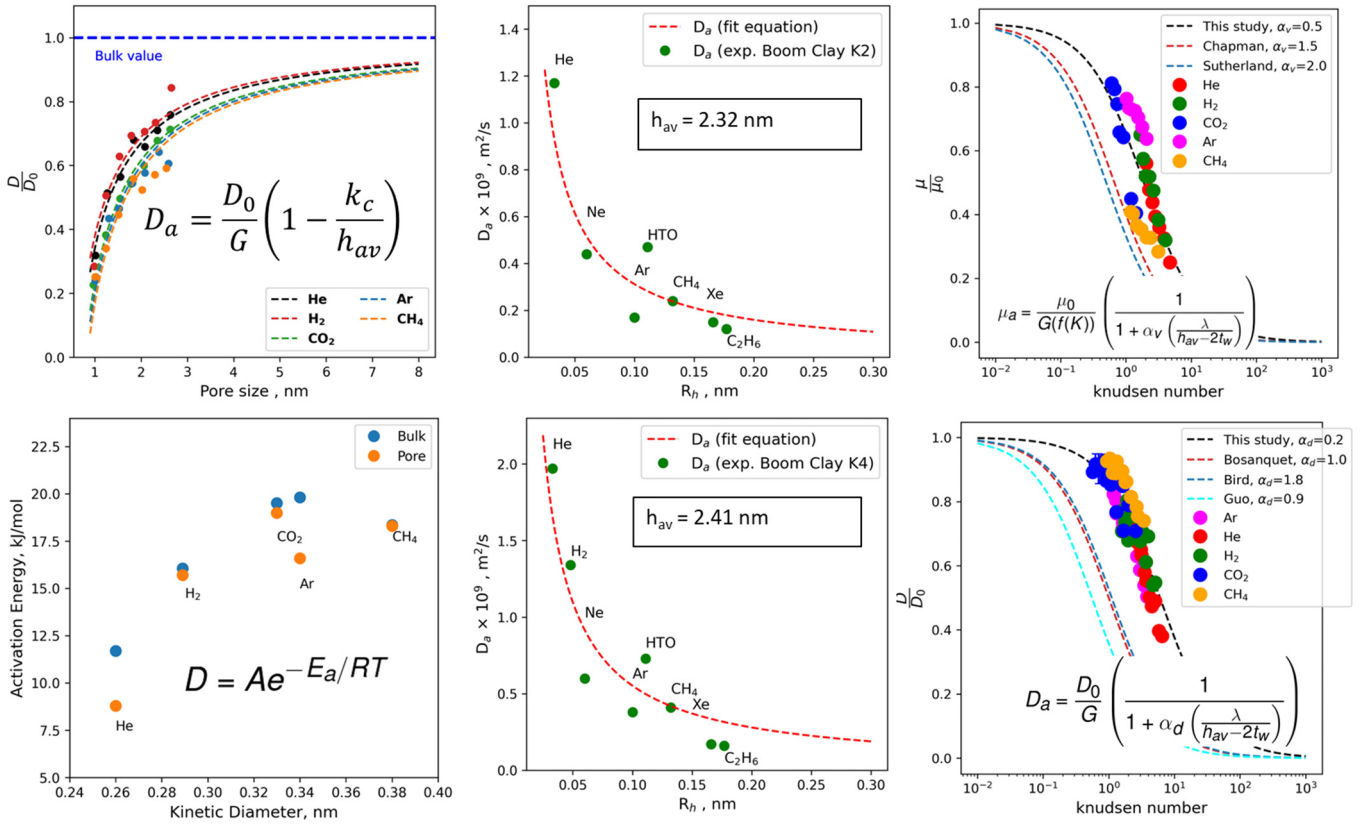

Fig. 2.9: Molecular scale and effective transport parameters of Ar, He H_2, CO_2 and CH_4 obtained by molecular dynamics simulations (Owusu et al., 2022; Owusu et al., 2023a), where D_0 - bulk diffusion coefficient, G - geometric factor, D_a - apparent diffusion coefficient, h_{av} - average pore width, K_c - surface interaction parameter, D_p - pore diffusion coefficient, a_d - Bosanquet parameter, t_w - water film thickness, μ_0 - bulk dynamic viscosity, μ_a - apparent dynamic viscosity, E_a and A – activation energy and preexponential factor, T – temperature, R – thermodynamic gas constant.

2.7 Machine learning assisted geochemical reactive transport modelling

Reactive transport simulations are an essential tool for modeling and hence understanding physical and chemical processes in geological systems, e.g. in deep geological waste repositories. However, a major computational bottleneck has persisted, stemming from the computation of geochemical equilibria, which often consumes 70-99% of the total simulation time. A coupling of a transport solver together with surrogate models, like neural networks (NN), to replace the geochemical solver during the simulation, showed great potential to reduce the overall computation time (see Prasianakis et al. (2020) and Hax Damiani (2021)). In a follow up work considering the dolomitization benchmark example, where a 1 M $MgCl_2$ solution flow was injected into a calcite column, the accuracy of the neural network (and hence also the accuracy of the reactive transport modeling framework using Fenics for the transport simulation and a neural network for the geochemical solver) have been improved. The comparison between a conventional reactive transport simulation using Fenics and Reaktoro versus the improved Fenics and NN framework can be seen in Fig. 2.10. The improved framework can be found on the updated geoml.ai (https://geoml.ai) webpage.

2.8 Machine learning based drill core lithology classification and mineral content regression

Exploration of underground formations is important for various industries, like mining, oil and gas, geothermal energy, but also for the deep geological disposal of nuclear waste. Conventionally, drill cores are extracted and extensive lab measurements together with geophysical borehole data are analysed. To speed up that process, the capability of machine learning methods for assessing the formation classes as well as the mineral content directly from photographs was tested. (Boiger et al. 2023, Ballester, Bachelor Thesis 2023). A data set from deep drilling (Trüllikon) in Switzerland, conducted by Nagra, was available, and consisted of 55 metres of photographed drill cores. These images were first preprocessed, i.e. colour and white balance corrected, cracks were detected, and the images were sliced into 1 cm thick sections perpendicular to the drill core cylindrical axis. Then, a

convolutional neural network (CNN) was trained for identifying six different formation classes, resulting in a model that showed an accuracy of 96%. This classification model was then further trained with MultiMin log analysis data via transfer learning, to assess the mineral content solely from drill core images. Fig. 2.11 shows the six different formations (column 1) over the depth, the prediction results of the classification model (column 2), the MultiMin log analysis data (column 3), and the (CNN) model predicted mineral content. The performance of the mineral content regression model was then tested with real XRD measurements and showed similar performance to the MultiMin log analysis data. This work underscores the potential of deep learning, specifically transfer learning, for extracting key petrophysical properties such as mineral content and formation classification directly from drill core images.

2.9 Multiphase modelling

2.9.1 Boiling flow simulation in fuel-assembly affected by CRUD

The project "Boiling flow simulation in fuel-assembly affected by CRUD" under the Swissnuclear funding agency and in collaboration with the Laboratory for Scientific Computing and Modelling at PSI (LSM-PSI) has been significantly advanced (A. Mokos). A new thermal model for the multi-GPU LB code using a second order central finite difference scheme has been developed and validated. The thermal model has been used, in conjunction with a newly developed multi-relaxation time (MRT) scheme, to simulate nucleate boiling flow within porous media corresponding to the CRUD microstructure. Fig. 2.12 shows two screenshots of a simulation, where an increased temperature has been applied to the centre of the domain, heating the water and causing it to evaporate. Vapour is then moving upwards under the influence of gravity towards the top boundary, where a bubble is seen detaching from the rough CRUD surface. These simulations shed light on the bubble birth mechanisms and the multiphase mixture circulation within the CRUD.

In addition, the multiphase LB model was used to study the multiphase transport through a porous medium due to capillary forces. Using the multi-GPU LB code, large scale 3D realistic porous structures were able to be simulated. In addition, the uptake of water was simulated for different saturation points of the water-vapour mixture. Fig. 2.13 shows a slice of a simulation on a computational grid consisting of 0.25 billion nodes, executed on 35 parallel GPUs. A water-vapour mixture with 25% saturation is entering through the bottom and slowly creeping upwards. A CRUD chimney structure is added on the right-hand side, showing an increased rate of penetration by the mixture.

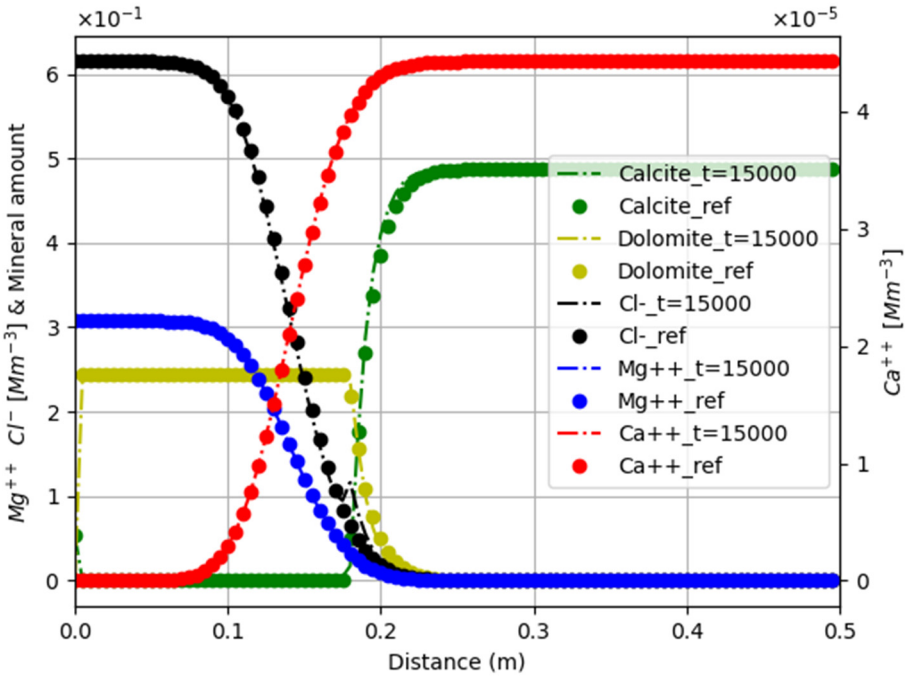

Fig. 2.10: Comparison of aqueous species during a dolomitisation process between simulations using FENICS-Reaktoro (circles, ref) and FENICS-NN (dash-dotted lines). The neural network is trained on data obtained from Reaktoro. The geochemical calculations within the FENICS-NN framework are accelerated by a few orders of magnitude.

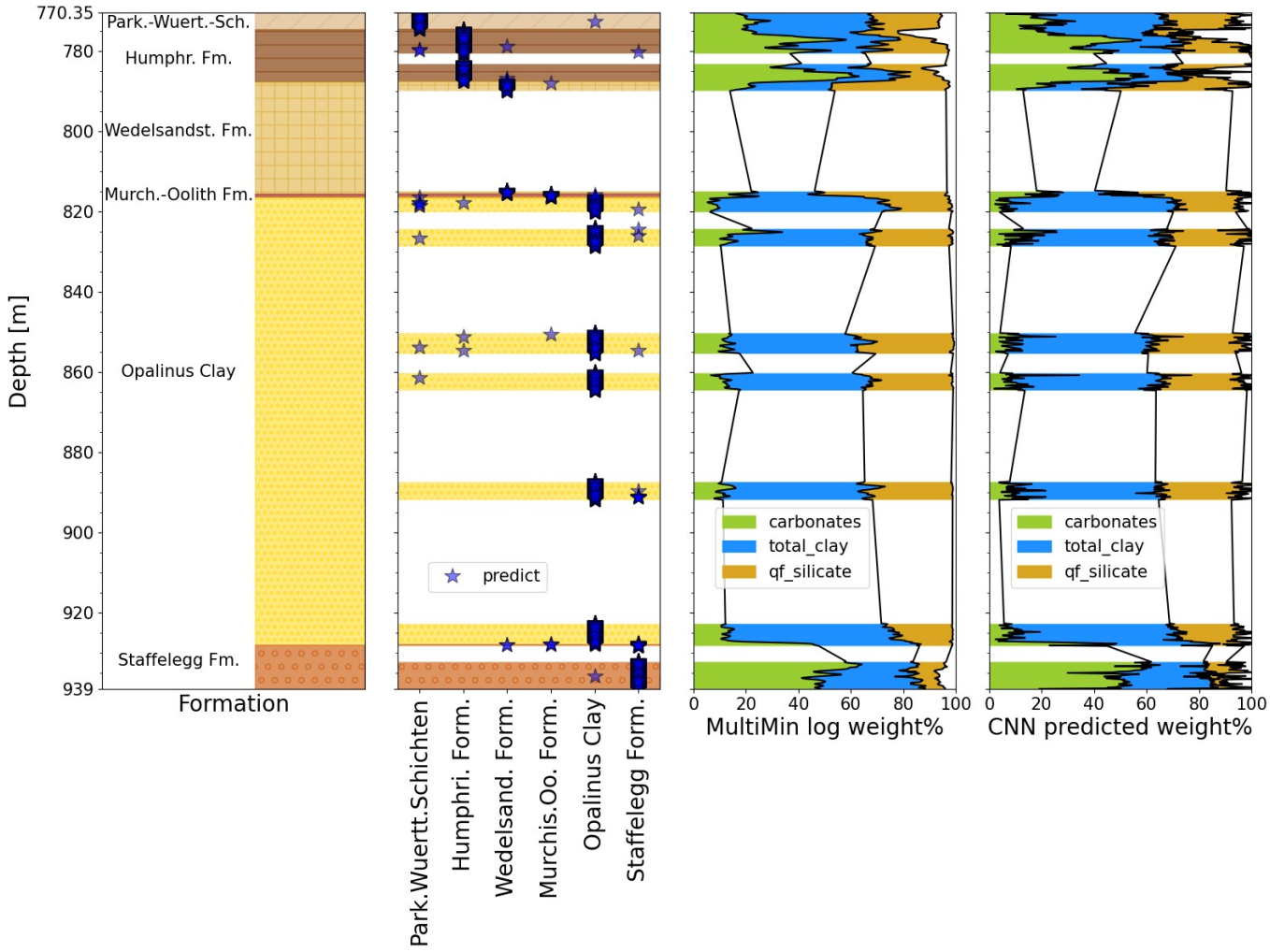

Fig. 2.11: Performance of the CNN model: Column 1: classification data, showing the different formations over depth, Column 2: CNN model predicted formation classes, Column 3: Mineral content from MultiMin Log analysis data, Column 4: Mineral content predicted with CNN model.

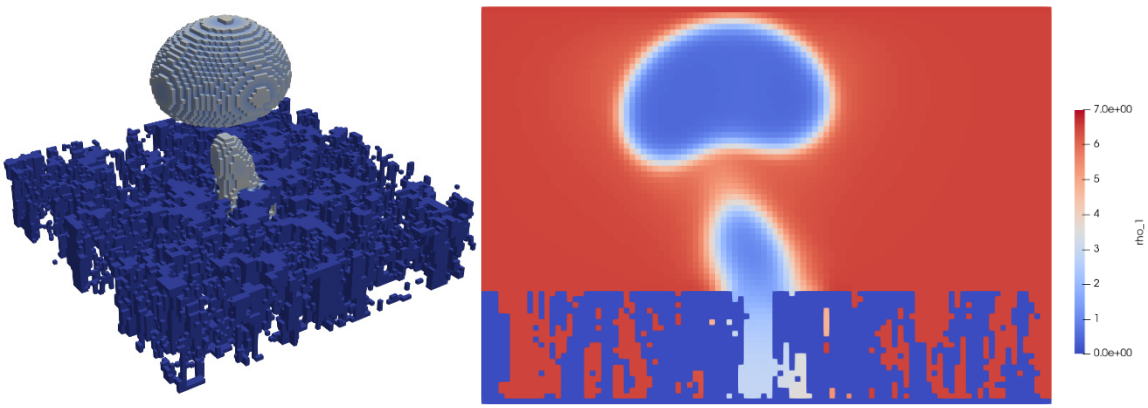

Fig. 2.12: Water boiling on crud surface (left) a 3D screenshot; grey is the vapour and blue is the porous medium; water is not visible for visualisation purposes, and (right) a 2D slice of a nucleate boiling simulation within a porous medium CRUD model; colour signifies the density, which is high for the water and low for the vapor. A bubble departure is observed.

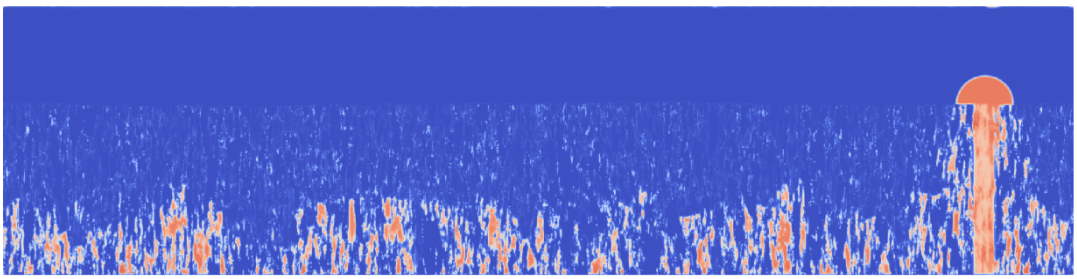

Fig. 2.13: Water-vapour mixture uptake through a porous medium. A steam chimney structure is added in the right hand side, a structure which is typical for CRUDS. Red color signifies the water (high density), while blue is vapour. The porous medium is not depicted for visualisation purposes.

2.9.2 Functionalisation of membrane surfaces: droplet transition from Wenzel to Cassie-Baxter state

The internal LES LB GPU code has been used (A. Mokos, N. Prasianakis), in collaboration with the University of Luxembourg (T. Jager and Prof. S. Leyer), for the PhD project of T. Jager. The project is relevant to the performance and design optimisation of desalination membranes. The micro-surface functionalisation is of interest, in order to reduce the membrane degradation and to increase water evaporation through the membrane. The use of micro-pillars has been investigated. It is important is to understand the wetting mechanisms. To validate the transition criteria from the Cassie-Baxter to the Wenzel state for periodically pillared surfaces, a model was created. A new criterion based on the energy barrier and adapted for a finite area has been derived. Fig. 2.14 shows two instances of a bubble on top of such a surface, in both the Wenzel and Cassie-Baxter states. When the liquid stream remains in the Cassie-Baxter state, the accumulation of solid precipitates on the membrane due to evaporation is reduced, thus increasing the service time of the material.

2.10 Characterisation of spent nuclear fuel with machine learning

In the context of nuclear energy production, waste management and nuclear safeguards, the precise quantification of spent nuclear fuel (SNF) inventory is of importance for safety, efficiency, and sustainability. One of the basic equations for building physics-based models for characterising SNFs is the Bateman equation, a linear ordinary differential equation. This equation describes the time evolution of the nuclear assembly based on decay rates. The stiffness of this equation, in combination with the possibly high dimension systems considered, can make the equation hard to solve. Therefore, improved numerical solution methods are needed, that are more accurate and faster. Hence, the capability of Physics Informed Neural Networks (PINNs), a special type of neural networks dedicated for solving differential equations, was considered to solve the Bateman equation. Different types and combinations of PINNs were tested and validated against state-of-the-art methods, and can be used to accelerate the numerical simulations while having the same accuracy, (Pacifico et al., 2023a,b, Pompe et al., 2023).

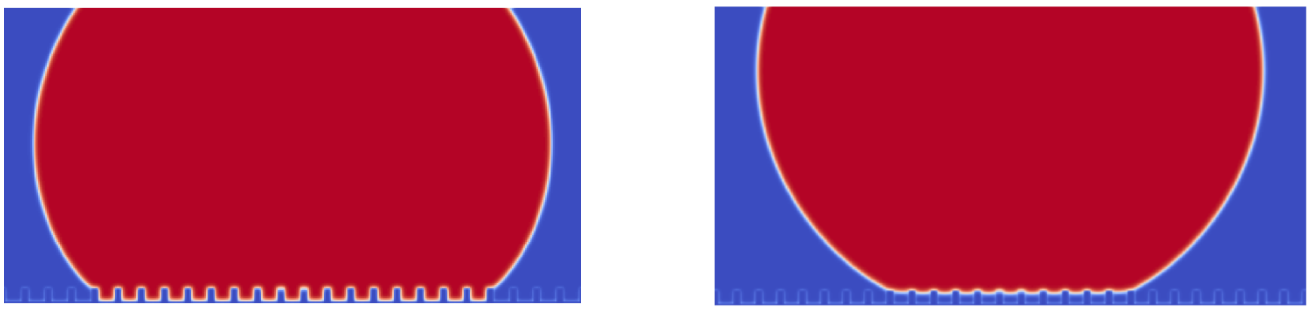

Fig. 2.14: Left: Water droplet in the Wenzel state (wetting the underlying surface), right: the droplet in the Cassie-Baxter state (not wetting the underlying surface). The pillars have a height of 33.08 μm, and an interpillar distance of 58 μm for the Wenzel or 54 μm for the Cassie-Baxter.

The Bateman equation, a fundamental component of the full physics-based models, as implemented in SCALE (SCALE: Standardized Computer Analyses for Licensing Evaluation) or CASMO5 (a lattice physics code for modeling PWR and BWR fuel), is of interest for SNF characterisation. Those models simulate the characteristics of spent nuclear fuels, like decay heat, actinide concentrations, or concentration of caesium and strontium. These models are reliable, but their computational demands are substantial. Hence, the goal in (Albà et al., 2023) was to introduce a surrogate modelling approach employing neural networks (NN) to predict the SNF properties with significantly reduced computational cost. The NN was trained using data generated from CASMO5 lattice calculations, and predicted the decay heat and nuclide concentrations based on key input parameters, including enrichment, burnup, cooling time, mean boron concentration and fuel temperature. Validation against physics-based simulations and measurements (Fig. 2.15) demonstrates excellent alignment, with computational costs reduced by an order of magnitude or more. This work underscores the feasibility of employing NNs as surrogate models for rapid SNF characterisation, offering a promising avenue to enhance computational efficiency in assessing nuclear fuel behaviour and associated risks.

2.11 Digital Twin of the Full Emplacement Mont Terri experiment

In addition to the geochemical evolution of a repository, the temperature evolution plays an important role at the initial stages. The temperature evolution defines temperature dependent geochemical parameters, the resaturation of the near-field and related mechanical, hydraulic and heat transport parameters, as well as the cooling capacity of the near-field and related waste storage (optimisation) options. Furthermore, temperature is the main parameter which can be monitored in a pilot repository to confirm repository performance during design, construction, operation and monitoring phase. A Full-scale Emplacement (FE) Experiment at the Mont Terri URL provides understanding on the aspects of the construction, the waste emplacement, the backfilling, and the early-stage evolution of a SF / HLW repository tunnel in a clay-rich formation (Opalinus Clay). In place of SF / HLW canisters heaters are used. The design and sensor data derived from this experiment serve as the basis for constructing a 3D digital twin replicating a part of the (pilot) repository. This advanced model facilitates the prediction of temperature variations within the repository's near-field, utilising early-stage sensor data like temperature and humidity installed within the vicinity of the pilot repository. A successful digital twin has the potential for extension, allowing the simulation of the long-term repository evolution including radionuclide transport.

Within EURAD MODATS WP, sensor data from the FE experiment (Mont Terri) are used to develop a digital twin for the FE experiment. 3D system information, e.g., homogeneous/heterogeneous distributions for porosity, saturation degree, density, and related thermal conductivity parameters are used to set up a physical model for heat transport (Fig. 2.16).

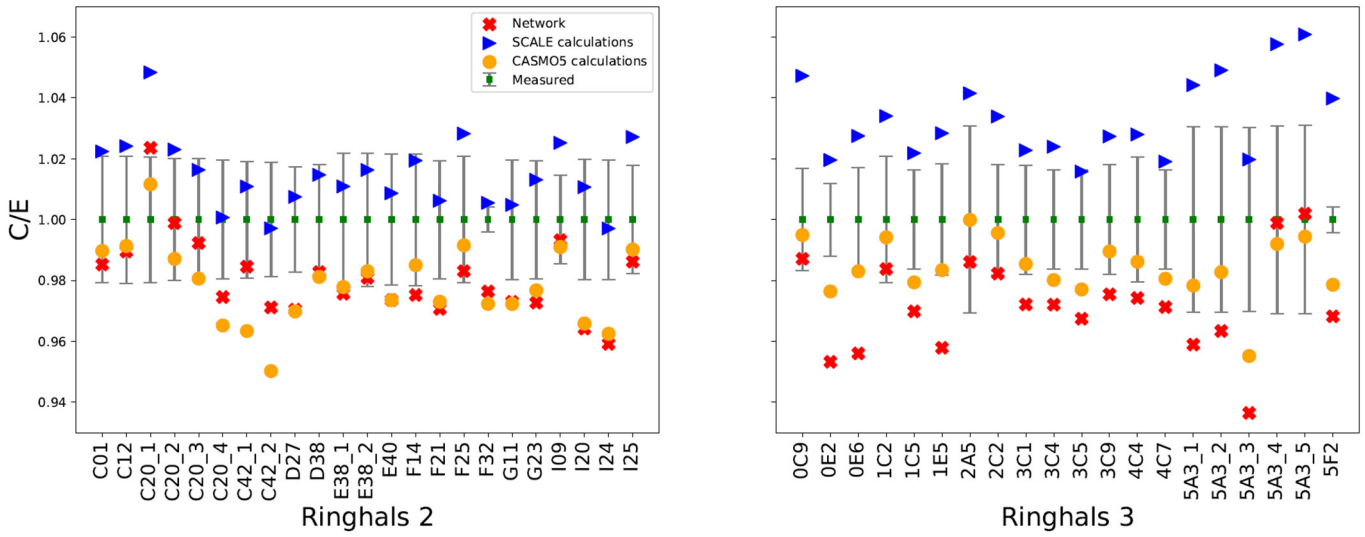

Fig. 2.15: Decay heat measurements and network prediction, with uncertainties shown as 2 standard deviations. On the x-axis different fuel assemblies are depicted, while on the y-axis the ratio between the measured (E) and calculated (C) decay heat is shown for two different Pressurized Water Reactors (Ringhals 2 on the left, Ringhals 3 on the right). The model was trained on the C20 assembly, a 15 x 15 UO_2 fuel assembly from Ringhals 2.

Data driven modelling is used to project the evolution of the degree of saturation measured from the sensors to the high resolution spatial discretised computational domain. The saturation in turn influences the thermal conductivity, especially of bentonite. For the implementation, the data from the saturation degree sensors are used (saturation degree as a function of x, y, z, time, material) to provide a surrogate function for the degree of saturation (humidity) in the 3D model domain (Fig 2.17). The physical model for heat transport is used to predict the 3D heat evolution around the three heaters, and within the tunnel and surrounding host rock (Fig 2.18). Comparison between the experimental data of the temperature sensors (Fig. 2.19) and the digital twin model data allows model validation. The modelling results are in excellent agreement with the experimental data. As a further step the physical model was used for the sensitivity analysis considering material properties (thermal conductivity), and a related parameter uncertainty analysis was conducted.

In a next step, new incoming data from the FE experiment will be used to feed the digital twin, i.e. to generate a new surrogate function for the saturation degree, improve model physical model predictions, and assess temperature sensor data with respect to sensor failures. Moreover, it is possible to mimic a number of FE experimental scenarios with assumptions on longer term changes of material properties around the heater, in order to simulate longer term evolution of the system compared to the real FE experimental duration.

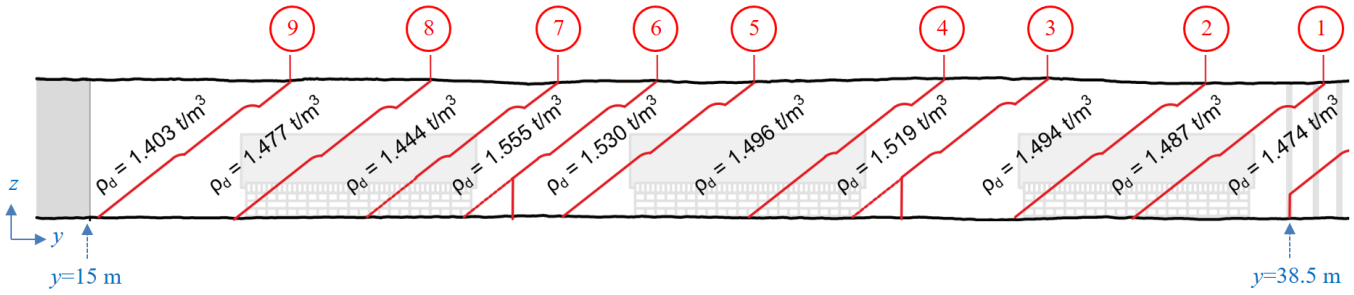

Fig. 2.16: 3-D slope scans and bulk dry densities of a longitudinal section of the backfilled FE tunnel (adapted from Lanyon et al., 2020).

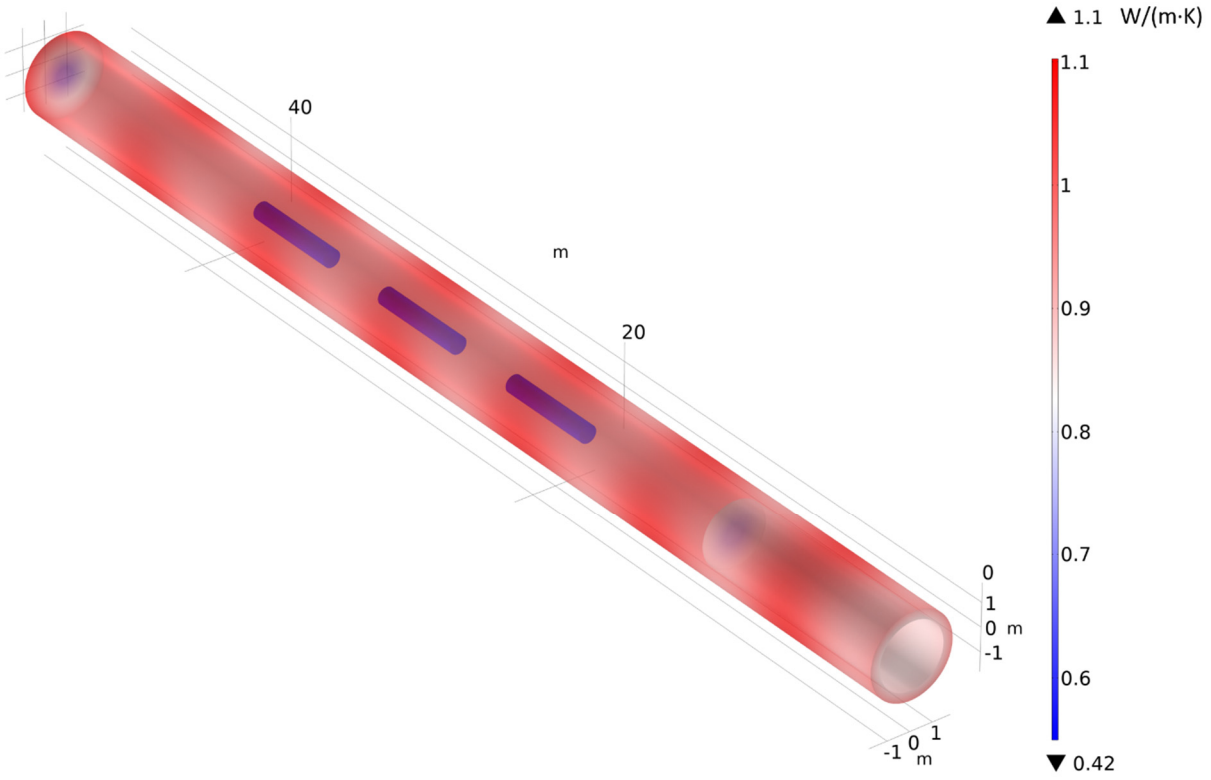

Fig. 2.17: Surrogate model of 3D-thermal conductivity evolution at t=3000 days of granulated bentonite material of the Full-scale Emplacement (FE) experiment at the Mont Terri underground laboratory.

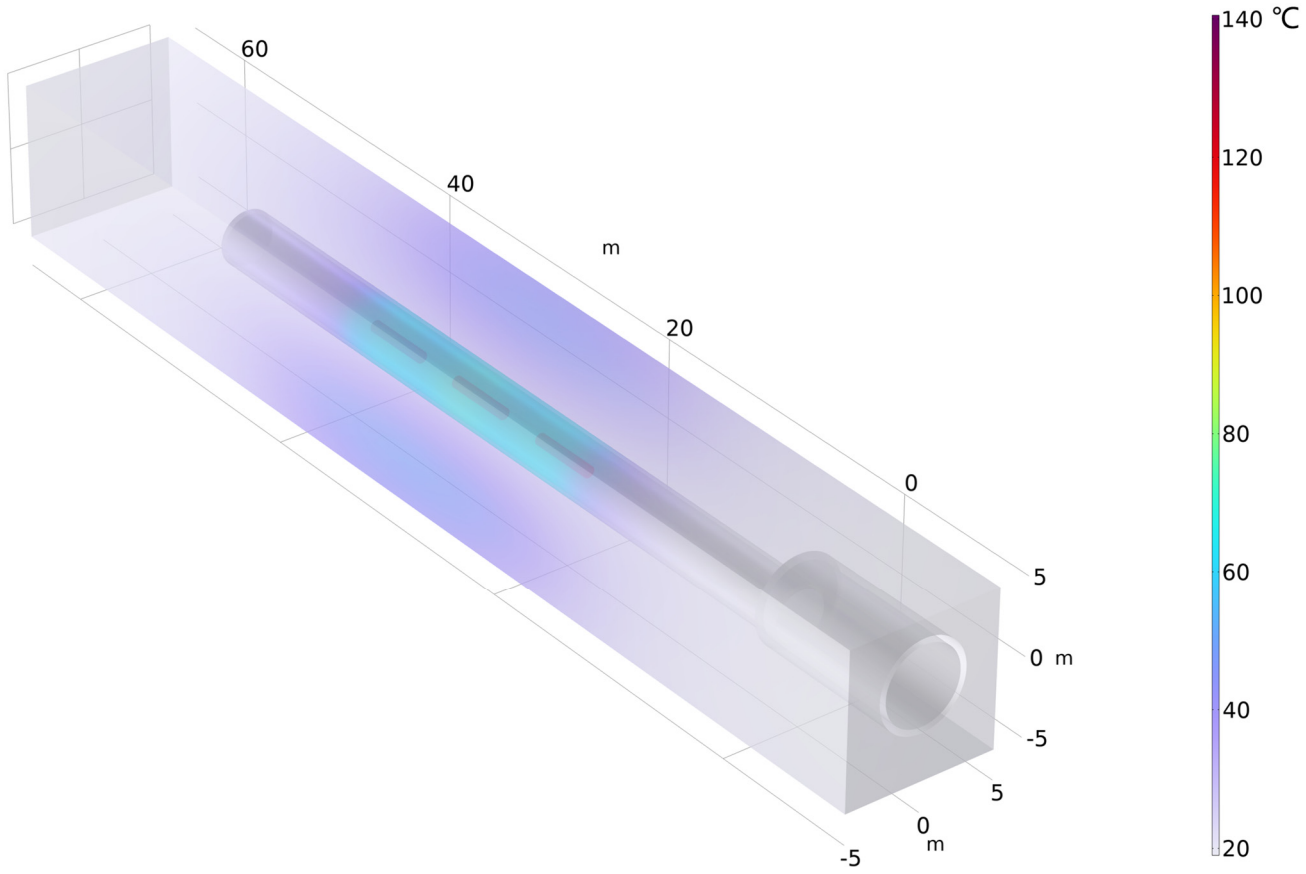

Fig. 2.18: Digital twin of 3D-temperature evolution at t=3000 days with a physical-based model for the Full-scale Emplacement (FE) experiment at the Mont Terri underground laboratory.

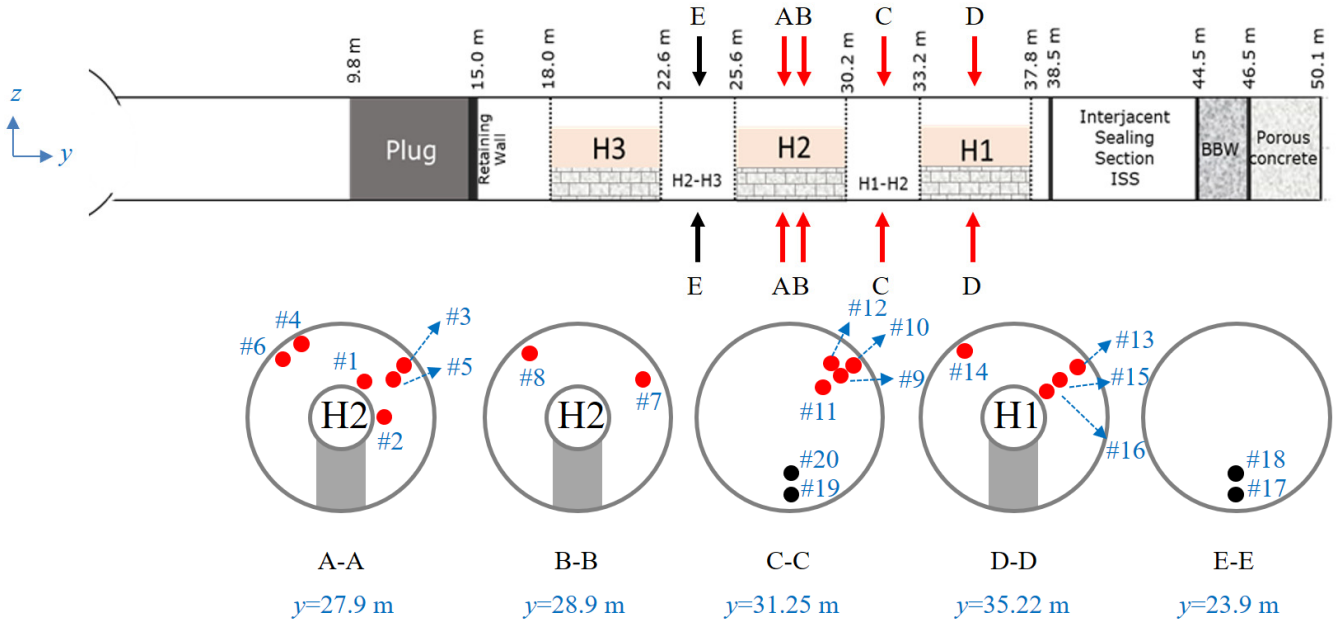

Fig. 2.19: Schematic diagram of positions of typical sensors of temperature/saturation degree sensors in the upper and lower half of the Granulated bentonite material (GBM) (adapted from Nagra, 2019).

2.12 References

Albà A., Adlemann A., Münster L., Rochman D., Boiger R. (2023)
Fast Uncertainty Quantification of Spent Nuclear Fuel with Neural Networks. Annals of Nuclear Energy Volume 196, 110204.

Alcolea A., Marschall P., Damians I. P., Olivella S., Gens A., Madaschi A., Bosch J., Laloui L., Shao H., Wang W., Kolditz O., Nagel T. (2021)
FE-Modelling Task Force/Task 1: Validation of Thermally Induced THM Effects in the Rock around the FE-Tunnel[R]. Nagra Arbeitsbericht, NAB 19-40, February 2021.

Ballester Llagaria I. (2023)
Bachelor Thesis at Department of Computer Science, ETH Zürich, Image Classification of Drilling cores.

Benson C.H., Trast J.M. (1995)
Hydraulic conductivity of thirteen compacted clays. Clays and Clay Minerals 1995, 43, 669–681.

Berner U., Kulik D.A., Kosakowski G. (2013)
Geochemical impact of a low-pH cement liner on the near field of a repository for spent fuel and high-level radioactive waste. Physics and Chemistry of the Earth, Parts A/B/C, 64, 46–56.

Blanc Ph., Lassin A., Piantone P., Azaroual M., Jacquemet N., Fabbri A., Gaucher E.C. (2012)
Thermoddem: A geochemical database focused on low temperature water/rock interactions and waste materials. Applied Geochemistry, 27(10), 2107–2116.

Boiger R., Churakov S.V., Ballester Llagaria I., Kosakowski G., Wüst R., Prasianakis N.I. (2024) Direct mineral content prediction from drill core images via transfer learning. Swiss Journal of Geosciences 117, 8 (2024).

Bradbury M.H., Berner U, Curti E., Hummel W., Kosakowski G., Thoenen T. (2014)
Geochemical near-field evolution of a deep geological repository for spent fuel and high-level radioactive waste. Nagra Technischer Bericht, NTB 12-01.

CASMO5: lattice physics code for modeling PWR and BWR fuel from Studsvik.
https://www.studsvik.com/key-offerings/nuclear-simulation-software/software-products/casmo5/

Cloet V., Curti E., Kosakowski G., Lura P., Lothenbach B., Wieland E. (2018)
Cementitious backfill for a high-level waste repository: impact of repository induced effects. Nagra Arbeitsbericht, NAB 18-41.

Curti E. (2022)
Aqueous Corrosion of Vitrified Nuclear Waste: Current Process Understanding, Literature Review and Recommended Rates. Nagra Arbeitsbericht, NAB 23-09.

Curti E. (2023)
Bentonite Pore Waters (BPW) for SGT-E3: Model Development, Testing and Final Calculations. Nagra Arbeitsbericht, NAB 23-43.

Curti E., Thoenen T., Kosakowski G., Baeyens B., Van Loon L.R., Leupin O.X, Martin L. (2023)
The long-term geochemical evolution of the near-field of the HLW/SF repository. Nagra Technischer Bericht, NTB 23-02.

Domínguez J.M., Fourtakas G., Altomare C., Canelas R.B., Tafuni A., García-Feal O., Martínez-Estévez I., Mokos A., Vacondio R., Crespo A.J.C., Rogers B.D., Stansby P.K., Gómez-Gesteira M. (2022)
DualSPHysics: from fluid dynamics to multiphysics problems. Computational Particle Mechanics 9(5): 867-895.

Glaus M.A., Frick S., Van Loon L.R. (2021)
Competitive effects of cations on the diffusion properties of strongly sorbing trace cations in compacted illite and Opalinus Clay. ACS Earth and Space Chemistry, 5(10), 2621–2625.

Hax Damiani L. (2021)
A novel reactive transport framework for fluid-rock interaction analysis: Computational approach, applications and benchmarks, PhD Thesis, Universität Bern, 22. October 2021.

Hax Damiani L., Boiger R., Haller R.L.I, Kosakowski G., Miron G.D., Kulik D.A. Churakov S.V., Prasianakis N. (2023)
Machine learning assisted geochemical reactive transport modeling: a fully automated workflow (in prep.).

Johnson L., Curti E., Spahiu K. (2023)
A Radionuclide Release Model for Spent UO_2 and MOX Fuel for Safety Assessment with Application to Waste to be Disposed of in a Deep Geological Repository in Switzerland. Nagra Arbeitsbericht, NAB 23-10.

Kato H., Muroi M., Yamada N., Ishida H., Sato H. (1994)
Estimation of effective diffusivity in compacted bentonite. MRS Online Proceedings Library (OPL) 1994, 353, 277.

Kosakowski G. (2023)
Reactive Transport Modelling of Material Interface Evolution in the HLW Near-field. Nagra Arbeitsbericht, NAB 23-33.

Kosakowski G., Watanabe N. (2014)
OpenGeoSys-Gem: A numerical tool for calculating geochemical and porosity changes in saturated and partially saturated media. Physics and Chemistry of the Earth, Parts A/B/C, 70–71, 138–149.

Krejci P. (2023)
Diffusion of sorbed cations in clays: Development, improvement and application of new and existing models. Thesis, University of Bern, Bern, Switzerland.

Krejci P., Gimmi T., Van Loon L.R. (2021)
On the concentration-dependent diffusion of sorbed cesium in Opalinus Clay. Geochimica et Cosmochimica Acta, 298, 149-166.

Kulik D.A., Wagner T., Dmytrieva S.V., Kosakowski G., Hingerl F.F., Chudnenko K.V., Berner U.R. (2013)
GEM-Selektor geochemical modeling package: revised algorithm and GEMS3K numerical kernel for coupled simulation codes. Computational Geosciences 17(1): 1-24.

Lanyon B., Lüthi F., Manukyan E (2020)
Interpretation of the First 5 Years of the FE Experiment: a THM Synthesis. Nagra Arbeitsbericht, NAB 19-46, September 2020.

Lothenbach B., Kulik D.A., Matschei T., Balonis M., Baquerizo L., Dilnesa B., Miron G.D., Myers R.J. (2019)
Cemdata18: A chemical thermodynamic database for hydrated Portland cements and alkali-activated materials. Cement and Concrete Research, 115, 472–506.

Ma B., Lothenbach B. (2020)
Synthesis, characterization, and thermodynamic study of selected Na-based zeolites. Cement and Concrete Research, 135, 106111.

Ma B., Lothenbach B. (2021)
Synthesis, characterization, and thermodynamic study of selected K-based zeolites. Cement and Concrete Research, 148, 106537.

Marty N.C.M., Claret F., Lassin A., Tremosa J., Blanc P., Madé B., Giffaut E., Cochepin B., Tournassat C. (2015)
A database of dissolution and precipitation rates for clay-rocks minerals. Applied Geochemistry, 55, 108–118.

Mokos A., Peng H., Miron G.D., Kulik D.A., Griffa M., Ma B., Prasianakis N., Churakov S.V. (2023)
Pore-level modelling of cement paste degradation due to cement-clay interaction. Goldschmidt 2023, Lyon, France.

Nagra (2019)
Implementation of the Full-scale Emplacement Experiment at Mont Terri: Design, Construction and Preliminary Results. Nagra Technischer Bericht, NTB 15-02, May 2019.

Owusu J.P., Karalis K., Prasianakis N. I., Churakov S.V. (2022)
Mobility of Dissolved Gases in Smectites under Saturated Conditions: Effects of Pore Size, Gas Types, Temperature, and Surface Interaction. The Journal of Physical Chemistry C, 126(40), 17441-17455.

Owusu J.P., Karalis K., Prasianakis N.I., Churakov S.V. (2023a)
Diffusion and Gas Flow Dynamics in Partially Saturated Smectites. The Journal of Physical Chemistry C, 127 (29), 14425 – 14438.

Owusu J.P. (2023b)
Numerical simulations of gas transport in argillaceous rocks: A molecular dynamics and pore-scale simulation study. (PhD Dissertation, University of Bern, Institute of Geological Sciences).

Pacifico G. (2023a)
Solving the Decay Equation using a Physics Informed Neural Network (PINN). Semester project at ETH-Zürich/PSI supervised by Andreas Adelmann, Arnau Albà and Romana Boiger.

Pacifico G. (2023b)
Solving the Bateman Equation using Physics Informed Neural Networks (PINNs). Master thesis at ETH-Zürich/PSI supervised by Andreas Adelmann, Arnau Albà and Romana Boiger.

Pompe M. (2023)
Physics-Informed Neural Networks (PINN) with a mathematics-informed architecture for the nuclear decay equation. Semester project at ETH-Zürich/PSI supervised by Andreas Adelmann, Arnau Albà and Romana Boiger.

Prasianakis N.I., Haller R., Mahrous M., Poonoosamy J., Pfingsten W., Churakov S.V. (2020)
Neural network based process coupling and parameter upscaling in reactive transport simulations. Geochimica et Cosmochimica Acta, 291, 126-143.

SCALE: Standardized Computer Analyses for Licensing Evaluation, it is a code system from Oak Ridge National Laboratory.
https://www.ornl.gov/scale/overview

Thoenen T., Hummel W., Berner U., Curti E. (2014)
The PSI/Nagra chemical thermodynamic database 12/07. PSI Bericht Nr. 14-04.

3 RETENTION AND TRANSPORT IN CLAY SYSTEMS

Glaus M.A., Churakov S.V., Dähn R., Di Lorenzo F., Ma B., Marques Fernandes M., Van Loon L.R., Qian Y. (PhD student), Stotskyi V. (PhD student), Wei X. (Guest PhD student), Zerva D. (PhD student)

3.1 Introduction

The retention of radionuclides by clay minerals in engineered and geological barrier systems is a key process responsible for the radiological safety of a deep geological repository. Reliable sorption (sorption distribution coefficients, R_d) and diffusion (effective diffusion coefficients, D_e) data and a mechanistic understanding of sorption and transport processes are thus mandatory for a proper evaluation of the barrier safety function. Sorption studies are mainly performed in batch systems using dispersed clays with a low solid to liquid ratio. In such an experimental setup the composition of the solution can be well controlled (e.g. pH, Eh, concentrations of anions and cations, organic and inorganic ligands) and/or varied in order to study their effect on the sorption. Undisturbed clay rocks, however, are very dense and are characterised by a high solid-to-liquid ratio. Several aspects of transferability for data and models derived from dilute dispersed systems to natural consolidated rocks and compacted clays are still under debate. The aim of this project is to address and resolve conceptual difficulties in applying the existing sorption models to diffusion in compacted argillaceous rocks.

A key question related to the transport oriented activities of the project deals with the question whether adsorbed ions shall be treated as immobile or only partially immobile. These two conceptual model assumptions have fundamental implications for the transport behaviour of ions in compacted systems. In the case of full immobilisation, a pore diffusion model can describe transport, whereas in the case of partial immobilisation surface diffusion models have to be applied.

3.2 Zinc(II) transport in compacted illite in the presence of organic ligands

3.2.1 Introduction

Argillaceous rock is considered as potential host rock for geological disposal of radioactive waste. Illite, as one of the most common argillaceous minerals, plays an important role in the environmental behaviour of hazardous species. In compacted illite, the transport processes of radionuclides are largely controlled by diffusion and characterised by strong retardation (Dähn et al. 2021). In contrast to the conventional understanding, recent studies showed that the cation species enriched in the electrical double layer (EDL) at the negatively charged illite surface are mobile and can provide a substantial contribution to the diffusive flux (Glaus et al. 2020). Organic ligands (OLs) exist widely in natural and engineered systems and have strong complexation capabilities, affecting the charge, size and geometry of metal cations, and thus their speciation. The presence of OLs results in a re-distribution of the cations in the EDL and between the solid and liquid, which is decisive for the diffusive flux. For this reason, OLs are assumed to not only have the well-known negative effect on the retardation of radionuclides by lowering their sorption on clay surfaces. In view of the more recent studies on the role of the EDL in the overall diffusion of cations (Glaus et al. 2020), this is not *a priori* the only important effect. Depending on speciation in the EDL, organic ligands can even decrease diffusion. In this study, we investigate the diffusion and sorption behaviour of Zn(II) cations in the presence of organic ligands (oxalate and 1,10-phenanthroline) in an illite system. These ligands were chosen for their model character in terms of differently charged chelates.

Due to chemical similarity, Zn(II) is a good analogue of divalent transition metal cations for sorption/ diffusion studies in soils and clays. In this study, transport of Zn(II) in Na^+-conditioned illite du Puy (Na-IdP) was investigated by in-diffusion and batch sorption experiments in the presence of either a negatively charged OL [oxalate (Ox^{2-})] or an uncharged OL [1,10-phenanthroline (Phen)], in order to clarify the role of positively charged (Phen) and/or negatively (or uncharged) charged (Ox) complexes of Zn(II). The coordination environments of the sorbed Zn(II) are characterised by Zn K-edge X-ray absorption spectroscopy (XAS).

3.2.2 Diffusion of Zn(II) in the compacted Na-illite

Fig. 3.1 shows the diffusion results for Zn(II) in compacted Na-illite in the presence of different OL concentrations at 0.01 M NaCl and at 0.1 M NaCl. The plots show the total element concentrations representing the sum of the radioactive and the stable isotopes. These values were calculated from the tracer activities using the ratio of stable isotope to radiotracer in the radiotracer source solution. The extents of decrease of Zn(II) concentrations in the upstream reservoir at 0.01 M NaCl and 0.1 M NaCl are comparable. The resulting profile analysis shows

deeper penetration of Zn(II) into compacted Na-illite at 0.01 M NaCl, indicating that Zn(II) diffusion is enhanced at the lower background electrolyte concentration. An exception is observed for the case of 0.1 mM Phen, where no significant differences in the profile occur for the different electrolyte concentrations.

A summary of the best-fit parameter values for Zn(II) is given in Tab. 3.1. A clear trend of increasing D_e and R_d values with decreasing concentrations of the background electrolyte can be noted. For both NaCl concentrations, different effects of the addition of organic ligands are observed in terms of diffusion and sorption behaviour. For both ligands, D_e decreases with increasing ligand concentration. However, the addition of Phen leads to an increase of R_d values, while R_d decreases in the case of Ox. This indicates that the two ligands tested differ in the formation of surface complex species. While Phen stabilises surface species by the formation of ternary surface complexes, Ox mainly forms aqueous complexes, leading to a decrease of the R_d.

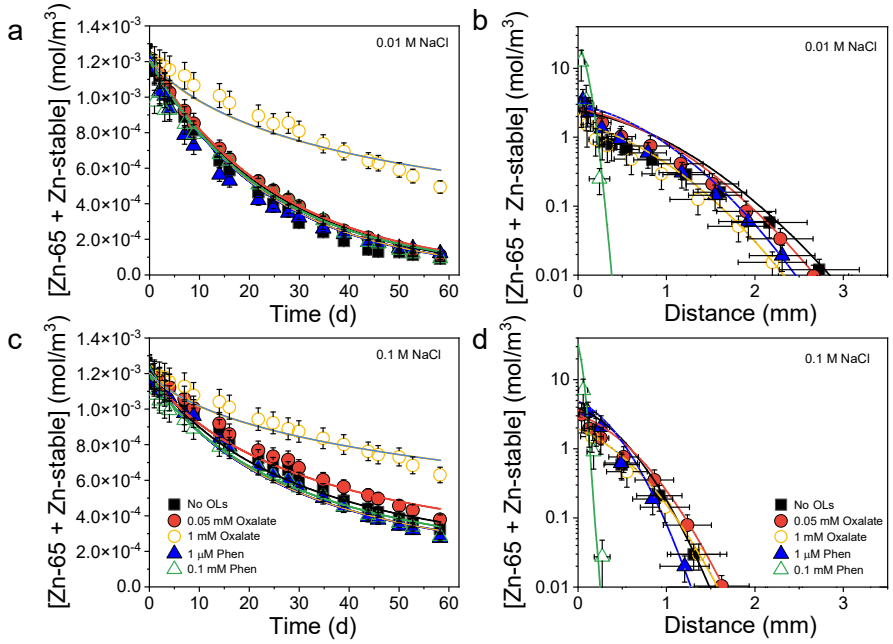

Fig. 3.1: In-diffusion experiments with Zn(II) at pH 5, showing (a) the total element concentration depletion in the upstream reservoir with time, and (b) the profile of total element concentration in the clay.

Tab. 3.1: Experimental conditions and best-fit parameter values from the diffusion experiments with Zn^{2+}.

OLs	background electrolyte (M)	D_e (m^2/s)	R_d (m^3/kg)
No	0.01	6.9E-08	399.71
0.05 mM Ox	0.01	1.5E-08	99.54
1 mM Ox	0.01	2.5E-10	2.01
1 µM Phen	0.01	3.2E-08	270.15
0.1 mM Phen	0.01	1.1E-09	555.91
No	0.1	4.0E-10	9.43
0.05 mM Ox	0.1	3.1E-10	5.84
1 mM Ox	0.1	1.0E-10	1.86
1 µM Phen	0.1	4.5E-10	15.36
0.1 mM Phen	0.1	6.0E-11	90.99

3.2.3 Batch sorption experiments of Zn(II) in dispersed Na-illite suspension

The batch sorption experiment of Zn(II) on Na-illite can provide mechanistic understanding of the diffusion behaviour of Zn(II). Preliminary results of Zn(II) sorption, and the modelling as a function of pH at the two electrolyte concentrations, are shown in Fig. 3.2. It is clear that Zn(II) species are strongly sorbed at pH 3.5 – 7.0, and that the sorption behaviours are different in the presence and absence of OL complexation. Compared to the system without OLs, weaker sorption and pH dependence of Zn(II) on Na-illite were observed in the presence of 1 mM Ox, which can be explained by the typical sorption behaviour of bare Zn(II). According to the 2SPNE SC/CE model (Bradbury & Baeyens 2009), the sorption was possibly controlled by the contribution of strong sites. In contrast, the presence of Phen significantly enhances the Zn(II) sorption. This might be explained by the formation of ternary surface complexes between illite–Phen–Zn induced by the formation of ion-π bonding between Phen and Na-IdP (Lan et al. 2008). The fitting results of the 2SPNE SC/CE model show that the sorption was mainly controlled by the strong site in the presence of high Phen concentration. Moreover, in contrast to the Ox and the bare Zn(II) system, the sorption was completely independent of the ionic strength and pH in the 0.1 mM Phen system, which further indicated that the predominant sorption mechanism was not cation exchange in the EDL.

Sorption isotherms of Zn(II) on Na-illite were determined at pH 5.0 and IS ~0.01 M in the presence of different OLs using a ^{65}Zn tracer. The experimental data and modelling results are shown in Fig. 3.3. In each subfigure, selected sample points for Zn K-edge XAS investigations are marked by Zn1, Zn2, and Zn3. Generally, the model calculations and experimental data are in good agreement, especially in view of the wide range of conditions covered ([Zn_{eq}]= 1×10^{-8} - 1×10^{-4} M). Based on the modelling indicated by the coloured solid lines in Fig. 3.3a, Zn should occupy essentially the so-called strong sites (high-affinity/low-capacity) at relatively low Zn(II) concentrations. With increasing concentration, Zn(II) should further occupy the weak sites and planar sites (low affinity/high capacity). Similar modelling results are shown in the presence of 0.05 mM Ox and 1 µM Phen. However, the sorption was mainly controlled by the sorption on the strong sites and planar sites in the presence of 1 mM Ox, and the sorption on the strong sites is dominant in the presence of 0.1 mM Phen. These results agree well with the weak diffusion of Zn(II) in the compacted Na-illite in the presence of high Phen concentrations.

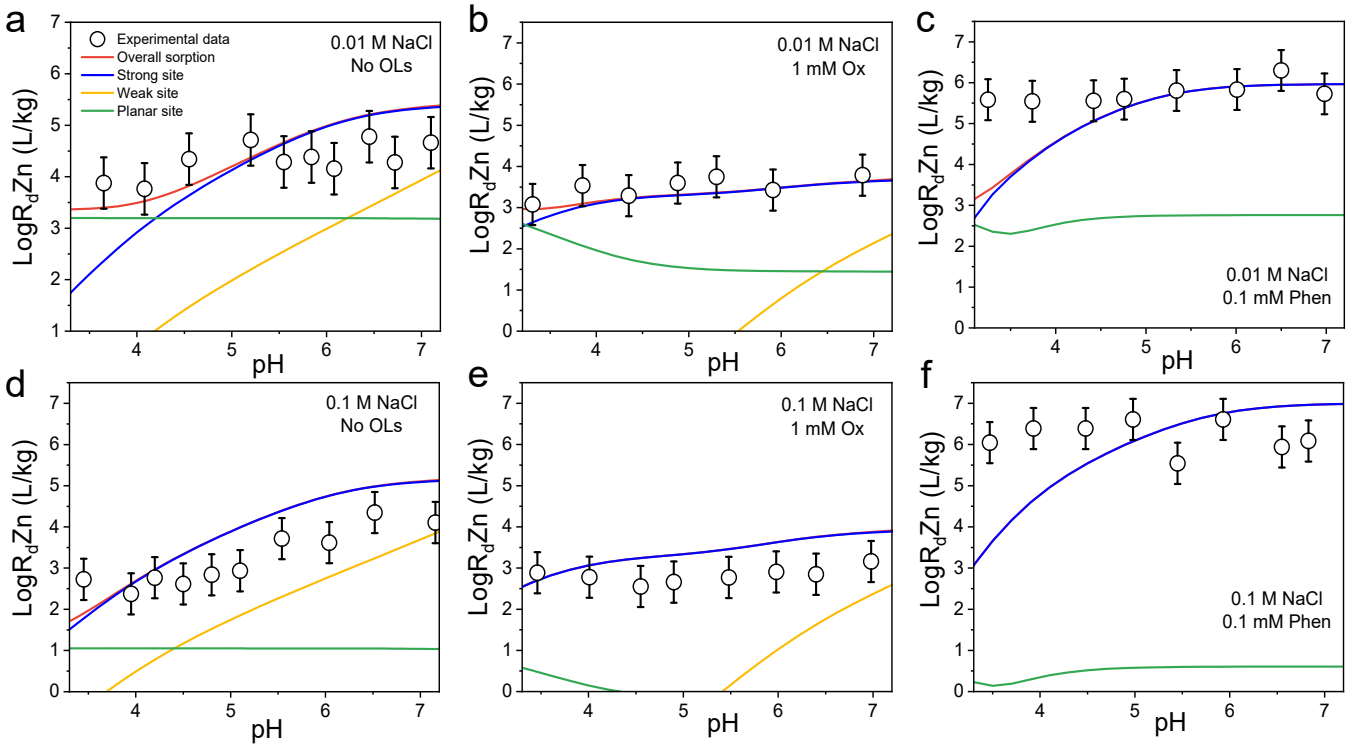

Fig. 3.2: Effect of organic ligands on the pH dependence of Zn(II) sorption onto Na-illite at trace Zn levels (1.84×10^{-7} M) in (a-c) 0.01 M NaCl and (d-f) 0.1 M NaCl (symbols), and modelling (solid red lines) with the contributions of sorption on planar sites (solid green lines), weak sites (solid orange lines) and strong sites (solid blue lines).

3.2.4 Spectroscopic investigation

To gain deeper insight into the sorption behaviours of Zn(II), the coordination environment of sorbed Zn(II) was investigated by XAS. Fig. 3.4 displays the $k^3\chi(k)$ EXAFS spectra of the solid samples, revealing distinct variations in the spectra as Zn(II) loading increases. Notably, the pronounced split beat pattern observed at 3.8 $Å^{-1}$, which is a characteristic feature of Zn(II) atoms located within octahedral layers of 2:1 phyllosilicates, is most prominent in the case of illite-Zn_{incur} (Dähn et al. 2011). As Zn loading increases, the splitting of oscillations at 3.8 $Å^{-1}$ becomes less pronounced or even disappears. This suggests that at low Zn(II) concentrations, the predominant mode of Zn uptake involves adsorption on edge sites, which exhibits a coordination environment similar to Zn atoms incorporated into the illite structure. With increasing Zn(II) concentration, other sorption sites become increasingly involved in Zn(II) adsorption, and the dominance of edge sites diminishes.

However, this observed trend is specific to Zn(II)-illite samples in the absence of OLs or in the presence of low concentrations of oxalate and 1,10-phenanthroline (Fig. 3.4a-c). For samples with high concentrations of 1,10-phenanthroline, there is no split peak at 3.8 $Å^{-1}$ across all Zn(II) concentrations (Fig. 3.4d). This indicates that the sorption mechanism of Zn(II) onto illite differs significantly between high 1,10-phenanthroline concentrations and conditions with either no OLs or low 1,10-phenanthroline/oxalate concentrations, as the OL concentrations strongly affect the Zn(II) speciation. Zn(II)-OL complexes predominate only under relatively high OL concentrations (i.e., 1 mM Ox or 0.1 mM Phen).

In the radial structure functions (RSFs) corresponding to both Zn-incorporated illite (illite-Zn_{incor}) and the Zn-sorbed illite (Fig. 3.5), a distinctive RSF peak attributed to the Zn-O interaction appears at R + ΔR = 1.62 Å (Dähn et al. 2021). As depicted in the spectra of Fig. 3.5a-c, as the metal loading increases, the amplitude of this peak diminishes, while its position shifts slightly towards lower R + ΔR values. This shift suggests that the bond length and coordination number of Zn-O decrease with increasing Zn(II) loading. However, due to the strong chelating capability of Zn(II) with Phen and the surplus of Phen in the system, in the presence of 0.1 mM Phen, the RSF peak at R + ΔR = 1.62 Å may be attributed to the Zn-N contribution (Fig. 3.5d). This assumption gains support from the presence of peaks within the 2 to 3.4 Å range. Beyond the first coordination shell, additional RSF peaks emerge in the R + ΔR range of 2 to 4 Å. Most of the variations observed in the $k^3\chi(k)$ spectra are manifested in the RSF within the 2 to 3.0 Å range.

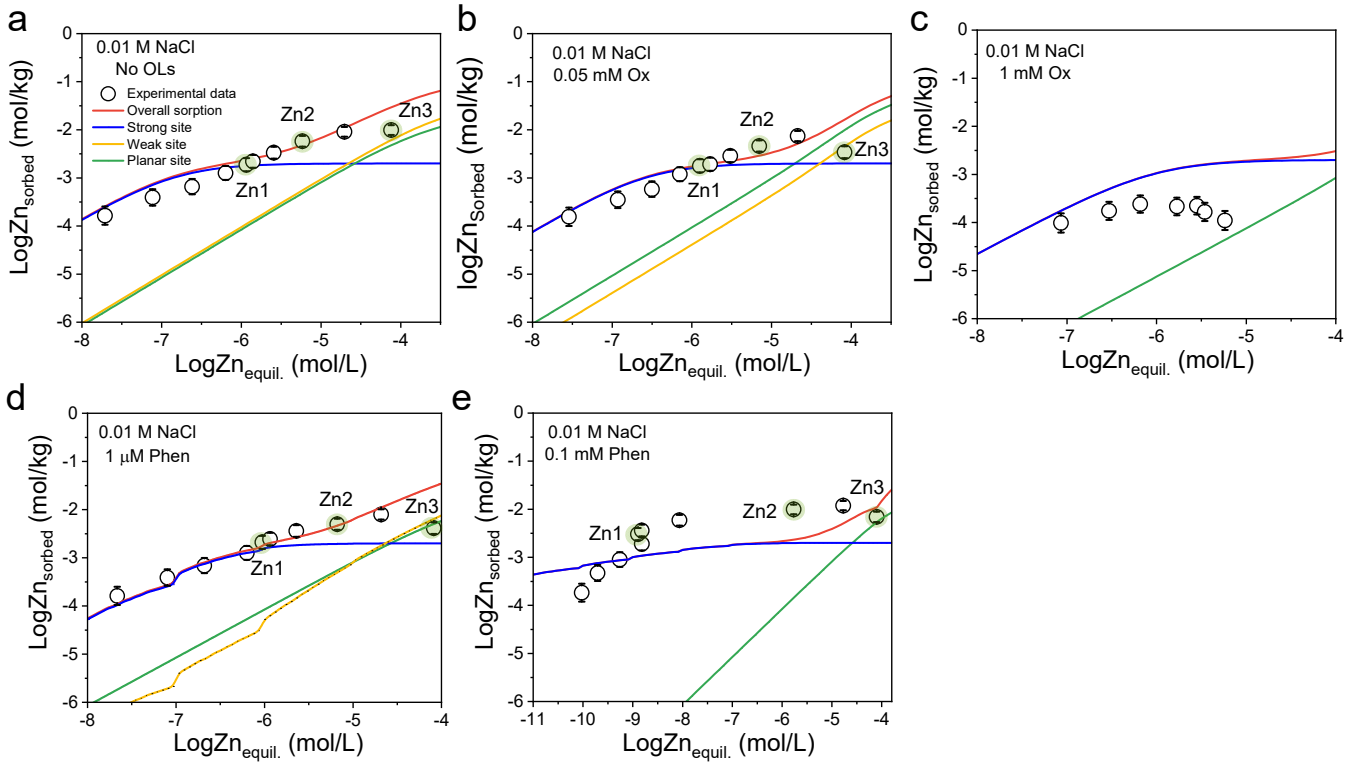

Fig. 3.3: Zn sorption isotherms on Na-illite in the (a) absence of organic ligands, and in the presence of (b) 0.05 mM oxalate, (c) 1 mM oxalate, (d) 1 µM Phen, (e) 0.1 mM Phen in 0.01M NaCl (symbols), and modelling (solid red lines) with the contribution of sorption on planar sites (solid green lines), weak sites (solid orange lines) and strong sites (solid blue lines).

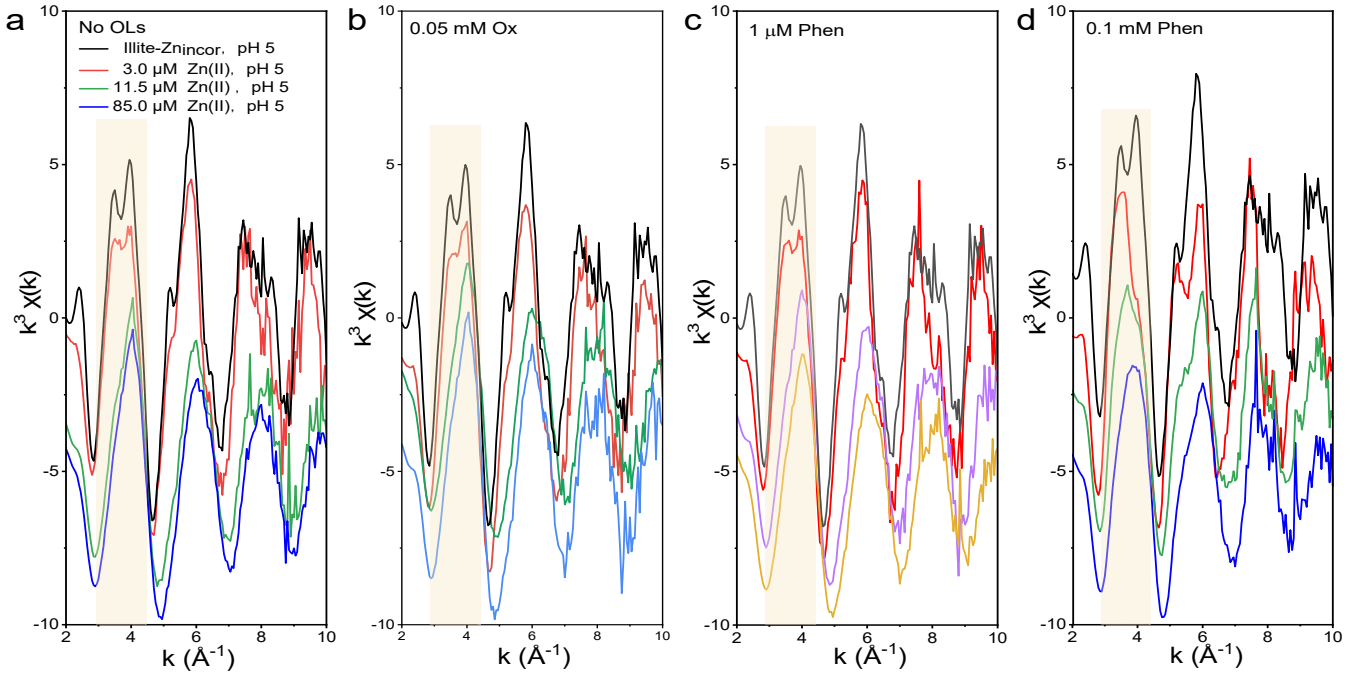

Fig. 3.4: Comparison of k^3-weighted Zn K-edge EXAFS spectra of Zn(II) sorbed illite in the absence and presence of OLs. (a) No OLs; (b) 0.05 mM Ox; (c) 1µM Phen; (d) 0.1 mM Phen.

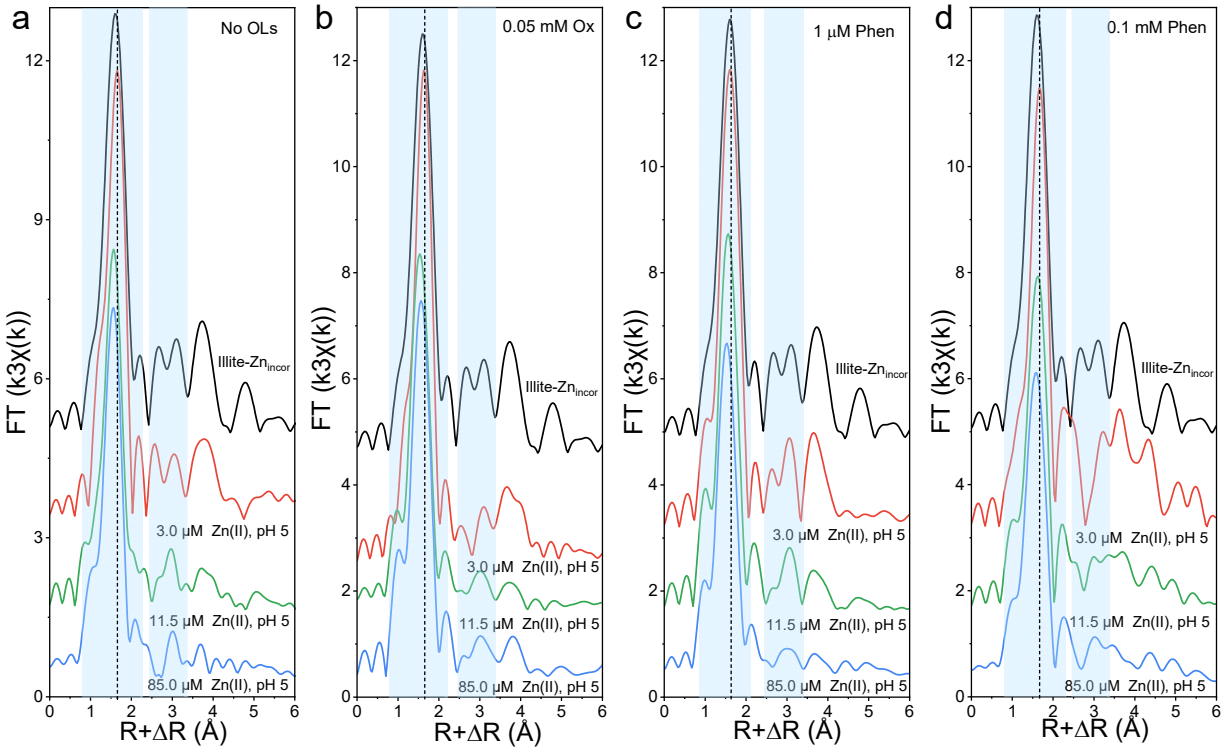

Fig. 3.5: Corresponding Fourier transforms in R space. (a) No OLs; (b) 0.05 mM Ox; (c) 1µM Phen; (d) 0.1 mM Phen.

Notably, the positions of these peaks remain relatively constant in the R + ΔR range of 2.4 to 3.4 Å in the absence of OLs and in the presence of 1 µM Phen (Fig. 3.5a and 5c). However, in the presence of 0.05 mM Ox and 0.1 mM Phen (Fig. 3.5b and 3.5d), these peak positions exhibit significant changes, possibly attributed to the formation of Zn-C bonds. Consequently, the RSF peak at R + ΔR = 1.62 Å is contributed by the species of Zn(II)-Ox and Zn(II)-Phen in the presence of 0.05 mM Ox or 0.1 mM Phen, respectively.

To further substantiate the hypotheses discussed above, we present the results of EXAFS data fitting in Fig. 3.6 and the best fitting parameters in Tab. 3.2. Data analysis of Fig. 3.6a-c reveals that Zn(II) is coordinated by a first shell of oxygen, with Zn-O distances ranging from 2.08 to 2.00 Å, corresponding to an overall trend of decreasing Zn-O bond distances. This trend aligns with the transition from Zn in sixfold coordination with oxygen atoms (R_{Zn-O} = 2.05–2.07 Å) to Zn in fourfold coordination with oxygen atoms (R_{Zn-O} = 1.94–1.97 Å) (Waychunas et al. 2002, Nelson et al. 2017). This suggests that at high Zn loading, Zn(II) predominantly exists in a tetrahedrally coordinated environment. Further evidence supporting a mixture of tetrahedral and octahedral Zn(II) surface complexes is the shift in k-space between 5.5–6.5 $Å^{-1}$ and 7.5–8.5 $Å^{-1}$ (Fig. 3.4), rather than the presence of a 5-fold coordinated complex. For the second shell fitting, it is observed that there are 0.4 – 2.1 Al atoms around Zn at distances of 3.0 – 3.1 Å, and 1.0 – 2.4 Si atoms around Zn at distances of 3.18 - 3.26 Å. These values are smaller than the theoretically expected numbers, indicating a higher degree of disorder (Dähn et al. 2003). For sorption in the presence of 1 mM Ox, Al and Si atoms from the illite structure as well as C atoms from oxalate are detected in the second shell (Li et al. 2017), indicating that Zn(II) is sorbed in the form of an illite-Zn(II)-Ox ternary complex. The first shell fitting results in the case of 0.1 mM Phen show that Zn(II) is surrounded by nitrogen atoms. The coordination number and distance of Zn-N remain relatively constant, and primarily exist in an octahedral geometry due to the excess Phen (Fig. 3.6). No obvious backscattering signal between Zn and the structural atoms of illite was detected at relatively low Zn(II) concentrations. This suggests that Zn(II) prefers to complex with Phen and further interact with the illite surface by forming illite-Phen-Zn(II) ternary complexes. However, with increasing Zn(II) loading, the coordination environment of sorbed Zn(II) changes from Zn-N to tetrahedral Zn-O.

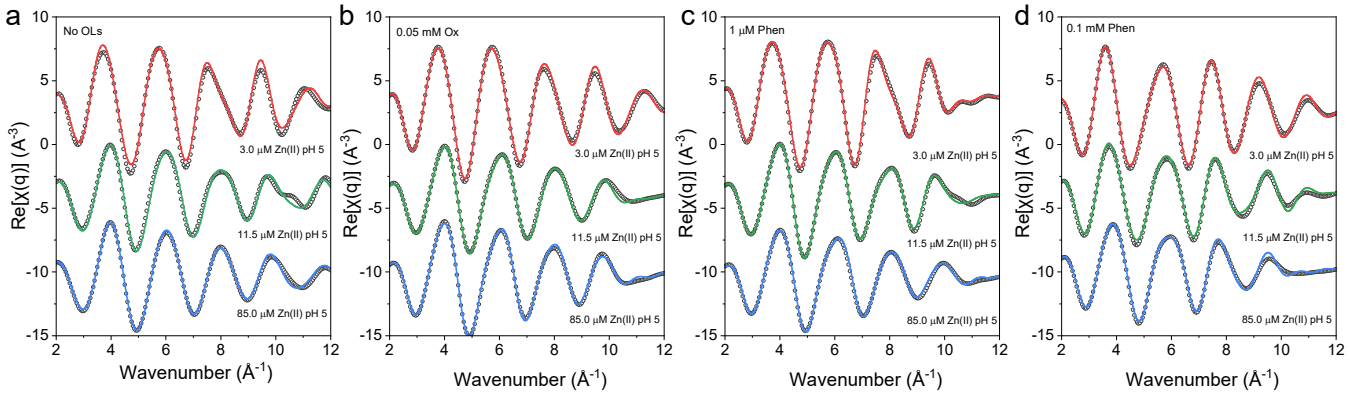

Fig. 3.6: Quantitative fits of FT^{-1} EXAFS data of Zn(II) sorbed on illite in the absence and presence of OLs. (a) No OLs; (b) 0.05 mM Ox; (c) 1µM Phen; (d) 0.1 mM Phen.

Tab. 3.2: Results from the quantitative fitting of EXAFS data.

Sample[a]	Zn-O			Zn-N			Zn-C			Zn-Al			Zn-Si			ΔE	Reduced χ^2	R factor
	CN[b]	R (Å)[c]	δ2 (Å)	CN	R (Å)	δ2 (Å)	CN	R (Å)	δ2 (Å)	CN	R (Å)	δ2 (Å)	CN	R (Å)	δ2 (Å)			
Illite-Zn1	5.4(5)	2.08(1)	0.005(1)							1.2(9)	3.00(6)	0.008(9)	2.4(9)	3.24(3)	0.007(8)	0.25	124	0.02
Illite-Zn2	4.7(2)	2.02(1)	0.007(1)							0.4(2)	2.97(2)	0.001(9)	1.8(5)	3.18(2)	0.009(9)	0.28	27	0.008
Illite-Zn3	4.7(2)	2.01(1)	0.007(1)							0.5(2)	3.02(1)	0.006(4)	1.3(3)	3.19(1)	0.006(3)	0.57	42	0.009
Illite-0.05 mM Ox-Zn1	6.9(2)	2.08(1)	0.006(1)				3.3(5)	2.80(1)	0.009(3)	1.3(7)	2.99(2)	0.009(9)	1.0(3)	3.26(2)	0.004(5)	5.77	26	0.003
Illite-0.05 mM Ox-Zn2	5.8(1)	2.01(1)	0.008(1)				1.2(4)	2.85(4)	0.009(4)	1.1(6)	3.05(1)	0.009(2)	1.5(2)	3.23(1)	0.007(2)	5.77	31	0.002
Illite-0.05 mM Ox-Zn3	4.6(2)	2.02(1)	0.006(7)							1.4(4)	3.08(1)	0.009(9)	1.9(9)	3.25(3)	0.009(9)	1.41	19	0.003
Illite-1 μM Phen-Zn1	5.7(3)	2.08(1)	0.005(1)							1.0(5)	2.98(5)	0.009(9)	1.4(8)	3.25(3)	0.003(7)	0.35	129	0.009
Illite-1 μM Phen-Zn2	4.6(3)	2.02(1)	0.006(1)							1.0(6)	3.05(3)	0.002(6)	1.7(7)	3.23(2)	0.005(5)	1.74	40	0.003
Illite-1 μM Phen-Zn3	4.5(4)	2.00(1)	0.007(1)							0.9(4)	3.06(2)	0.006(6)	1.4(5)	3.22(2)	0.008(7)	-0.37	71	0.004
Illite-0.1 mM Phen-Zn1				7.9(8)	2.15(1)	0.005(1)	5.7(7)	2.99(3)	0.008(8)							4.9	60	0.004
Illite-0.1 mM Phen-Zn2				7.3(4)	2.11(1)	0.007(9)	2.2(7)	2.92(3)	0.009(2)							4.36	57	0.004
Illite-0.1 mM Phen-Zn3	3.2(2)	2.06(1)	0.008(1)	1.4(4)	2.09(2)	0.006(4)	3.5(8)	2.91(1)	0.005(4)	2.1(6)	3.08(1)	0.009(5)	1.0(3)	3.25(1)	0.002(3)	2.86	142	0.005

[a] Sample collection conditions are indicated in the adsorption isotherm (Fig. 3.3), Zn1: 3.0 μM Zn(II); Zn2: 11.5 μM Zn(II); Zn3: 85.0 μM Zn(II);

[b] CN: coordination number;

[c] R: Radial distance

3.3 Functional relationships for estimating diffusion behaviour of uncharged tracers for application in diffusion databases

The use of adequate transport models and parameter values for diffusion is an indispensable requirement for a robust and reliable assessment of potential radioactive doses in the biosphere. Diffusion measurements of tritiated water (HTO), $^{36}Cl^-$ and $^{22}Na^+$ tracers on > 130 samples from the deep-borehole drilling campaign (TBO) of Nagra in the Mesozoic sediments of Northern Switzerland were carried out at LES in order to provide a sound data basis for predicting diffusion data for dose critical elements in various abstracted geological model units and bentonite.

Archie's relationship and extensions of it were used in previous studies (Bestel et al., 2018; Glaus et al., 2010; Van Loon, 2014; Van Loon & Mibus, 2015) for a simplistic empirical description of the effective diffusivity as a function of the total porosity of the porous medium, and to derive effective diffusion coefficients for safety analysis (Van Loon, 2014). In view of the data obtained in the TBO study, it is rather obvious that this approach will not provide sufficient accuracy: the majority of the porosity values of the rock samples cluster around a value of ~0.1, but with rather large variability of the D_e values for HTO. Furthermore, the best-fit parameter values for the extended Archie's relationship provided in Van Loon & Mibus (2015) were not sufficiently consistent with the results obtained for carbonate-rich rock samples (Fig. 3.7). For this reason, an improved empirical model description was developed, relating the effective diffusion coefficient to the total clay content of the sample.

Fig 3.8 visualises the correlation between the D_e value of HTO and the total clay content of a rock sample (Van Loon et al., 2023). It can be seen that between a clay content of approximately 20 and 50 wt.%, the dependency of the effective diffusion coefficient on the clay content is rather weak. Below a clay content of 20% and above a clay content of 50 wt.%, the effective diffusion coefficient decreases with decreasing or increasing clay content.

3.4 Temperature effects in the surface diffusion of $^{57}Co^{2+}$ tracer in Opalinus Clay from TBO samples

The diffusion data predicted for dose critical elements in abstracted geological model units and bentonite are determined at a standard temperature of 25 °C. Extrapolations to different temperatures are obtained using the Arrhenius equation (Van Loon & Mibus, 2015). It is an open question whether such relationships are also applicable for elements undergoing surface diffusion. Surface diffusion is not only governed by well-studied geometric factors, but also by the chemical equilibration of ionic species between the bulk aqueous phase and the Donnan volume near the basal clay surfaces (Glaus et al., 2015). The exact dependence of these thermodynamic equilibria on temperature is unknown. For this reason, temperature effects of surface diffusion are currently studied at LES, both for compacted illite model systems and for samples from the TBO deep-drilling campaign of Nagra.

Table 3.3 shows the results obtained for $^{57}Co^{2+}$ diffusion in small scale samples of Opalinus Clay from the Bözberg 2-1 borehole embedded in epoxy resin. The reported values are the best fit parameter values for the effective diffusion coefficients (D_e) and sorption distribution coefficients (R_d). The latter values are derived from the observed rock capacity factors.

The final interpretation of these results is still pending. It involves also the diffusion coefficients of the uncharged HTO tracer, which were also measured at room temperature.

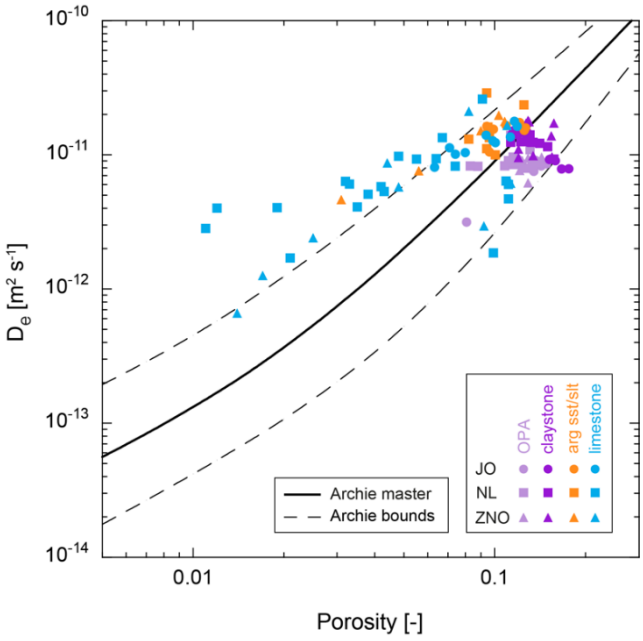

Fig. 3.7: Relationship between accessible porosity and effective diffusion coefficient of HTO (Archie's plot). The lines were calculated using the e-Archie equation and parameters given in Van Loon & Mibus (2015).

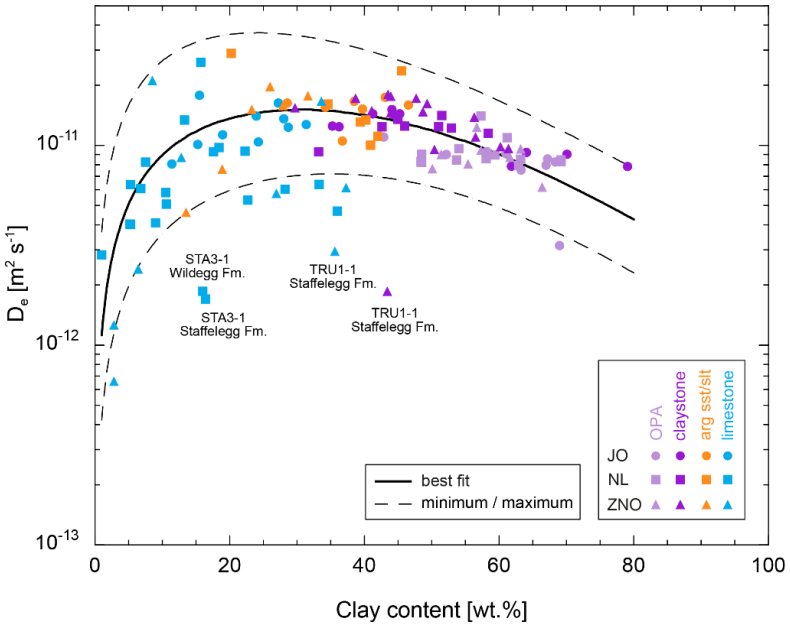

Fig. 3.8: Correlation between the effective diffusion coefficient of HTO (D_e) and the total clay content of a sample. The solid line represents the best fit. Upper and lower curves represent the upper and lower bounds. Some of the outliers are labelled and are clay-rich samples with high amounts of organic carbon (4.7 and 7.8 wt.%) from the Staffelegg Formation of borehole TRU1-1 (ZNO). Two other outliers are clay-poor samples with high calcite (79 and 74 wt.%) but low organic carbon contents (0.36 and 0.28 wt.%), and are from the Staffelegg and Wildegg Formation of the deep borehole STA3-1 (NL).

Tab. 3.3: Best-fit parameter values for diffusion parallel to the bedding of $^{57}Co^{2+}$ in small cylindrical samples of Opalinus Clay from borehole sample BOZ 2-1-571.50-DI (Bözberg 2-1 borehole). The measurements were done using synthetic Bözberg pore water (ionic strength 0.19 M, pH 7.9).

Sample	Temperature (°C)	D_e (m^2/s)·10^{10}	R_d (m^3/kg)
67	23	0.76 ± 0.29	0.70 ± 0.13
68	23	0.87 ± 0.31	0.85 ± 0.21
43	40	1.4 ± 0.3	0.30 ± 0.10
46	40	1.9 ± 0.5	0.88 ± 0.10
69	60	3.0 ± 1.0	1.03 ± 0.3
70	60	2.7 ± 0.8	1.1 ± 0.3

3.5 Eurad project FUTURE: Retention and transport of radionuclides

3.5.1 The effect of cation loading on the anion-accessible porosity of Cl^- in compacted illite

The effect of different homoionic forms of illite on anion accessible porosity has been studied in the framework of the Eurad project FUTURE. Samples of illite converted to Li, Na, K and Cs homoionic forms were compacted into POM confinement cells at bulk dry densities ranging from 1.4 to 1.6 g/mL and saturated with the corresponding metal chloride solutions of variable concentration. Each experimental condition was measured at least in triplicate, counting in total 65 cells. As a next step, the illite samples were extruded from the cells and dispersed in a defined volume of ultrapure water (MQ). The amounts of Cl^- from the clay pore space were measured by ion chromatography. The anion accessible porosity (ε_{acc}) was calculated according to eq. (3.1)

$$\varepsilon_{acc} = \frac{C_{Cl} * V_{MQ}}{C_{eq} * V_{clay}} \quad (3.1)$$

where C_{Cl} (mol/L) is the measured concentration of Cl^- in the extracts, V_{MQ} (L) is the extraction volume, C_{eq} (mol/L) is the electrolyte concentration measured at the

end of the sample saturation, and V_{clay} (L) is the volume of the extruded clay. The ε_{acc} values were normalized with respect to the total water porosity (ε_{tot}) of the sample. The anion-accessible porosity fraction δ (–) is the ratio $\frac{\varepsilon_{acc}}{\varepsilon_{tot}}$ which allows for the comparison of the anion exclusion effect irrespective of bulk dry density.

The experimental results (Fig. 3.9) show the dependence of the anion-accessible porosity fraction on the homoionic form of the clay and on the electrolyte concentration of the saturation solution. Considering that ε_{acc} cannot be larger than ε_{tot}, δ must be ≤ 1. The observed tendency of increasing δ from Li- to Cs-illite can be interpreted in terms of an electrostatic model, in which the negative surface charge is partly shielded by cations closely bound to the clay surface (Stern layer). Moreover, the anion exclusion effect seems to be similar for Li- and Na-illite, whereas those from K- and Cs-illite form a different cluster. This observation is in alignment with the finding of Bourg et al. (2017) where K^+ and Cs^+ form inner sphere complexes within the hexagonal cavities of the tetrahedral sheet, while Li^+ and Na^+ form inner sphere complexes on the oxygen triad.

Similar experiments using SO_4^{2-} electrolytes have recently been completed, and the results are under evaluation.

3.5.2 Redox reactivity of Se on iron bearing clay minerals

Fe-bearing clay minerals used as engineered barriers and backfill in radioactive waste repositories are critical for immobilizing redox sensitive radionuclides, such Tc(VII) and Se(IV). To better understand the molecular mechanism of selenite Se(IV) retention in argillaceous systems, structural characterisation of Fe-bearing clay minerals is conducted in the Eurad project FUTURE. A comprehensive understanding of the clay structural changes under the transition from oxidising to reducing conditions is necessary in the sorption experiments. In this study, clay reduction experiments in the aqueous phase were conducted by the citrate-bicarbonate-dithionite (CBD) method. Techniques including X-ray diffraction (XRD), transmission electron microscopy (TEM), ^{57}Fe Mössbauer spectrometry, photoelectron spectroscopy (XPS), X-ray absorption near edge structure (XANES) spectroscopy including its pre-edge, extended X-ray absorption fine structure (EXAFS) spectroscopy, and mediated electrochemical oxidation and reduction (MEO/MER) were applied to study the clay dissolution in the reduction process, reveal the structure of nontronite, and compare the results of different method for the measurement of the Fe redox state as a function

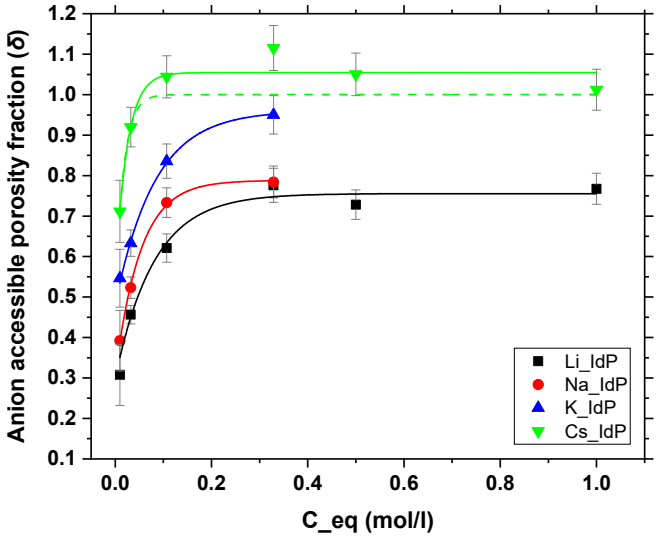

Fig. 3.9: Anion-accessible porosity fraction (δ) as a function of index cation of the illite samples and the corresponding electrolyte concentration. The solid lines are simple non-linear fit curves without physical background. The green dotted line is the limiting curve for $\delta = 1$.

of reduction degree. The combination of XRD and TEM showed that the long-range structure of nontronite at the highest obtained reduction degree of 44% Fe(II) is not different from that of fully oxidised nontronite, except for a slight basal plane dissolution on the external surfaces. The short-range order probed by EXAFS spectroscopy suggests increasing structural disorder and Fe clustering with increasing reduction of structural Fe. The consistency of the results of quantitative Fe redox state measurements with Mössbauer spectrometry, XPS, XANES, EXAFS, and MEO/MER suggested that all methods provide reliable Fe(II)/Fe(III) ratios and can be applied to other clay samples. This work builds a good foundation for the further investigation of the retention of Tc(VII) and Se(IV) on Fe(II)/Fe(III) bearing clay minerals. This work has been published this year (Qian et al., 2023).

3.5.3 Reversibility of Sorption

The sorption of radionuclides on clay minerals in engineered and geological barrier systems is a main pillar in the safety case for deep geological disposal of radioactive waste. Subtask 2.3 of the Eurad WP FUTURE investigates the reversibility of sorption by clay materials. Currently existing uptake models are based on the assumption that sorption processes are fully reversible. Other processes such as the neoformation of solid phase, the incorporation of radionuclides in the clay structure, or recrystallisation processes occurring at the edge sites of the clay mineral surfaces can severely contradict the assumptions made in these classical models. It is therefore of utmost importance for safety assessments to gain a molecular

understanding of experimental conditions which can favour or hinder reversible sorption processes. Wet chemistry and EXAFS investigations showed that the sorption of Zn by illite and SWy montmorillonite is irreversible at pH 7 and metals loadings up to 20 mmol/kg. Only at higher metal concentrations, 40% of the metal loading could be desorbed. The experiments showed that Zn-surface complexes (for loadings up to 20 mmol/kg) on illite and montmorillonite remained unchanged for a reaction period up to 2 years, and that uptake processes at the edges of the clay particles are responsible for the irreversibility. The study investigated loadings up to 60 mmol/kg and did not observe the precipitation of new Zn phases.

3.6 Molecular scale understanding of competitive cation adsorption on swelling clay minerals

In the framework of the SNF project (SNF Nr. 200021-129947) "*Molecular scale understanding of competitive cation adsorption on swelling clay minerals*", experimental studies and molecular dynamics simulations are used to further refine the mechanistic aspect of cation uptake by smectite minerals. One set of experiments was aimed to study the protolysis constants of saponite, i.e. backtitration experiments (Baeyens & Bradbury, 1997). Other experiments aimed to validate the significance of the metal sorption behaviour of saponite observed for nickel and lutetium by using other metals. In particular, the sorption by saponite of other four trivalent lanthanides (Ce^{III}, Dy^{III}, Nd^{III}, and Tb^{III}) and divalent zinc was studied. The sorption samples were characterized with polarised EXAFS at ESRF with in-house beamtime thanks to the collaboration with HZDR.

The new results agreed with previous observations, and the four additional REEs showed sorption coefficients higher than divalent nickel (Fig. 3.10a). The EXAFS characterisation confirmed the presence of a unique significant backscattering contribution coming from the first shell of oxygen atoms (Fig. 3.10b). The lack of backscattering contributions from octahedral and tetrahedral sites and the absence of angular dependence are very different behaviours from what has been observed for Ni^{2+}. The different size of the ions could provide an explanation for the observation that lanthanides do not seem to be able to bond to edge structural positions (commonly called strong sites); rather, the mechanism of lanthanide sorption by saponite seems to resemble the formation of outer-sphere complexes. However, preliminary fitting results performed with Artemis showed a strong deformation of the coordination environment of the lanthanide ions. As an example, Tb^{3+} ions showed a strong reduction of the coordination number between Tb-O when going from an aqueous stock solution of $TbCl_3$ to Tb^{III} sorbed by Na-Mg-saponite at different loadings (Fig. 3.10c). The high sorption of REEs by saponite and the impossibility for REEs to bound to strong sites imply that REEs can bound relatively well to weak sites (which are much more abundant than strong sites).

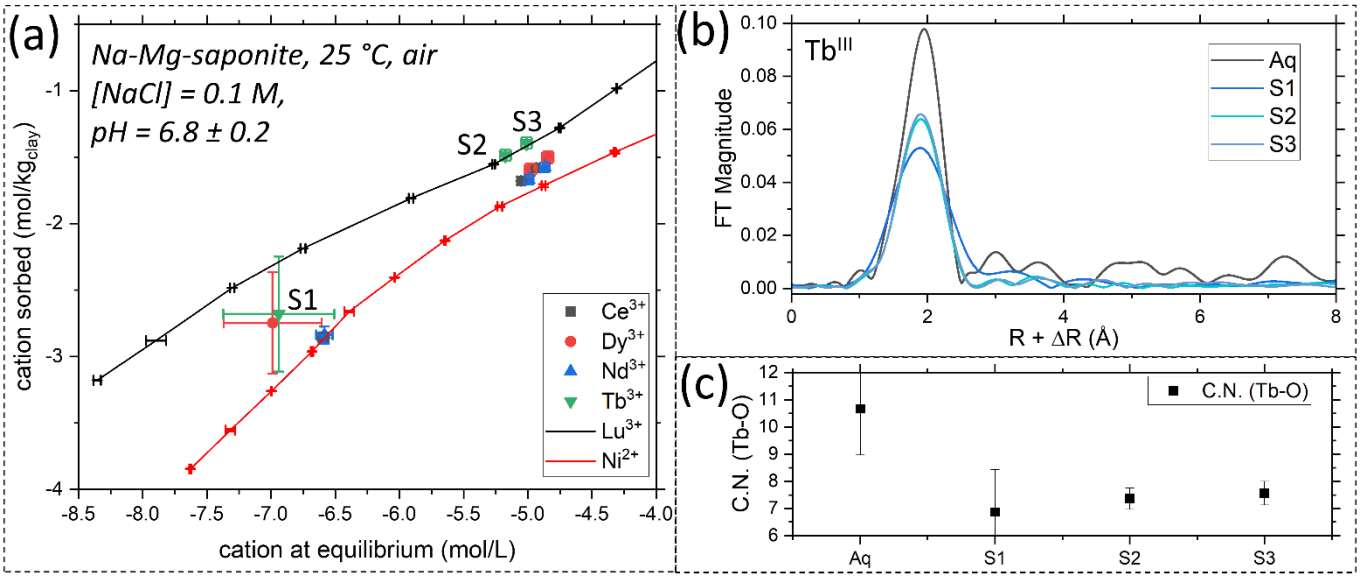

Fig. 3.10: (a) The sorption isotherms of five trivalent lanthanides and divalent nickel by saponite. (b) Radial distribution functions obtained from Fourier transforms of cubic chi functions of four different Tb-bearing samples; the aqueous ion is compared with three incremental amounts of sorbed terbium. (c) Coordination numbers obtained from fitting with Artemis of these four samples.

The sorption behaviour shown by REEs with common industrial products such as saponite seems promising for the recovery of REEs from aqueous wastes. The high sorption occurring at weak sites of saponite particle edges could enable sorption of large amounts of REEs, isolating the lanthanides from the aqueous matrix. Such REEs could be successively separated by the clay through an exchange reaction with another ion (e.g., nickel) that could reach more stable positions at the edge of clay particle, compromising the ability of the REEs to remain bound to the weak sites.

Advances have been made also towards the atomistic modelling of sorption and the simulation of the experimental EXAFS results. The simulations performed for saponite samples with Ni^{2+} incorporated shown good agreement between experimental and theoretical spectra. This supports the combined use of ab initio molecular dynamics simulation and theoretical modelling of EXAFS spectra for interpretation of experimental XAS data. The linear combination fitting for Ni sorption samples were performed considering the strong and weak sites on (100) and (130) talc edge surfaces. This approach shows some level of agreement, although certain features were missing. Some disagreements were explained by topographic observations with the atomic force microscope (AFM), which indicated that other surfaces are more relevant for saponite than the previously suggested (100) and (130).

Further simulations using the Wulff construction method (Rahm & Erhart 2020) confirmed that (010) and (110) are indeed the most stable surfaces. New atomistic models were constructed and scheduled to test the influence of the different surface selection. A research article, where we describe in detail the sorption of nickel by saponite, is currently under revision in Geochimica et Cosmochimica Acta.

3.7 References

Baeyens B., Bradbury M.H. (1997)
A mechanistic description of Ni and Zn sorption on na-montmorillonite. Part I: Titration and sorption measurements. Journal of Contaminant Hydrology, 27(3–4), 199–222.

Bestel M., Glaus M.A., Frick S., Gimmi T., Juranyi F., Van Loon L.R., Diamond L.W. (2018)
Combined tracer through-diffusion of HTO and ^{22}Na through Na-montmorillonite with different bulk dry densities. Applied Geochemistry, 93, 158–166.

Bourg I.C., Lee S.S., Fenter P., Tournassat C. (2017) Stern layer structure and energetics at mica-water interfaces. Journal of Physical Chemistry C, 121, 9402–9412.

Bradbury M.H., Baeyens B. (2009)
Sorption modelling on illite. Part II: Actinide sorption and linear free energy relationship. Geochimica et Cosmochimica Acta, 73, 990–1003.

Dähn R., Baeyens B., Bradbury M.H. (2011)
Investigation of the different binding edge sites for Zn on montmorillonite using P-EXAFS – The strong/weak site concept in the 2SPNE SC/CE sorption model. Geochimica et Cosmochimica Acta, 75(18), 5154–5168.

Dähn R., Baeyens B., Marques Fernandes M. (2021) Zn uptake by illite and argillaceous rocks. Geochimica et Cosmochimica Acta, 312, 180–193.

Dähn R., Scheidegger A.M., Manceau A., Schlegel M.L., Baeyens B., Bradbury M.H., Chateigner D. (2003)
Structural evidence for the sorption of Ni(II) atoms on the edges of montmorillonite clay minerals: a polarized X-ray absorption fine structure study. Geochimica et Cosmochimica Acta, 67(1), 1–15.

Glaus M.A., Aertsens M., Appelo C.A.J., Kupcik T., Maes N., Van Laer L., Van Loon L.R. (2015)
Cation diffusion in the electrical double layer enhances the mass transfer rates for Sr^{2+}, Co^{2+} and Zn^{2+} in compacted illite. Geochimica et Cosmochimica Acta, 165, 376–388.

Glaus M.A., Frick S., Rossé R., Van Loon L.R. (2010) Comparative study of tracer diffusion of HTO, $^{22}Na^{+}$ and $^{36}Cl^{-}$ in compacted kaolinite, illite and montmorillonite. Geochimica et Cosmochimica Acta, 74, 1999–2010.

Glaus M.A., Frick S., Rossé R., Van Loon L.R. (2020) A coherent approach for cation surface diffusion in clay minerals and cation sorption models: Diffusion of Cs^{+} and Eu^{3+} in compacted illite as case examples. Geochimica et Cosmochimica Acta, 274, 79–96.

Lan Y.Q., Li C., Mao J.D., Sun J. (2008)
Influence of clay minerals on the reduction of Cr^{6+} by citric acid. Chemosphere, 71, 781–787.

Li C.C., Wang Y.J.，Du H.，Cai P.，Peijnenburg WJGM，Zhou D.M. (2017)
Influence of bacterial extracellular polymeric substances on the sorption of Zn on γ-alumina: A combination of FTIR and EXAFS studies. Environmental Pollution, 220, 997–1004.

Nelson J., Wasylenki L., Bargar J.R., Brown Jr. G.E., Maher K. (2017)
Effects of surface structural disorder and surface coverage on isotopic fractionation during Zn(II) adsorption onto quartz and amorphous silica surfaces. Geochimica et Cosmochimica Acta, 215, 354–376.

Qian Y., Scheinost A.C., Grangeon S., Greneche J.-M., Hoving A., Bourhis E., Maubec N., Churakov S.V., Fernandes M.M. (2023)
Oxidation state and structure of Fe in nontronite: From oxidizing to reducing conditions. ACS Earth and Space Chemistry 7, 1868-1881.

Rahm J.M., Erhart P. (2020)
WulffPack: A Python package for Wulff constructions. The Journal of Open Source Software 5(45), 1944.

Van Loon L.R. (2014)
Effective diffusion coefficients and porosity values for argillaceous rocks and bentonite: measured and estimated values for the provisional safety analyses for SGT-E2. Nagra Technischer Bericht, NTB 12-03.

Van Loon L.R., Mibus J. (2015)
A modified version of Archie's law to estimate effective diffusion coefficients of radionuclides in argillaceous rocks and its application in safety analysis studies. Applied Geochemistry, 59, 85–94.

Van Loon L.R., Glaus M.A., Wüst R. (2023)
Diffusion of HTO, $^{36}Cl^{-}$ and $^{22}Na^{+}$ in the Mesozoic rocks of northern Switzerland: I: Measurement of diffusion coefficients and capacity factors. Applied Geochemistry 159, 105843.

Waychunas G.A., Fuller C.C., Davis J.A. (2002) Surface complexation and precipitate geometry for aqueous Zn(II) sorption on ferrihydrite I: X-ray absorption extended fine structure spectroscopy analysis. Geochimica et Cosmochimica Acta, 66(7), 1119–1137.

4 CEMENTITIOUS REPOSITORY FOR RADIOACTIVE WASTE

Provis J.L., Churakov S.V., Curti E., Griffa M., Guillemot T., Kunz D., Laube A., Lechleitner F., Ma B., Szidat S., Tits J., Wieland E., Wang D. (postdoc), Ban J. (PhD student), Bayram S.E. (PhD student)

4.1 Introduction

In the design of the Swiss deep geological repository for radioactive waste, a large amount of cementitious material will be used for the construction of the L/ILW cavern as well as for the conditioning of wastes and the backfilling of the cavern. The cementitious material contains a high proportion of Portland cement (PC), which hydrates to form space-filling, durable silicate and aluminate minerals with high surface area. Cementitious materials influence the geochemical conditions in the near field and contribute to the retention and slow release of radionuclides: 1) They create a high pH environment that ensures low solubility for much of the radionuclide inventory and contributes to the passivation of, steel contributing to low metal corrosion rates. 2) The alkaline near field creates hostile conditions for microbial activity. 3) Many radionuclides are strongly bound to cement minerals, reducing the concentrations in the cement pore waters (CPW) and thus radionuclide mobility.

The sorption values of safety-relevant radionuclides on hardened cement paste (HCP) are therefore key input data for the calculation of the radionuclide release from the L/ILW near field as part of the dose calculations that Nagra will perform for the safety analysis as part of the general license application. Data from the open literature combined with results from in-house research were used to select sorption values as outlined in section 4.2, taking into account current information on the waste inventories and the repository design. The updated cement sorption database (SDB) is the latest in a longstanding series describing the cementitious near field of L/ILW and ILW repositories.

Within the context of a cementitious repository, gas generation through corrosion of irradiated steel waste components is likely to be important in defining the nature and mobility of species containing ^{14}C, in both gaseous and aqueous forms. The long-running LOMIR experiments in LES are described in section 4.3, with key implications for ^{14}C inventory management and release rates in a repository.

Radiosotopes of silicon, aluminium and calcium have also recently been identified as potentially important dose-relevant radionuclides. However, the kinetic data for the uptake and release of these elements in a repository context have previously been lacking. Section 4.4 describes the outcomes of LES experimental work aimed at identifying and quantifying the mobility of ^{32}Si, ^{45}Ca, $^{35}SO_4^{2-}$ and $^{14}CO_3^{2-}$ by cement hydrates, which provides an important new contribution to the prediction of repository performance.

Quantitative data regarding the temporal evolution of poro-mechanical properties, along with qualitative information on chemical and microstructural changes in cementitious systems under conditions pertinent to Swiss geological disposal, is crucial for assessing repository safety. The objective described in section 4.5 involves conducting a time-lapse, chemo-poro-mechanical characterisation of mortars containing fine aggregates undergoing accelerated degradation in the laboratory, influenced by their interaction with the pore solution of Opalinus Clay. This task is a part of the EURAD MAGIC work package. The mortar types used mirror those employed in specimens cast in 2012 during the CI experimental campaign at the Mt. Terri Underground Rock Laboratory, aiming to construct lab-scale mock-ups replicating field experiment conditions.

The Cement Systems group has been joined in 2023 by a new Group Leader, Prof. Dr. John L. Provis, who has relocated from the University of Sheffield (UK) to take up this role within LES. Prof. Provis brings a background in cementitious materials science and engineering, and will lead new strategic developments in the scientific directions of the Cement Systems group, as described in section 4.6. The group will maintain and further strengthen its focus on delivering the practical outcomes and insight needed to support the core mission of geological disposal of radioactive waste in Switzerland, underpinned by fundamental science and innovation in the design, characterisation, and use of cementitious materials.

4.2 Nagra PSI cement sorption database: an update

Many radionuclides are strongly bound to cement minerals, reducing the concentrations in the cement pore waters (CPW) and thus radionuclide mobility. The sorption values of safety-relevant radionuclides on hardened cement paste (HCP) are key input data for the

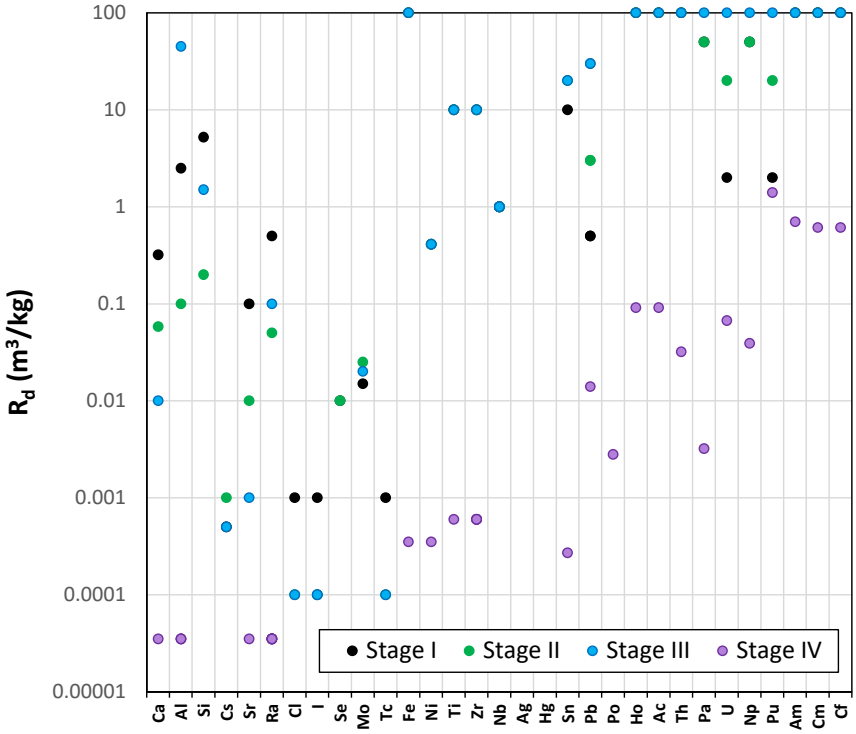

Fig. 4.1: Selected data from the updated Cement Sorption Database, showing recommended R_d values for selected elements under oxidising conditions. Full data sources are tabulated in Tits & Wieland (2023). Note that the full database also contains upper and lower bound values for each entry; these are not plotted here for visual clarity.

calculation of the radionuclide release from the L/ILW near field as part of the dose calculations that Nagra will perform for the safety analysis as part of the general license application. The updated cement sorption database (SDB) is the latest in a longstanding series; Wieland (2014) developed a SDB (CEM-14 SDB) for cementitious systems as an update of previous SDBs prepared by Wieland & Van Loon (2002) (referred to as CEM-02), Bradbury & Van Loon (1997) (referred to as CEM-97) and Bradbury & Sarott (1994) (referred to as CEM-94) for the cementitious near field of L/ILW and ILW repositories.

Based on the literature and data assessment as summarised (and exemplified) below, and the simulation of cement hydrate phase assemblages and pore fluid chemistry, the full updated cement SDB (Tits & Wieland 2023) describes R_d values and modifying factors for more than 30 elements, under oxidising and reducing conditions, and for all four stages of cement degradation under repository conditions. Figure 4.1 shows a subset of the database, focusing on inorganics under oxidising conditions, and exemplifies the range of values obtained. There are clearly striking differences in the interactions of different radioelements with C-S-H and other relevant cement hydrates, even for elements of similar charge state, which emphasises the importance of using appropriately derived, selected and curated data for repository performance prediction. It is hoped that the updated Nagra-PSI cement SDB provides a substantial contribution to national and international efforts in this regard.

4.2.1 Database structure and focus

The sorption values listed in the SDB are defined in terms of a distribution ratio, R_d, accounting for partitioning according to Eq. 4.1:
This expression gives an overall measure of the disappearance of the radionuclide from solution due to uptake by the solid; the difference between the initial radionuclide activity added to the cementitious system

$$R_d = \frac{\text{Quantity of a radionuclide sorbed per unit mass cement}}{\text{Equilibrium concentration of the radionuclide in porewater}} \left(\frac{m^3}{kg}\right) \quad (1)$$

and the final activity in solution. However, this does not provide specific information on the uptake mechanism, which must obtained from additional wet chemistry investigations, such as measurements at increasing solute concentrations (isotherms) and reversibility tests, or spectroscopic investigations on the coordination environment of the sorbate. Therefore, the mechanisms of the radionuclide sorption on cement paste and cement phases are often poorly known and/or disputed. In this SDB, an attempt is made not only to assign R_d values to each radionuclide, but also to consider the radionuclide uptake process itself and the cement phases responsible for the uptake processs. Reduction in sorption due to the presence of complexing ligands (formation of water-soluble complexes), colloids (which can associate with radionuclides, leading to increased radionuclide mobility) or due to sorption competition can affect radionuclide sorption and thus reduce the R_d value. The SDB therefore also tabulates reduction factors that describe the impacts of these different mechanisms on observed sorption behaviour.

In previous SDBs, the sorption values were selected by taking into account the three main stages of the cement degradation. Briefly, the stages can be characterised as follows: In stage I, the composition of cement pore water is dominated by the release of alkali hydroxides (NaOH, KOH), which results in a pH of ~ 13.3. In stage II, the chemical composition of the alkali-depleted CPW is controlled by the solubility of portlandite, which fixes $[Ca]_t$ at ~ $2 \cdot 10^{-2}$ M and pH at ~ 12.5. Stage III is reached when the portlandite is completely dissolved, and so the calcium silicate hydrate (C-S-H) phases dissolve incongruently, which results in a pH decrease from 12.5 to 10. This means that the Ca and Si concentrations in CPW vary depending on the chemical composition of the C-S-H phases, in particular the Ca/Si (C/S) ratio. As a new addition in the updated SDB, stage IV of the cement degradation is also considered. Stage IV is reached when all Ca-bearing cement phases (portlandite, C-S-H, AFt, AFm) are dissolved. The matrix is thus dominated by carbonate and/or clay minerals.

The dose-relevant radionuclides were selected by analysis of the waste streams including a re-assessment of radionuclide inventories and simplified transport calculations. The radionuclides belong to the element groups listed in Table 4.1. New elements have been added to the list of dose-relevant radionuclides (^{26}Al, ^{41}Ca, $^{249/251}$Cf, ^{60}Fe, ^{194}Hg, ^{166m}Ho, ^{32}Si) due to a new selection procedure resulting from transport calculations for RBG (Nagra 2019). The dose-relevant radionuclides in L/ILW include all actinides and their daughters with long half-lives, as well as activation and fission products.

4.2.2 Reassessment of cement hydrate chemistry

The composition of HCP in all stages of the cement degradation must be taken into account when assigning sorption values. The main development presented in the updated SDB is the exclusion of AFm phases, which can be attributed to the new thermodynamic data available for Si/Al siliceous hydrogarnet (Dilnesa et al. 2014; Lothenbach et al. 2019). Updated modelling shows that Al/Fe siliceous hydrogarnet is the most thermodynamically stable Al/Fe-containing cement phase, which is formed at the expense of AFm phases. AFm phases are only present in the form of monocarbonate in stage II and are not present at all in stage I and stage III. It should be noted that thermodynamic modelling determines the thermodynamically most stable composition of hardened cement paste (HCP), which is considered representative in the long term in a deep geological repository. This means that AFm phases can be observed experimentally in fresh HCP due to kinetic control of phase formation, but are not expected to persist in HCP aged for hundreds or thousands of years.

In stage III the C-S-H phases, calcite, and zeolites are the predominant minerals according to the current model of the cementitious system. In contrast to

Tab. 4.1: Dose-relevant radioelements considered in the updated cement SDB. Note that carbon is considered in both organic and inorganic forms, and redox-active elements are assessed under both reducing and oxidising conditions at high alkalinity.

Group 1, 2 and 13 elements	Cs, Ca, Sr, Ra, Al
Transition elements (first to third period)	Ti, Fe, Ni, Zr, Nb, Mo, Tc, Ag, Hg
Group 14, 16 and 17 elements	C, Si, Sn, Pb, Se, Po, Cl, I
Lanthanoids and actinoids	Ho, Ac, Th, Pa, U, Np, Pu, Am, Cm, Cf

previous modelling, ettringite is predicted to be thermodynamically stable in stages I and II, while it is unstable in stage III as Al is preferentially accommodated by zeolites. It should be noted that C-S-H phases and calcite are the only minerals present in all of the first three stages of cement degradation.

In previous SDBs, AFm phases were considered to be an important cement phase for anion retention (Wieland 2014). In the current evaluation of sorption values, it is considered that AFm phases are only present in the form of monocarbonate in DS-II. It is known that AFm phases show a strong preference for CO_3^{2-} anions in their interlayers compared to other anions, and so monocarbonate is not considered a good sorbent for anions and is not discussed further in the present SDB for the long-term retention of anionic radioelements in a deep geological repository.

This new assessment of the composition of the cement matrix requires C-S-H phases and ettringite to be considered as the relevant cement phases contributing to anion retention. Improved knowledge of the long-term evolution of the mineral composition of degrading cementitious matrices, in particular the absence of AFm phases, requires a re-evaluation of anion retention for the development of the new cement SDB, focused on the role of C-S-H.

4.2.3 Critical assessment of literature data for the SDB: The example of iodide

The present update of sorption values has been made with reference to the previous CEM-94, CEM-97, CEM-02 and CEM-14 SDBs. Sorption values were revised when new information and/or data became available that allowed changes or re-appraisals of the data compared to previous SDBs. The sorption values have been selected either on the basis of i) in-house experimental data that are available, ii) survey of sorption values in the open literature, or iii) chemical analogy.

The sorption values were divided into three categories for the development of the updated cement SDB:

- Not re-assessed, not revised: No new information and experimental data are available; sorption values listed in CEM-14 were not revised.
- Re-assessed, not revised: New and relevant information and experimental data are available, but do not require a revision of the sorption values as listed in CEM-14. The values are, if necessary, only adjusted according to the different solid and pore water compositions considered.
- Re-assessed, revised: New and relevant information and experimental data are available that allow a re-evaluation of the sorption values previously recommended in CEM-14. The values were revised in accordance with the new experimental data and/or based on a more in-depth knowledge of the sorption process under the different pore water compositions of the reference systems considered.

As an example of the processes followed to assess and select data for one element in developing the cement SDB, the case of iodide is briefly summarised here.

Since the publication of NTB 14-08 (Wieland 2014), new research results have been published in the open literature. These new data largely support the process understanding obtained for I^- binding by cementitious materials presented in NTB 14-08 (Wieland 2014). Two main processes may potentially control I^- binding by cementitious materials: 1) exchange with anions in AFm phases, which form extensive solid solutions in some cases involving iodides, but notably not in the case of monocarbonate-AFm, as shown by Nedyalkova et al. (2020; 2021; 2022); and 2) electrostatic adsorption onto the positively charged surface sites of C-S-H phases.

The difference in the cement mineralogy between NTB 14-08 (Wieland 2014) and the updated cement SDB also plays an important role in the selection of I^- R_d values. The content of AFm phases in the cement matrices calculated with the new CEMDATA 18.1 database is negligible, and so it is now considered that AFm phases do not play a role in anion sorption in aged cementitious systems. This means that the selection of R_d values for I^- uptake by HCP for the updated cement SDB must be based on uptake by C-S-H phases, in Stages I-III of cement degradation.

Therefore, it is proposed to select the I^- R_d values for the updated cement SDB as follows:

Stage I: We select the same R_d values for $^{129}I^-$ sorption as previously assigned to $^{36}Cl^-$ sorption, which means that the R_d value selected in NTB 14-08 (Wieland 2014) can be retained ($R_d = 10^{-3}$ m^3/kg).

Stage II: The Cl^- concentration of the Stage II pore water is expected to be high, and the sorption behaviour of $^{36}Cl^-$ and $^{129}I^-$ will be similar at high salinity. So, it is recommended to reduce the R_d value for Stage II given in NTB 14-08 (Wieland 2014) by a factor of 10 to $R_d = 10^{-4}$ m^3/kg, corresponding to the R_d value of Cl^-.

Stage III: Consistent with Stage II, we assign the same sorption values to $^{36}Cl^-$ and $^{129}I^-$ for DS-III ($R_d = 10^{-4}$ m^3/kg). Thus, the previously selected R_d value of zero in NTB 14-08 for DS-III (Wieland 2014) is revised in the current version of the cement SDB due to the high Ca concentration and the related positive surface charge of C-S-H phases under the expected near-field conditions.

4.3 IGD-TP project: "Long-term monitoring of C-14 compounds released during corrosion of irradiated steel" (LOMIR)

The objective of the project LOMIR is to gain insight in the speciation of ^{14}C-bearing compounds released during anoxic corrosion of irradiated steel under hyperalkaline conditions existing in the cementitious near field of a deep geological repository for low and intermediate level radioactive waste (L/ILW DGR). In 2016 PSI set-up a long-term corrosion experiment with an irradiated stainless steel nut from the Gösgen nuclear power plant (Switzerland) to monitor the ^{12}C- and ^{14}C-compounds released under conditions relevant to a L/ILW DGR. Briefly, two 2 mm thick slices of an irradiated steel guide tube nut from the Gösgen nuclear power plant (Switzerland) were immersed in a synthetic, highly alkaline, aged cement pore water (ACW) in a gas-tight stainless steel pressure reactor, under N_2 (Guillemot et al. 2021; Guillemot et al. 2022; Tits et al. 2023). Analysis is conducted by high performance ion exchange chromatography coupled to mass spectrometry (HPIEC-MS) and gas chromatography coupled to mass spectrometry (GC-MS). Analytical tools were optimised for the identification and quantification of the ultra-low concentrations of dissolved and gas-phase compounds: individual ^{14}C-compounds in both solution and gas phase are determined using compound-specific radiocarbon analysis based on chromatographic separation techniques combined with accelerator mass spectrometry (AMS) measurements and determination of total organic and inorganic carbon (TOC and TIC respectively). A complete mass balance of the ^{14}C in the experiment could thus be calculated after each sampling.

This report describes the results of the sampling campaign carried out in February 2023 and compares these with the earlier results (Tits et al. 2023).

4.3.1 Total release of compounds of interest

The evolution of the stable ^{12}C release in solution and in the gas phase during corrosion of the steel nut shows a fast initial release during the first 30 days, identified both in solution and in the gas phase, followed by a much slower release continuing for almost 3 years. Beyond this time period, the amounts of ^{12}C in solution and in the gas phase remain roughly constant.

In Figure 4.2, ^{14}C release into the liquid and gas phases is shown as function of the experiment time, both for measurement of the $TO^{14}C$ without sample pre-treatment (direct $TO^{14}C$), and with the sample pre-treated by passage through an ion-exchange Ag/Ba/H cartridge prior to the $TO^{14}C$ analysis. The analysis of the samples taken in 2023 confirm the long-term trends described in Tits et al. (2023): the results measured after cartridge pre-treatment show an initial fast release of ^{14}C to the liquid phase during the first 30 days. After this, the concentrations of dissolved ^{14}C-organics stabilise with time (Figure 4.2a). Long-term $TI^{14}C$ measurements indicate constant amounts in solution after three years of alkaline anoxic corrosion (Figure 4.2b). Overall, the evolution of the $TI^{14}C$ concentration in solutions is similar to that of the $TO^{14}C$ concentration.

In contrast to the evolution of the concentrations of ^{14}C compounds in solution, the amounts of ^{14}C released to the gas phase slightly increase with time (Figure 4.2c). In addition to the evolution of the concentrations of ^{14}C compounds in the gas phase, the concentration of H_2 released to the gas phase during corrosion was also monitored (Figure 4.2d). H_2 production is widely used as an indicator for the corrosion of steel and iron under anoxic conditions. Despite a large scatter due to the difficulties in measuring low concentrations of H_2 by GC-MS, H_2 concentrations seem to show a small increase following a predicted corrosion rate of 1 nm/a (Figure 4.2d). Further samplings are needed to confirm this statement. The ^{14}C release is well described by a model assuming a 2-step release scenario including a fast release during the first 30 days (corrosion rate of 20 nm/a), followed by a slow release, assuming a corrosion rate of 1 nm/a.

The rapid initial release of ^{14}C into solution followed by a stagnation of the ^{14}C amounts in solution suggests that dissolved ^{14}C-compounds were originally weakly bound in the oxidation layer of the steel matrix and quickly released as soon as the metal was in contact with solution. After the first 30 days, $TO^{14}C$ concentrations remain constant in solution, while the total amount of ^{14}C released to the gas phase ($TG^{14}C$) slightly increases with time, following a modelled corrosion rate of 1 nm/a (Figure 4.2c).

4.3.2 Distribution of individual species

The identification of individual dissolved ^{14}C-compounds was determined with AMS-based CSRA, starting after 1252 days of corrosion. Concentrations of ^{14}C-bearing carbonates ($^{14}CO_3^{2-}$) and five different ^{14}C-bearing carbonic acids (CAs): formic acid (FA), acetic acid (AA), oxalic acid (OA), malonic acid (MA), and lactic acid (LA) are quantified in Figure 4.3.

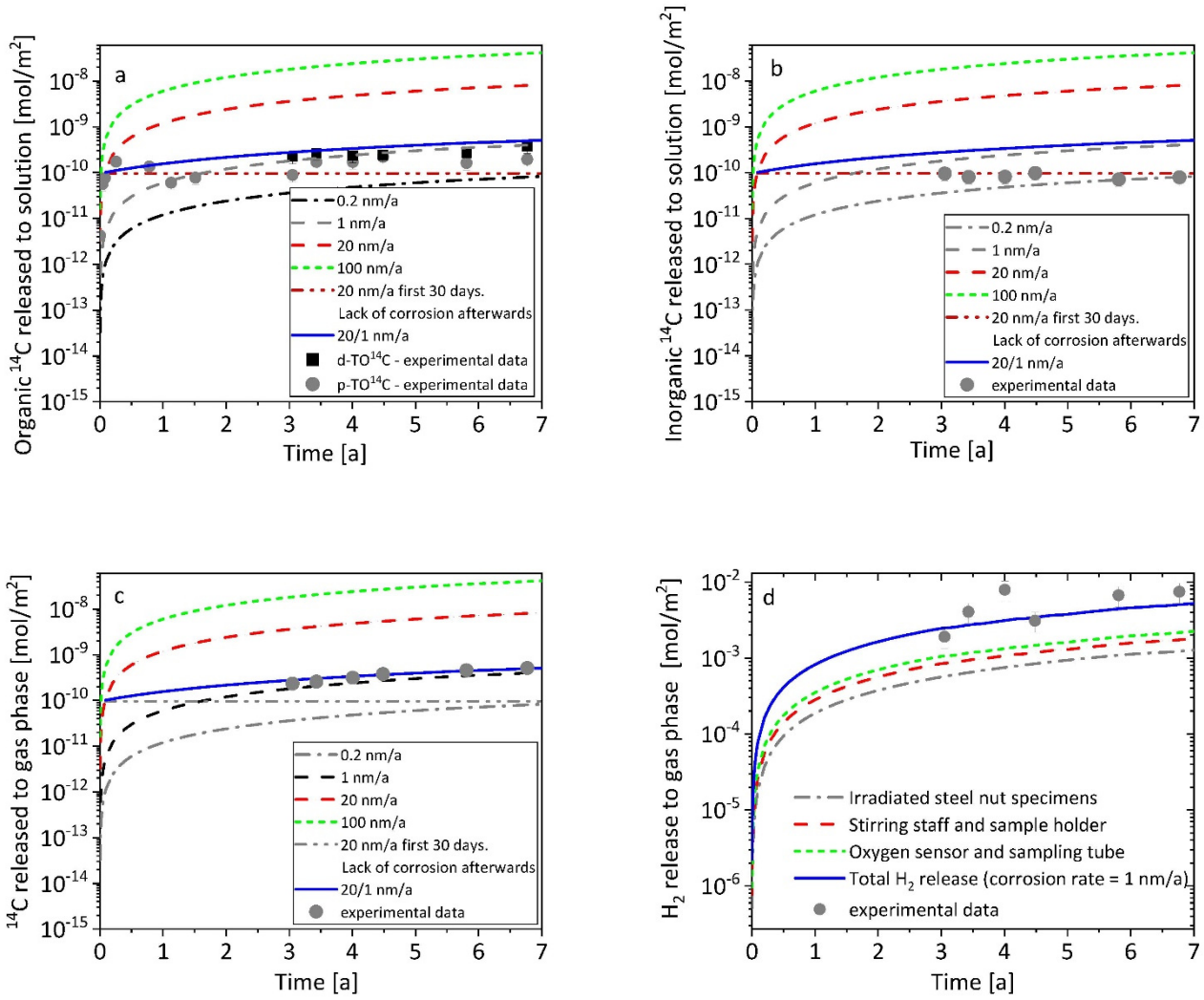

Fig. 4.2: Temporal evolution of (a) d–TO^{14}C and p-TO^{14}C; (b) TI^{14}C; (c) gaseous ^{14}C; and (d) H_2 during the corrosion of two irradiated steel specimens in an aged cement pore water (pH = 12.5, [Ca] = 2·10^{-2} M) under N_2 atmosphere. Comparison of the experimental data with model predictions in a,b,c is based on three different scenarios: 1) Continuous release with different corrosion rates varying between 0.2 nm/a and 100 nm/a; 2) A fast release assuming a corrosion rate of 20 nm/a during the first 30 days and no release thereafter; 3) A 2-step release scenario including a fast release the first 30 days (corrosion rate = 20 nm/a) and a subsequent slower release, assuming a corrosion rate of 1 nm/a. Uncertainty in experimental data is ± 30%.

Approximately 75 % of the dissolved ^{14}C-compounds are organics and the remaining 25 % are carbonates (Figure 4.3a). The five CAs identified in solution make up about 60 % of the ^{14}C-organics while the remaining 40 % remain unknown, Figure 4.3b. FA and AA make up the largest part of the CAs.

^{60}Co, the main activation product in activated steels, was originally expected to be released congruently with progressing corrosion under the assumption that it is homogeneously distributed in the pristine steel matrix. This would make ^{60}Co an interesting proxy for corrosion rate measurements. At the start of the corrosion experiment, a ^{60}Co activity of approximately 1.5·10^6 Bq m^{-2} was measured (Figure 6). During the first 3 years of corrosion, the ^{60}Co activity decreased by at least a factor of ten, falling below the detection limit of the gamma counter used. During the last two sampling campaigns, the ^{60}Co activity was additionally measured by γ -spectrometry, with a further factor of three greater sensitivity. Despite the use of this more sensitive equipment, no ^{60}Co could be detected. This could be explained by the precipitation of ^{60}Co as a hydroxide in alkaline environment, or by sorption on the iron oxides in the corrosion layer.

Figure 4.4 gives a more detailed picture of the composition of the gas samples collected after 2470 days; the relative composition of the earlier samples is similar. The main ^{14}C-containing species is $^{14}CH_4$, making up 85 % to 92 % of the TG^{14}C. It has been proposed that a Fischer-Tropsch-type (FT) process is responsible for the formation of hydrocarbons during the corrosion of iron in similar experimental conditions (i.e. anoxic atmosphere, highly alkaline solution, temperature of 25°C) (Cvetković et al. 2018; Guillemot et al. 2020), and so this is the most likely hypothesis to explain the behaviour observed here.

After 2470 days of corrosion under anoxic alkaline conditions, a total of 0.003 % of the initial ^{14}C inventory has been released to the solution and gas phases. The experiment remains ongoing.

4.4 Uptake of ^{32}Si, ^{45}Ca, $^{35}SO_4^{2-}$ and $^{14}CO_3^{2-}$ by cement hydrates

In a recent evaluation, Nagra identified ^{26}Al, ^{32}Si, and ^{41}Ca as new dose relevant radionuclides for the safety assessment of a future low and intermediate level (L/ILW) radioactive waste repository in Switzerland. Little or no research has been published in the literature on the retention of these radionuclides by cementitious materials. The aim of this study was, on the one hand, to determine ^{26}Al, ^{32}Si and ^{41}Ca sorption values (R_d, L kg^{-1}) for the main cement phases and for hardened

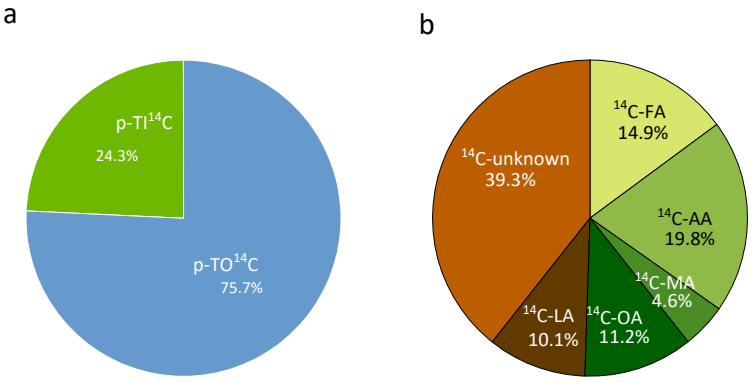

Fig. 4.3: ^{14}C composition of the liquid phase (average values obtained over different time periods, according to methodological development). a) Distribution of inorganic and organic carbon compounds in solution after cartridge pre-treatment and before injection in ion-chromatography between 1114 and 2470 days of corrosion. b) Distribution of the ^{14}C-CAs and the unidentified ^{14}C-organics measured between 552 and 2470 days of corrosion.

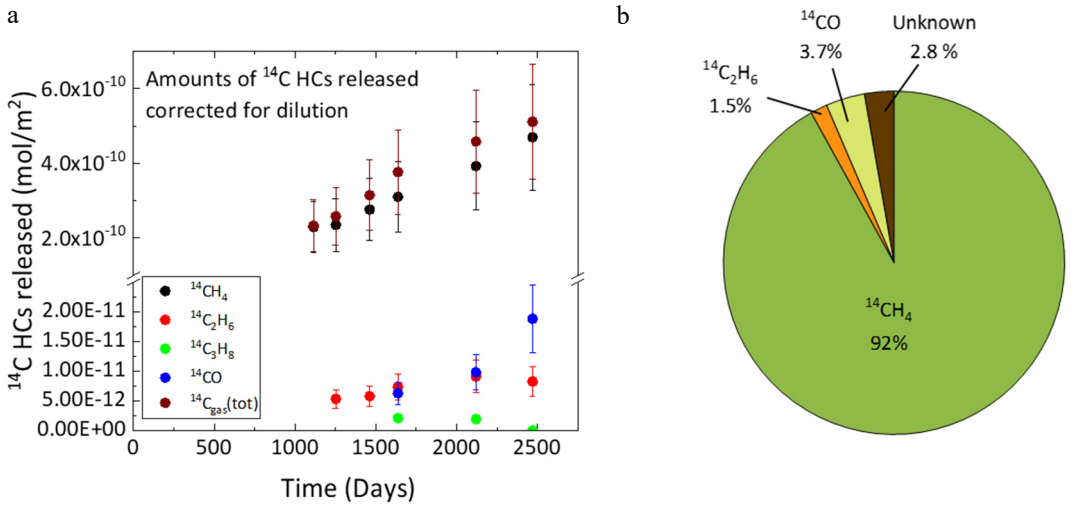

Fig. 4.4: (a) Evolution of the amount of ^{14}C HC released to the gas phase as function of time; data corrected for dilution, expressed in mol/m$^{2;}$ (b) ^{14}C distribution in the gas phase after 2470 days (b) of corrosion in alkaline anoxic conditions.

cement paste, for inclusion into the cement sorption database (described in section 4.2), and also to gain insight into the processes controlling the sorption of these radionuclides onto cementitious materials. This may take place through surface processes such as surface complexation or ion exchange, and also by isotopic exchange during dissolution-precipitation (recrystallisation) reactions. The former processes are fast, taking hours to a few days, whereas the latter are much slower, taking up to several years.

The sorption kinetics of ^{32}Si, ^{45}Ca (as an analogue for ^{41}Ca), $^{35}SO_4^{2-}$ and $^{14}CO_3^{2-}$ onto key cement hydrate products, and onto HCP, were investigated in batch sorption experiments. Additionally, experiments with $^{35}SO_4^{2-}$ and $^{14}CO_3^{2-}$ have been carried out on AFm phases and ettringite. In all sorption kinetics experiments, continuous uptake over at least one year was observed. It is therefore hypothesised that the retention of ^{26}Al, ^{32}Si and ^{41}Ca by cementitious materials is controlled by isotopic exchange with stable Al, Si and Ca during recrystallisation of the main cement minerals, such as C-(A)-S-H phases (Ca, Si, Al), portlandite (Ca), ettringite (Ca, Al) and AFm phases (Ca, Al). Distribution ratios (R_d) were calculated from the observed data, as exemplified in Fig. 4.5.

Experimental data of this type can be modelled using a variety of formulations describing different underlying combinations of physical and chemical processes. The model that best describes the experimental results is the continuous homogeneous recrystallization (CHOR) model of Heberling et al. (2018), Fig. 4.6, with an additional term to describe instantaneous surface adsorption. This model defines a reaction front that travels inwards within a particle, one "monolayer" at a time, and assumes that at each time step, all layers outside the reaction front recrystallise and equilibrate with the external solution (containing the radioisotope). The time taken for a recrystallisation step to occur is proportional to the number of monolayers that participate in the recrystallisation at that time step. So, the rate of ingress of the reaction front (and thus also the shrinkage of the unreacted core of the particle) decreases as a function of time, and the radioisotope suppled initially into the solution is distributed homogeneously throughout all of the regions of the particle that have participated in the reaction up to that particular time step.

The model gave an adequate description of the experimental isotopic exchange data for ^{32}Si and ^{45}Ca in the individual hydrates, as well as part of the experimental data for $^{14}CO_3^{2-}$ and $^{35}SO_4^{2-}$, although specific ion exchange effects in the layered AFm structures complicated the analysis of anion exchange in those phases.

The model for HCP, Fig. 4.7, is constructed from the models describing individual phases, based either on the assumption that C-S-H (solid line in Fig. 4.7) or portlandite (dashed line in Fig 4.7) control the uptake processes. Fig. 4.7a demonstrates a much closer fit to the experimental data when using the assumption of C-S-H control of the reaction rates, which is potentially important and merits further investigation regarding silicate exchange rates within C-S-H phases.

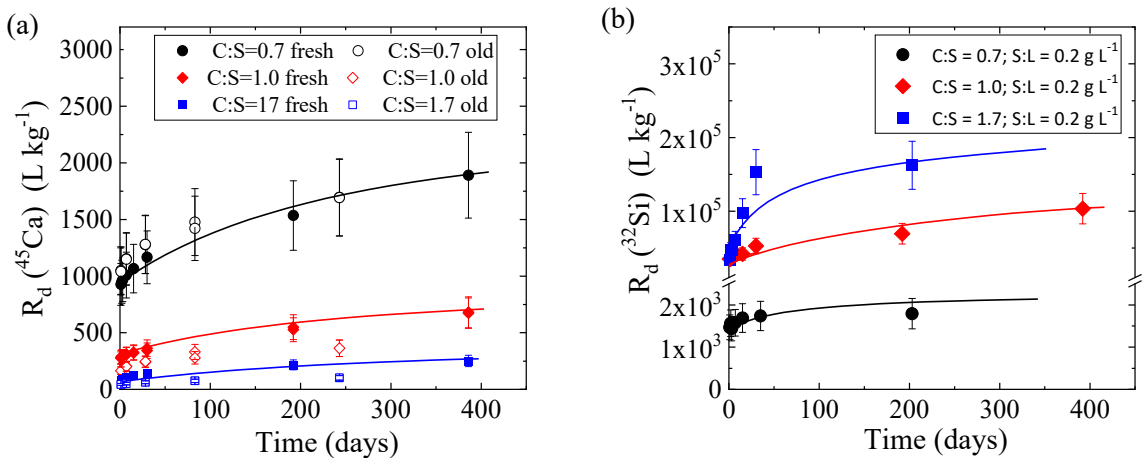

Fig. 4.5: ^{45}Ca and ^{32}Si uptake kinetics on C-S-H phases with different C:S ratios. a) Effect of C:S ratio and ageing on ^{45}Ca uptake; S:L = 10 g L^{-1} (fresh C-S-H phases) and 48 g L^{-1} (old C-S-H phases). b) Effect of the C:S ratio on the ^{32}Si uptake. Lines are added to guide the eye.

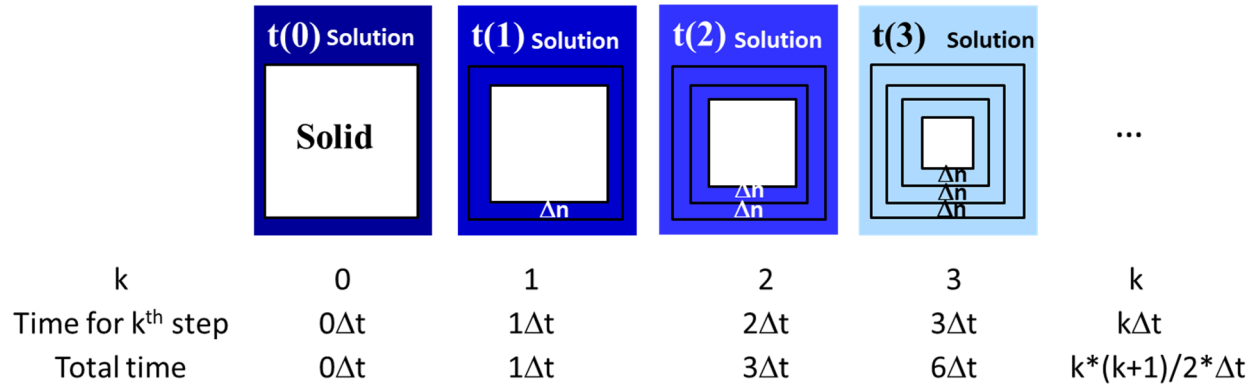

Fig. 4.6: Schematic representation of the recrystallisation kinetics applied in the CHOR model (adapted from Heberling et al. (2018)). "Δn" is the molar amount of solid corresponding to the recrystallisation of a single monolayer. "k" is the number of recrystallised monolayers, "Δt" is the time needed for the recrystallisation of the first monolayer.

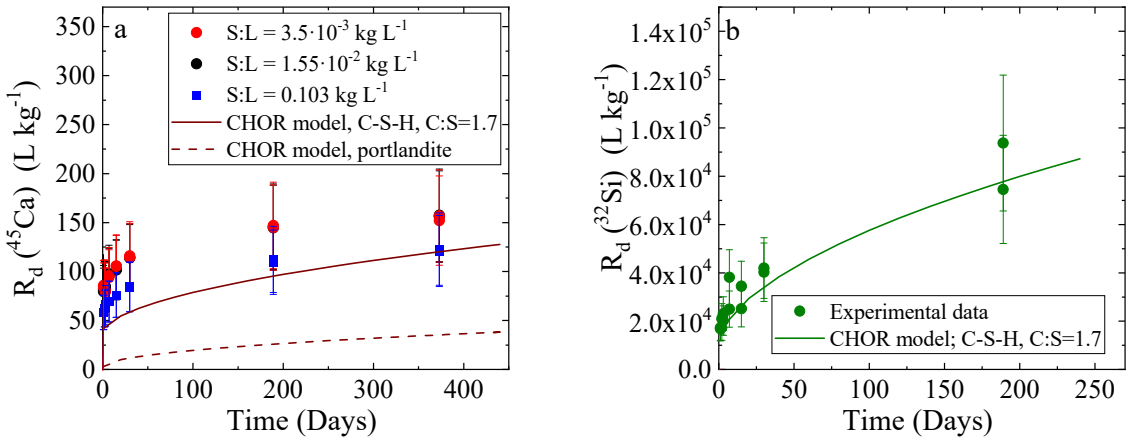

Fig. 4.7: Kinetics of uptake of (a) ^{45}Ca and (b) ^{32}Si on aged HCP at pH = 12.5. Solid lines represent the modelling results obtained with the CHOR model assuming that a C-S-H phase with a C:S ratio of 1.7 controls the ^{45}Ca and the ^{32}Si uptake. The dashed line in a) represents the modelling result obtained with the CHOR model assuming that portlandite controls the ^{45}Ca uptake.

For the assessment of the safety of a radioactive waste repository, long-term sorption values for ^{32}Si and ^{45}Ca are required. These long-term R_d values cannot be measured in the lab and have to be estimated from the appropriate recrystallisation models taking into account the chemical conditions expected in the cementitious environment of the repository. The CHOR model predicts that R_d values become constant once isotopic equilibrium between the fully recrystallised cement phase and the liquid phase is reached. These R_d values at isotopic equilibrium (R_d^{eq}) are selected for inclusion in the cement sorption database (section 4.2).

4.5 Chemo-mechanical investigation of cement degradation at repository conditions

In the framework of the EURAD project MAGIC, LES researchers, in collaboration with colleagues from Empa, are performing chemo-poro-mechanical characterisation of cementitious systems undergoing laboratory-accelerated degradation due to interactions with the pore fluid of Opalinus clay. The cementitious systems are mortars with very fine (0.1 – 0.3 mm) aggregates. A key goal of this study is to provide quantitative information on the time dependence of poro-mechanical properties, as well as more qualitative

chemical and microstructural information about the alteration of cementitious systems under conditions relevant to the Swiss geological repository.

The two mortar types are the same as for the specimens cast in 2012 during the CI experimental campaign at the Mt. Terri Underground Rock Laboratory. The investigated aged specimens were degraded for 9 years by contact with with the pore solution of Opalinus clay cores. The parallel newly-cast specimens are subjected to an accelerated, lab-scale degradation protocol: a controlled, through-diffusion experiment with a synthetic Opalinus clay pore water. Each sample is hosted inside a modified version of the diffusion cell previously developed and used at PSI (Luraschi et al. 2020; Shafizadeh et al. 2020) (see Figure 4.8). The through-diffusion experiments are conducted at 40°C, both to accelerate the degradation process, and to simulate boundary conditions closer to a repository environment.

Further, casting of small mortar specimens was optimised. Figure 4.8 shows an example of an X-ray tomogram of Portland cement mortar (w/b = 0.47) specimens, where sample casting procedures were refined to avoid entrained air (e.g. sample 3) or detachment of the material from the mould due to autogenous and drying shrinkage. The tomography measurement settings were optimised for examination of defects (e.g., boundary cracks or air voids) within the mortars, or gaps between the mortar and the mould wall, to be used for quality control before starting the full experimental campaign.

Using a first prototype of the newly designed cell and specimen 4 (which was seen to be free of evident defects), a first HTO diffusion experiment was conducted at 40°C, with the goal of assessing the suitability of the designed cell for accelerated mortar degradation. The preliminary HTO diffusion results are shown in the right column of Figure 4.8. After around 16 days, the flux in the low side reached a maximum and then decreased continuously with time. The decrease may be caused by the progress of carbonation by the carbonate-containing pore fluid, as the newly formed calcite may change the pore structure of the mortar. The latter will be the subject of investigation by time-lapse tomography measurements.

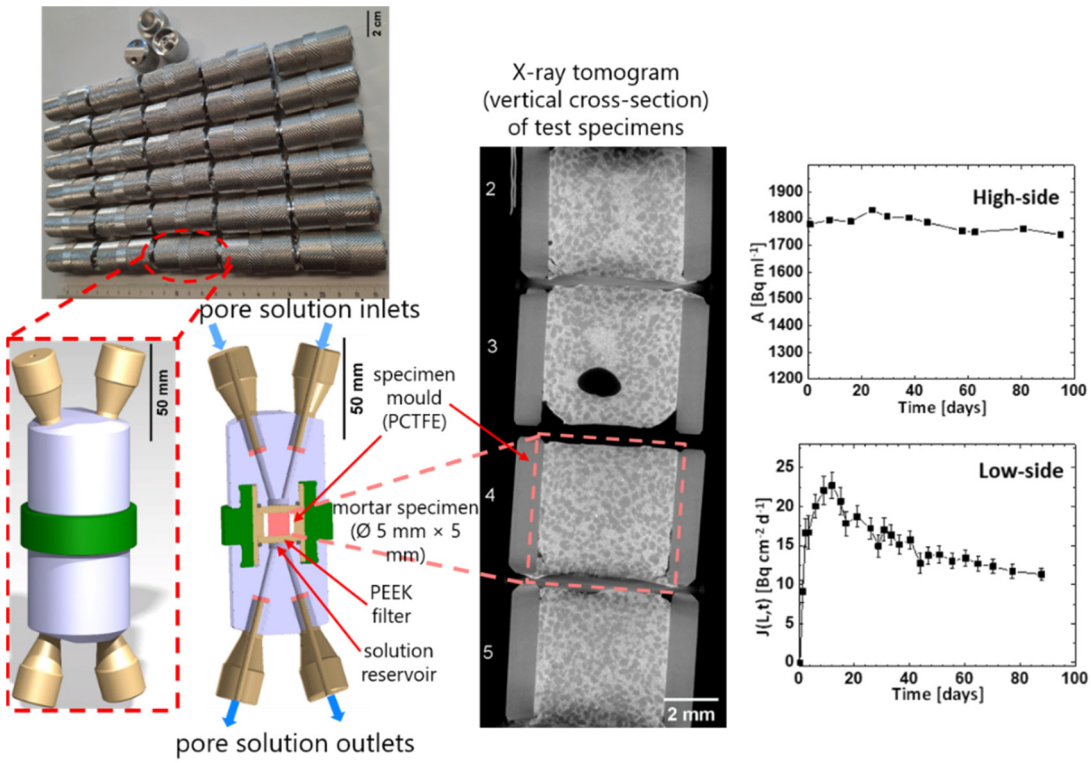

Fig. 4.8: Left column: manufactured flow cells (top photo) according to the new design (bottom drawings). Middle column: a vertical cross-section from the X-ray tomogram of four vertically stacked Portland cement mortar specimens. Right column: HTO activity (A) in the high-concentration side (top plot) and its diffusive flux density (J) at the low-concentration side (bottom plot), both as functions of time.

For each mix design, fifteen specimens were cast and are hosted inside respective cells. Three specimens are used for the mechanical characterisation, another three for diffusion coefficient measurements, and the remaining ones are intended for microstructural and chemical characterisation. Starting at approximately 10 weeks after casting, each specimen has been hosted inside a respective through-diffusion cell in contact with the Opalinus clay pore fluid, continuously circulated in upper and lower reservoirs. Each cell stays inside an oven at 40°C, hosted inside a glove box, to maintain controlled conditions. Diffusion measurements for a HTO tracer are conducted periodically (i.e., at least every 4 months) to assess the effective diffusivity and the water-accessible pore space.

The time-lapse poro-mechanical characterisation during the ongoing degradation involves measuring elastic properties, and assessing microstructure non-destructively by X-ray tomography. At the same time points, the diffusion coefficient of HTO is measured, to understand material degradation and changes in the pore structure. At four time points during the experimental campaign, one of the additional specimens will also be used for inspection of the microstructure by SEM with EDX mapping, to assess both the elemental composition and its spatial-temporal evolution. The experimental data obtained in this study are used for calibration and testing of pore scale microstructure evolution models.

4.6 New capabilities and future research direction in the Cement Systems group

4.6.1 Cement-waste compatibility and alternative cements

The cementation of low and intermediate level wastes is a key pillar in their conditioning for safe storage and disposal; in general, liquid and granular wastes are converted to solid forms to improve their safety. This is conventionally achieved using Portland cement, or blends or Portland cement with supplementary cementitious materials. However, some wastes are not conveniently compatible with the chemistry of Portland cement – for example, they may impede its setting and hardening processes – and this raises the need for the development and validation of alternative types of cement that can offer improved performance in waste cementation (Kearney et al. 2022).

One such cement type, which is gaining increasing attention for the cementation of various types of wastes including oils, reactive metals, cationic and anionic radionuclides, and granular ion exchange media, is the class of alkali-aluminosilicate "geopolymer" cements. These are under investigation in the nuclear sector, including as a major focus point in the EU *PREDIS* project and in other international partnerships. Examples of the use of geopolymer cements to treat cesium (which is only weakly retained by Portland cement hydrates) and to immobilise oils (which prevent Portland cement setting) are shown in Fig. 4.9.

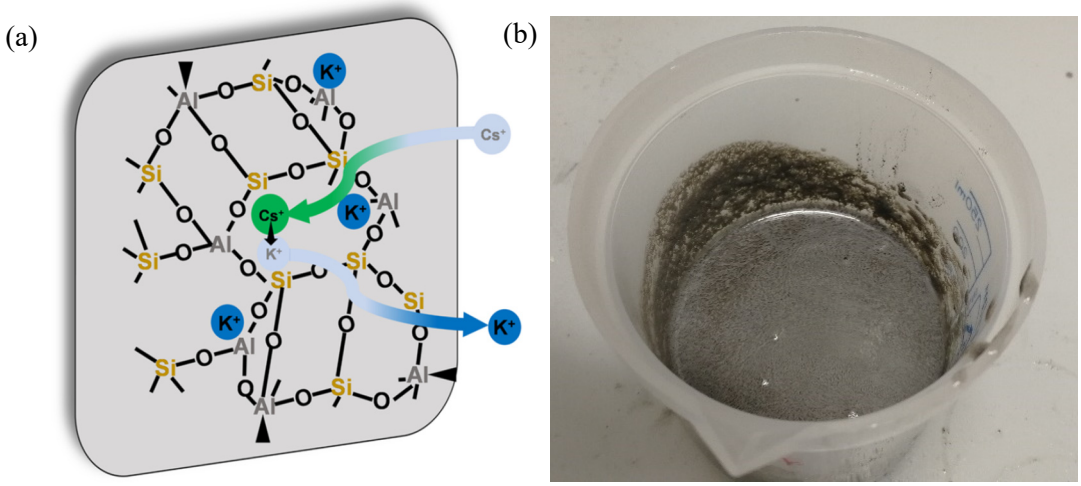

Fig. 4.9: (a) Proposed mechanism of binding of cesium in a geopolymer through ion exchange for other alkali cations (from Niu et al. (2022), reproduced under a Creative Commons CC-BY licence); (b) photograph of a geopolymer formulation containing 30 wt.% Nevastane oil, showing incorporation of oil droplets through a Pickering emulsification mechanism (from McWilliams et al. (2023), reproduced under a Creative Commons CC-BY licence).

Geopolymers are far from the only cement that is of relevance and interest in treating problematic and/or complex radioactive wastes; calcium sulfoaluminate cements (Nelson et al. 2023) and magnesia-based cements (Gardner et al. 2021) also have significant appeal in certain applications within the nuclear sector, among others. These cements also offer the possibility to produce binding materials with lower embodied CO_2 than Portland cement (Shi et al. 2019), and while it is unlikely that carbon emissions will ever be the most important criterion used in selection of a cement for waste immobilisation, it is still essential that the solutions selected for implementation at large scale are as environmentally responsible as possible. The design and environmental assessment of conventional and alternative cements is a critically important issue at present, and this provides an important opportunity for the Cement Systems Group to provide detailed and well-founded insights to partners nationally and internationally.

4.6.2 Structural evolution during cement hydration and in service

In addition to the existing strengths of LES in describing and predicting cement-waste interactions, the construction of the Swiss deep geological repository will also involve the production and emplacement of very large volumes of cementitious materials as structural concretes and as backfills. For these materials to be used effectively and efficiently, and to reduce the possibility of undesired behaviour (particularly cracking), it is essential to be able to predict their evolution – in terms of the pore fluid chemistry, the mineralogical makeup of the hydrate phase assemblages, porosity and pore size distributions, and the influence on each of these factors of interactions with the surrounding environment. Coupling all of these aspects across length-scales and time-scales into a holistic view of material performance in the fresh (fluid) state, during setting and hardening, and then in the context of durability, is essential to provide full confidence in material performance over a designed service life that may range from a few decades (for civil infrastructure), up to the million-year timescale on which a deep geological repository must serve to protect the environment.

Advanced characterisation techniques, including beamline-based tomography (Fig. 4.10a) and various spectroscopic techniques, can be (and must be) coupled with rheological/mechanical measurements, determination of heat flow (Fig. 4.10b), electrochemical methods to determine redox and corrosion behaviour, and thermodynamic and kinetic modelling approaches, to enable the best possible materials selection, specification and design for safety-critical applications within and beyond the nuclear sector. The expertise and facilities available within LES provide new and exciting opportunities to advance the state of the art in both fundamental science and key applications of all types of cementitious materials.

(a)

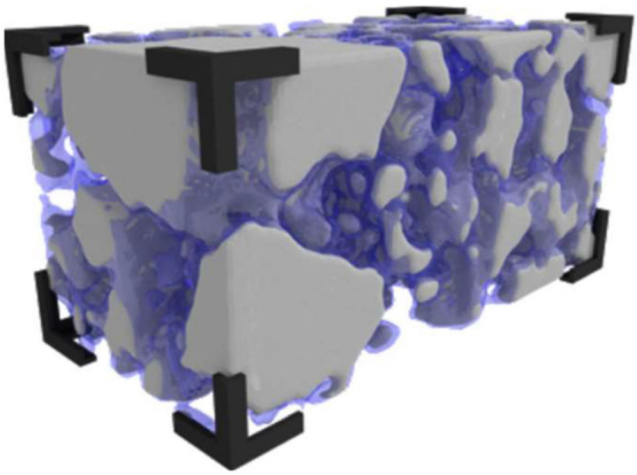

(b)

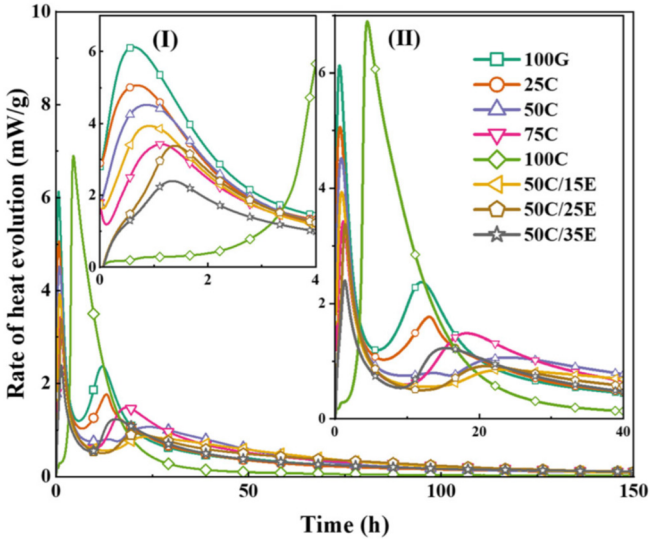

Fig. 4.10: (a) Reconstruction of the microstructure of a hydrating Portland cement, 13h45m after mixing, from synchrotron X-ray microtomography data. Region depicted is 250×250×500 mm. From Vigor et al. (2022), reproduced under a Creative Commons CC-BY licence. (b) Isothermal calorimetric traces describing the early stages of reaction of alkali-activated blends of blast furnace slag (G), copper slag (C), and electric arc furnace slag (E), showing the ability to manipulate the time and extent of heat release through blending of powder precursors in alternative cements. From Stefanini et al. (2023), reproduced under a Creative Commons CC-BY licence.

4.7 References

Bradbury M.H., Sarott F.A. (1994)
Sorption Databases for the Cementitious Near-Field of a L/ILW Repository for Performance Assessment. PSI Bericht Nr. 95-06.

Bradbury M.H., Van Loon L.R. (1997)
Cementitious Near-Field Sorption Data Bases for Performance Assessment of a L/ILW Repository in a Palfris Marl Host Rock - CEM-94: Update I. Nagra Technischer Bericht, NTB 96-04.

Cvetković B.Z., Rothardt J., Büttler A., Kunz D., Schlotterbeck G., Wieland E. (2018)
Formation of low-molecular-weight organic compounds during anoxic corrosion of zero-valent iron. Environmental Engineering Science 35(5), 447-461.

Dilnesa B.Z., Lothenbach B., Le Saout G., Renaudin G., Mesbah A., Filinchuk Y., Wichser A., Wieland E. (2014)
Synthesis and characterization of hydrogarnet $Ca_3(Al_xFe_{1-x})_2(SiO_4)_y(OH)_{4(3-y)}$. Cement and Concrete Research 59, 96-111.

Gardner L.J., Corkhill C.L., Walling S.A., Vigor J.E., Murray C.A., Tang C.C., Provis J.L., Hyatt N.C. (2021)
Early age hydration and application of blended magnesium potassium phosphate cements for reduced corrosion of reactive metals. Cement and Concrete Research 143, 106375.

Guillemot T., Cvetkovic B.Z., Kunz D., Wieland E. (2020)
Processes leading to reduced and oxidised carbon compounds during corrosion of zero-valent iron in alkaline anoxic conditions. Chemosphere 250, 126230.

Guillemot T., Kunz D., Salazar G., Rauber M., Szidat S., Tits J., Wieland E. (2021)
Long-term monitoring of dissolved and gaseous ^{14}C-bearing carbon compounds during alkaline anoxic corrosion of irradiated steel. Nagra Arbeitsbericht, NAB 21-26.

Guillemot T., Salazar G., Rauber M., Kunz D., Szidat S., Wieland E. (2022)
Carbon-14 release and speciation during corrosion of irradiated steel under radioactive waste disposal conditions. Science of the Total Environment 817, 152596.

Heberling F., Metz V., Böttle M., Curti E., Geckeis H. (2018)
Barite recrystallization in the presence of ^{226}Ra and ^{133}Ba. Geochim. Cosmochim. Acta 232, 124-139.

Kearney S.A., Yorkshire A.S., Geddes D.A., Hanein T., Nelson S., Provis J.L., Walkley B. (2022)
Cement-based stabilization/solidification of radioactive waste. *In* Tsang D.C.W., & Wang L. *eds.* Low Carbon Stabilization and Solidification of Hazardous Wastes. Amsterdam: Elsevier, 407-431.

Lothenbach B., Kulik D., Matschei T., Balonis M., Baquerizo L.G., Dilnesa B.Z., Miron D., Myers R. (2019)
Cemdata 18: A chemical thermodynamic database for hydrated Portland cements and alkali-activated materials. Cement and Concrete Research 115, 472-506.

Luraschi P., Gimmi T., Van Loon L.R., Shafizadeh A., Churakov S.V. (2020)
Evolution of HTO and $^{36}Cl^-$ diffusion through a reacting cement-clay interface (OPC paste-Na montmorillonite) over a time of six years. Applied Geochemistry 119, 104581.

McWilliams J., Walkley B., Provis J.L. (2023)
Developing Pickering emulsion routes towards oil immobilisation in geopolymers. *In* Thailand Concrete Association *ed.* 16th International Congress on the Chemistry of Cement: Further Reduction of CO_2-Emissions and Circularity in the Cement and Concrete Industry. Bangkok, Thailand: TCA, 497-500.

Nagra (2019)
Selection of dose-relevant radionuclides (dRN) for the reference scenario for post-closure safety in SGT-Stage 3. Nagra Aktennotiz, AN 16-559 Rev.3.

Nedyalkova L., Lothenbach B., Geng G., Mäder U., Tits J. (2020)
Uptake of iodide by calcium aluminate phases (AFm phases). Applied Geochemistry 116, 104559.

Nedyalkova L., Tits J., Bernard E., Wieland E., Mäder U. (2021)
Sorption Experiments with HTO, 36-Cl, 125-I and 14-C Labeled Formate on Aged Cement Matrices Retrieved from Long-term In-situ Rock Laboratory Experiments. Journal of Advanced Concrete Technology 19, 811-829.

Nedyalkova L., Tits J., Renaudin G., Wieland E., Mäder U. (2022)
Mechanisms and thermodynamic modelling of iodide sorption on AFm phases. Journal of Colloid and Interface Science 608, 683-691.

Nelson S., Geddes D.A., Kearney S.A., Cockburn S., Hayes M., Angus M.J., Cann G., Provis J.L. (2023)
Hydrate assemblage stability of calcium sulfoaluminate-belite cements with varying sulfate content. Construction and Building Materials 383, 131358.

Niu X., Elakneswaran Y., Islam C.R., Provis J.L., Sato T. (2022)
Adsorption behaviour of simulant radionuclide cations and anions in metakaolin-based geopolymer. Journal of Hazardous Materials 429, 128373.

Shafizadeh A., Gimmi T., Van Loon L.R., Kaestner A.P., Mäder U.K., Churakov S.V. (2020)
Time-resolved porosity changes at cement-clay interfaces derived from neutron imaging. Cement and Concrete Research 127, 105924.

Shi C., Qu B., Provis J.L. (2019)
Recent progress in low-carbon binders. Cement and Concrete Research 122, 227-250.

Stefanini L., Ghorbani S., De Schutter G., Matthys S., Walkley B., Provis J.L. (2023)
Evaluation of copper slag and stainless steel slag as replacements for blast furnace slag in binary and ternary alkali-activated cements. Journal of Materials Science 58(31), 12537-12558.

Tits J., Kunz D., Salazar G., Rauber M., Szidat S., Wieland E., Guillemot T. (2023)
1th annual report of the IGD-TP Project: "LOng-term Monitoring of C-14 compounds released during corrosion of IRradiated steel" (LOMIR). IGD-TP Report 2022/Report/1, Nagra, Wettingen, Switzerland (available on request).

Tits J., Wieland E. (2023)
Radionuclide retention in the cementitious near field of a repository for L/ILW: Development of the cement sorption data base for use in the license application. Nagra Technischer Bericht, NTB 23-07.

Vigor J.E., Bernal S.A., Xiao X., Provis J.L. (2022)
Time-resolved 3D characterisation of early-age microstructural development of Portland cement. Journal of Materials Science 57(8), 4952-4969.

Wieland E. (2014)
Sorption data base for the cementitious near field of L/ILW and ILW repositories for provisional safety analysis for SGT-E2. Nagra Technischer Bericht, NTB 14-08.

Wieland E., Van Loon L.R. (2002)
Cementitious near-field sorption database for performance assessment of an ILW repository in Opalinus Clay. PSI Bericht Nr. 03-06 and Nagra Technischer Bericht, NTB 02-20.

5 THERMODYNAMIC MODELS AND DATABASES

Miron G.D., Kulik D.A., Marinich O., Glaus M.A., Marques Fernandes M.

5.1 Introduction

The database projects support the development of the geochemical models for pore waters, radionuclide solubility, sorption, and transport calculations used in the geochemical safety assessments for the general license applications of the low- and intermediate-level (L/ILW) and high-level (HLW) radioactive waste planned repositories in Switzerland. The PSI chemical thermodynamic database TDB 2020 (Hummel & Thoenen, 2023) contains the thermodynamic properties of relevant substances necessary for geochemical modelling of in situ conditions in the repository near field, and radionuclide transport in geological and engineered barriers. The database is used in defining the chemical systems for calculating solubility limits, sorption, diffusion, pore water models and host rock mineralogy (Fig. 5.1). Parameterisation and calculations for the sorption (section 5.2) and diffusion models (section 5.3) and the corresponding databases are conducted in consistency with the PSI TDB 2020 using the GEMS software collection. The results of these calculations are then used by Nagra in repository performance case evaluations.

5.2 ClaySor (2SPNE SC/CE) model: updated thermodynamic sorption database

To assess the safety of a deep geological radioactive waste repository in clay rich rocks, solid-liquid distribution coefficients (Kd values) for various radionuclides, rock composition and pore water chemistry are needed. Over the past two decades, PSI has developed mechanistic sorption models for many relevant radionuclides using experimental in-house data (Baeyens & Bradbury, 2017; Bradbury & Baeyens, 2017). This includes a generalised Cs adsorption model for Cs(I) on argillaceous rocks, and the 2SPNE SC/CE model for various key radionuclides (STDB 2017) (Baeyens & Bradbury, 2017; Bradbury & Baeyens, 2017; Baeyens and Marques, 2018). In 2017, the 2SPNE SC/CE model was reimplemented in GEMS as the ClaySor model (Kulik et al., 2018). However, the previous ClaySor model did not account for parameter uncertainty estimates, and the standard thermodynamic properties of sorption species needed to be made consistent with the new chemical thermodynamic database TDB 2020 release (Hummel & Thoenen, 2023). Hence, the ClaySor model and database (TD-SDB) were updated to ensure consistency with the revised thermodynamic data for aqueous species and solids in TDB 2020.

The re-parameterisation of the ClaySor model was performed using the GEMSFITS parameter optimisation tool (Miron et al., 2015) that also provides parameter confidence intervals. In-house (published) experimental datasets, including sorption as a function of pH (pH edges) and at different metal concentration (sorption isotherms) in various single electrolyte solutions, were used for deriving an updated thermodynamic sorption database STDB 2023 (Fig. 5.2). These datasets were converted into a standardised format for GEMSFITS and were used to refit the standard equilibrium constants of sorption species, including deriving 95% parameter confidence intervals. These are essential for evaluating the model uncertainty in predicting element uptake in repository safety assessments based on specific porewater and clay rock mineralogy.

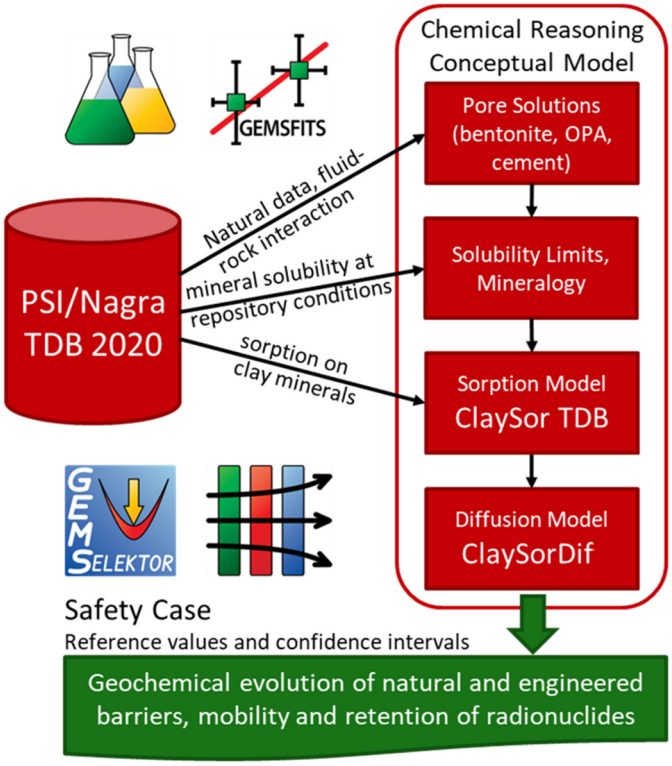

Fig. 5.1: Schematic relations between the PSI/Nagra thermodynamic database, models, and derived databases used in calculating reference values and confidence intervals for sorption, diffusion and geochemical repository evolution.

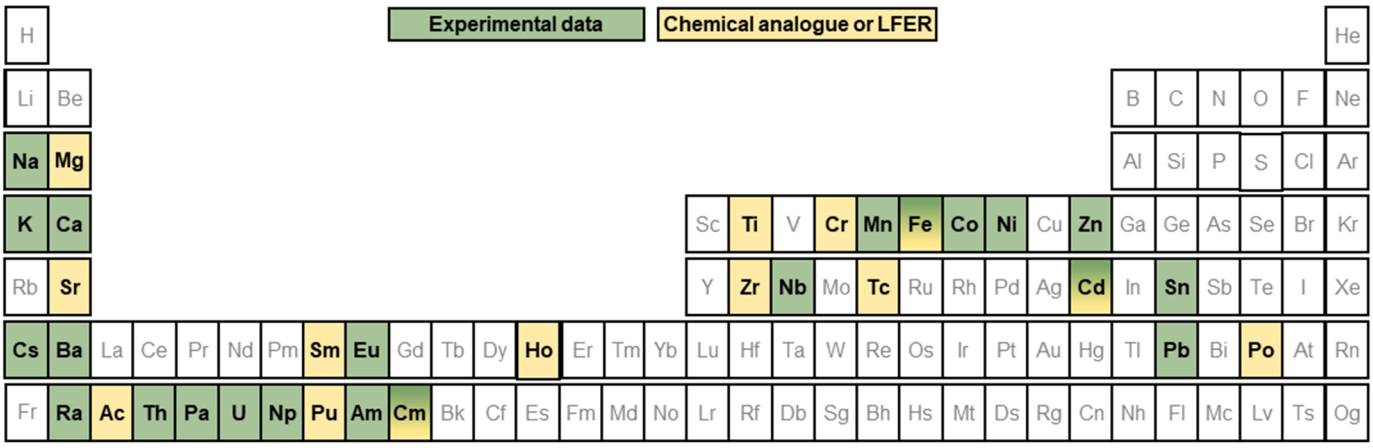

Fig. 5.2: Chemical elements considered in the PSI thermodynamic sorption database STDB 2017/ and 2023 update for illite and montmorillonite.

For some elements like thorium, changes in aqueous speciation have been proposed in the TDB 2020 aqueous database as compared with the data used for TD-SDB 2017. The third hydrolysed species $Th(OH)_3^+$ is not included in the aqueous database, see details in Hummel & Thoenen (2023). Consequently, the experimental Th(IV) sorption data were refitted without considering this species (Fig. 5.3 a, b). Strongly hydrolysed elements such as Th show almost constant sorption at different pH values. For other elements such as U(VI), no significant changes in the hydrolysis speciation exist. Changes to the model were implemented to optimise the fit and the number of surface complexation constants (Fig. 5.3 c, d). The uranyl ion still dominates at low pH and the increase in sorption can be observed from low to neutral pH values. The model 95% confidence band is calculated with the uncertainty propagation and sensitivity analysis for GEMS (UpSaGEMS) tool using the 95% confidence intervals distribution of the sorption species equilibrium constants.

For the Swiss geological repository performance assessment, a state-of-the-art sorption database (SDB) is needed for the different siting regions under investigation. This database contains solid-liquid distribution coefficients (Kd values) for various radionuclides under the conditions of the compacted clay host rocks and model porewater compositions typical for these regions. These are calculated using the "bottom-up" approach, based on complex aqueous speciation and single-mineral sorption processes, particularly focusing on 2:1 clay minerals such as illite, smectite, and illite-smectite mixed layers. The total sorption site capacities are then scaled to the 2:1 clay mineral content in the rock, and the radionuclide speciation in porewater is considered for calculating the sorption isotherms. The site-specific sorption distribution ratios (R_d) with 95% confidence intervals are calculated using the measured and modelled clay pore water, the determined clay percentage, and the ClaySor STDB model species equilibrium constants. For the sorption database for different trivalent and tetravalent elements, Am(III) or Eu(III) and Th(IV) were used as analogues (e.g. the same R_d values assumed), due to the lack of conclusive experimental data. Competition was taken into account between Fe, Mn, Cd, Co, Pb, and Zn divalent ions (Marques Fernandes and Baeyens, 2020). Elements that are predicted to be in zerovalent state (e.g., $Pd(0)_{aq}$) or having a dominant anionic speciation (e.g., complexes with Cl^-, HS^-) in the porewater were assumed to be non-sorbing. The sorption distribution coefficients for bentonite near field and Opalinus clay (Fig. 5.4) show a decreasing trend from higher to lower valence elements. Uranium stands out as it is predicted to be sorbed in the tetravalent oxidation state, but to be hexavalent in solution due to the very strong formation of calcium uranyl carbonate aqueous species. A larger scatter for the di- and monovalent elements is observed for illite due to sorption of certain elements on high-affinity sites (e.g. Cs sorption on frayed-edge and type-II sites (Brouwer et al., 1983)).

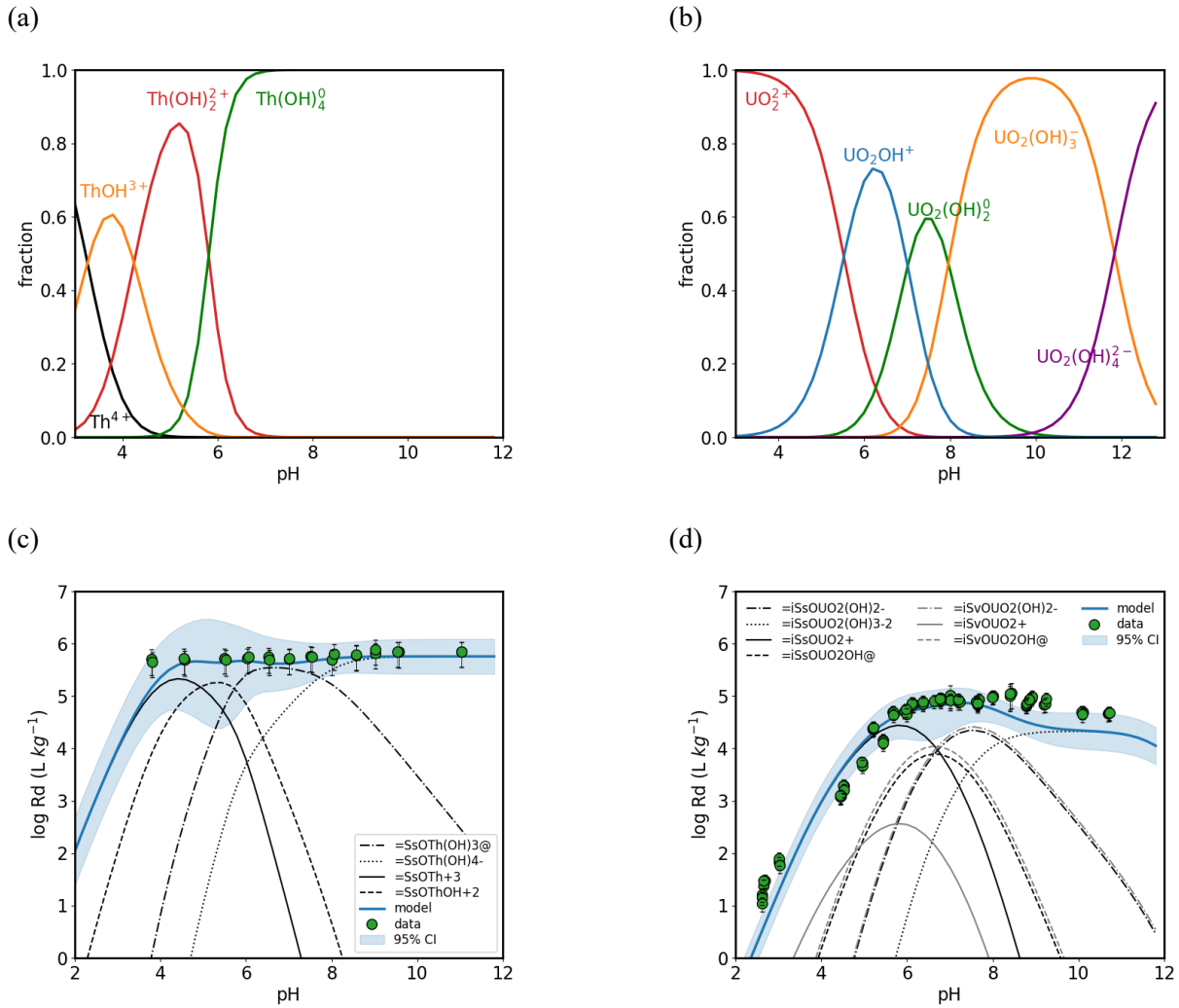

Fig. 5.3: (a, b) Aqueous speciation calculated based on TDB 2020: for (a) Th(IV) and (b) U(VI); (c, d) measured (symbols) (Baeyens & Bradbury, 2017; Bradbury & Baeyens, 2009) and calculated sorption R_d for pH edges in 0.1 M $NaClO_4$ with 95% model confidence band: (c) Th(IV) on montmorillonite and (d) U(VI) on illite. =Ss, -iSs, iSv stand for strong site montmorillonite, strong site illite and weak site illite, respectively.

5.3 The ClaySorDif model for effective diffusion coefficients in argillaceous media

Diffusion is the main transport mechanism for radionuclides in a deep geological repository with dense clay-rich natural and engineered barriers. Hence, using appropriate transport models and robust parameter values for diffusion is necessary for a reliable assessment of repository performance. The argillaceous rock and bentonite barriers contain ubiquitous clay minerals such as illite and montmorillonite, bearing a negative permanent charge due to isomorphic substitutions in the crystal lattice of their platelets or grains. Thus, diffusion of trace radionuclide species in porewater may be strongly influenced by this charge: anions are repelled from the planar clay surfaces ("anion exclusion") and diffuse at lower rates compared to uncharged tracers; cations are attracted by such surfaces ("cation condensation") and may diffuse at enhanced rates. These effects are captured in effective diffusion coefficients D_e that depend on various chemical characteristics of the clay surface and the porewater. Chemical models were implemented in various codes to derive such values based on the equilibrium distribution of charged species between the 'free' aqueous bulk solutions and pore water volumes near planar surfaces (Appelo & Wersin, 2007; Appelo et al., 2010; Parkhurst & Appelo, 2013; Glaus et al., 2015; Gimmi & Alt-Epping, 2018; Glaus et al., 2024a). A representative example for such a situation is shown in Fig. 5.5 for the mean-potential in Donnan layer model (MPDL).

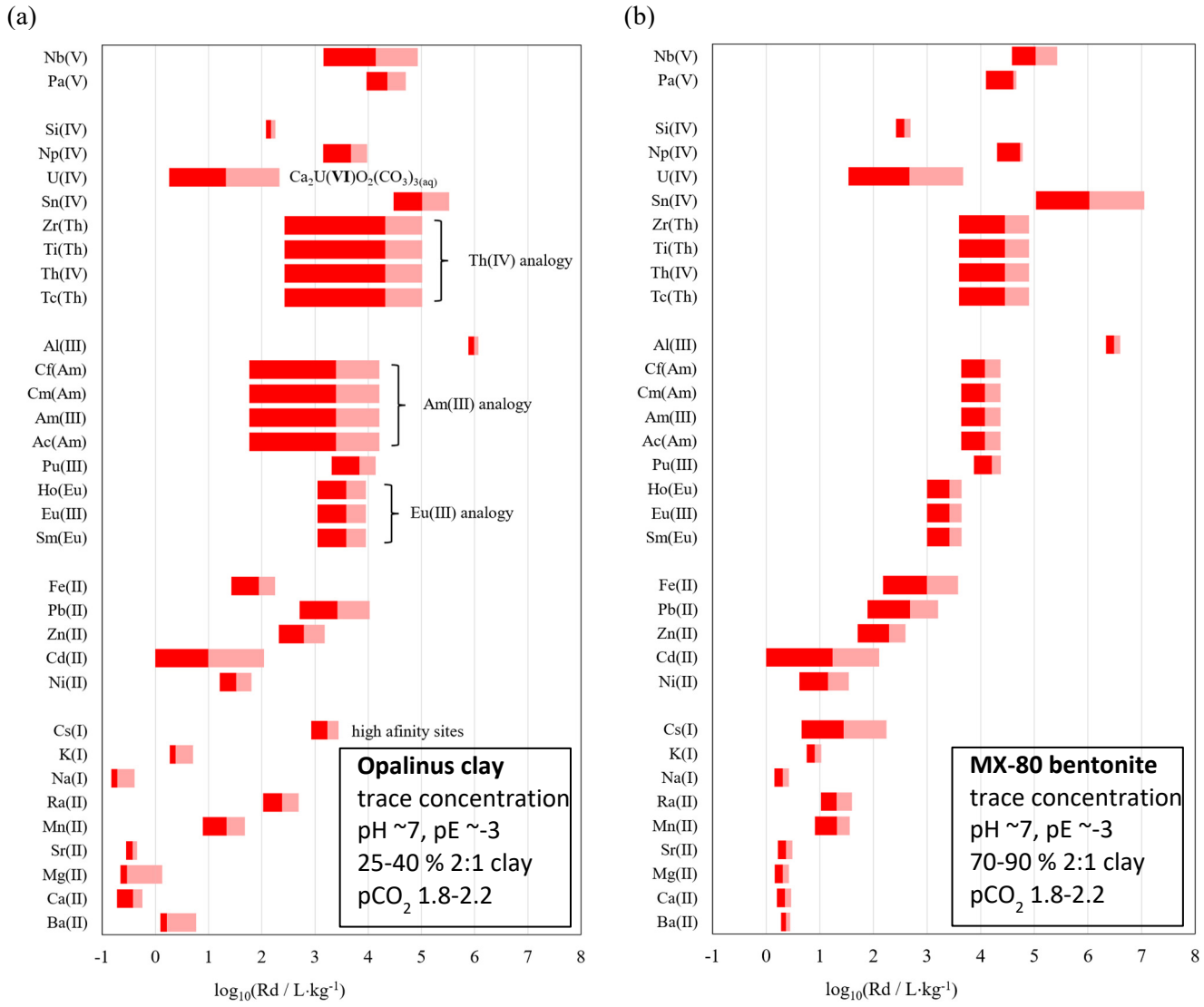

Fig. 5.4: (a) Sorption expressed as log R_d in Opalinus clay and in MX-80 bentonite, shown as bars ranging between lower and upper values determined by the variation in clay %, pore water composition and model uncertainty, with interface between light and dark red as the reference R_d.

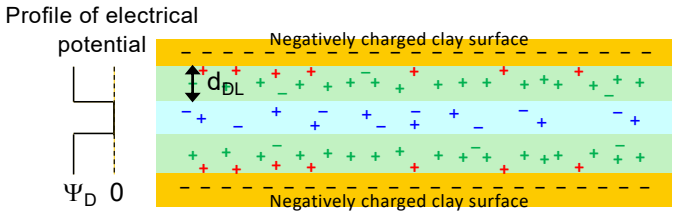

Fig. 5.5: Schematic diagram of a clay planar pore considered in the MPDL model (Glaus et al., 2024a).

In order to maintain the consistency of our toolchain based on GEMS (GEM software collection), we have implemented the MPDL model as the core of the ClaySorDif model code to provide the GEMS user community with extensions relevant for waste disposal in clay rock and bentonite (Kulik et al., 2023). The advantage of ClaySorDif is that it involves the ClaySor sorption model and database (see 5.2) as such, and does not require modification of the ion exchange model on illite or montmorillonite by adding "free charge" X-species and augmenting the binding constants for exchange cations as is done elsewhere (Appelo et al., 2010; Glaus et al., 2015, 2023b; Gimmi & Alt-Epping, 2018). Instead, the ClaySorDif implementation of MPDL is controlled by a new FCC (free charge capacity) adjustable parameter, separated from the measurable CEC (cation exchange capacity) = CBC (cation binding capacity) used in ClaySor and other sorption models to describe ion exchange on clays.

In simple diffusion models, the effective diffusion coefficient $D_{e,elem}$ for the total dissolved chemical element is used. From 'free' and Donnan layer porewater speciation, it is evaluated as a weighted average:

$$D_{e,elem} = D_{e,n}\chi_n + \frac{\varepsilon}{G}\sum D_{w,i}\left(f_{free}\chi_{i,free} + f_{DL}\frac{c_{i,DL}}{c_{i,free}}\chi_{i,DL}\right) \quad (5.1)$$

where ε is the porosity and G is the geometry factor, both treated as empirical functions of the clay content in the argillaceous rock or bentonite; χ_n, $\chi_{i,free}$, $\chi_{i,DL}$ are molar aqueous speciation fractions of all neutral species, ionic species i in 'free' and Donnan layer (DL) porewater of volume fractions f_{free} (dependent on ε) and f_{DL} (depends on ionic strength in model porewater), respectively; $D_{e,n}$ is the effective diffusion coefficient of all neutral species, assumed to be the same as $D_{e,HTO}$; $D_{w,i}$ is the bulk diffusion coefficient of ionic species i in water at the temperature and pressure of interest (taken from the DwDB database). $\frac{c_{i,DL}}{c_{i,free}}$ is the ratio of the molar concentration of species i in DL (affected by the clay permanent charge) and in the 'free' pore water, obtained from iterative MPDL charge-balance calculations based on the model porewater equilibrium composition.

Depending on the prevailing species (neutral, anionic or cationic), the overall pattern of diffusion rates for a given element may be neutral ($D_e = \frac{\varepsilon}{G}D_w$) similar to HTO tracer; anionic ($D_e < \frac{\varepsilon}{G}D_w$) meaning partial anion exclusion from porewater affected by clay charge; or cationic ($D_e > \frac{\varepsilon}{G}D_w$) meaning enhancement in porewater relative to 'free' porewater. Based on ClaySorDif calculations for OPA and bentonite model porewaters, the considered chemical elements can be grouped as shown in Table 5.1. Some trends in this table may seem counterintuitive. Due to strong hydrolysis or complexation with Ca or carbonate ions abundant in clayrock porewaters, some elements commonly expected to behave like cations (e.g. Nb, Np, Th, U; Cu), display anionic diffusion trends and should diffuse slower than water. Other cationic or anionic elements exist mainly as neutral aqueous species (e.g. Ag, Pd, Po, Se, Sn, Tc, Hg) and must diffuse in clayrock as fast as neutral tracers or water.

In addition to D_e values, predictions from the ClaySorDif model include the dimensionless rock capacity factor α. For anionic species ($z_i < 0$)

$$\alpha_i = \varepsilon_{AN,i} = (f_{free} + f_{DL}\frac{c_{i,DL}}{c_{i,free}})\varepsilon \quad (5.2)$$

$\varepsilon_{AN,i}$ is called the "anion-accessible porosity"; in the absence of clay charge, ε_{AN} is close to ε; at low porosity, high clay charge and relatively low ionic strength, f_{DL} reaches 0.99 and concentration ratio (especially for a divalent anion) can be much less than 0.1, meaning almost complete anion exclusion. For neutral non-sorbing tracers, $\alpha = \varepsilon$. For cationic elements, another form of the rock capacity factor is calculated:

$$\alpha = \varepsilon + R_d\rho_{br} \quad (5.3)$$

Here, R_d is the bulk distribution ratio (L·kg^{-1}). It is assumed that the [cationic] element is only sorbed on the clay mineral, in which case R_d is computed from the equilibrium between illite edges and planar sites and 'free' porewater using the ClaySor model (see Section 5.2 above), and then scaled down to the mass of clayrock by dividing by the mass fraction of illite or montmorillonite. For elements mainly sorbed by ion exchange on planar permanent-charge sites (Na, K, Sr, Ba, …), ClaySor includes the site-binding model normalised per mass of clay mineral and CBC, and delivers the same type of R_d, which is perhaps a good model for illite. However, for montmorillonite (in bentonite), alternative models have been suggested in the literature that represent cation exchange not as site binding (controlled by CBC parameter such as in ClaySor model) but rather as cation excess concentration in the Donnan layer relative to that in 'free' porewater. This kind of representation is possible in ClaySorDif as an alternative to the site-binding ion exchange in ClaySor model, but assessment of its applicability requires more future research.

Tab. 5.1: D_e trends of chemical elements due to speciation clayrock porewater (Glaus et al, 2023).

Speciation pattern	Radionuclides and fission products	Chemotoxic elements	Diffusion trend
Cationic	Am, Cm, Cs, Hg, Ho, Ni, Pb, Pu, Ra, Sm	Cd, Zn, Eu, Co	$D_{e,elem} > D_{e,HTO}$
Neutral	Ag, Pa, Pd, Po, Se, Sn, Tc, Ti, Zr	Hg	$D_{e,elem} \approx D_{e,HTO}$
Anionic	C, Cl, I, Mo, Nb, Np, Th, U, Br, F, S	Cu	$D_{e,elem} < D_{e,HTO}$

The ClaySorDif extension for modelling clayrock-porewater systems has been implemented as a Python class ClaySorDif.py which uses the Python interface xGEMS of GEMS3K code from the GEMS collection (Kulik et al., 2013; https://gems.web.psi.ch). It was calibrated and benchmarked by comparing with Phreeqc modelling of D_e, α and R_d curves derived from modelling of the experimental diffusion data for clayrocks from Nagra drilling campaigns (Glaus et al., 2015; 2024a).

Phreeqc modelling was applied recently to experimental diffusion data for TBO samples from the last Nagra drilling campaign, belonging to four locations (Glaus et al., 2024a). Diffusion measurements were conducted in four synthetic porewaters with compositions mimicking the porewater data for the respective locations (Van Loon et al., 2023). These porewater compositions were checked in Phreeqc and trial GEMS calculations against measured pH, Eh and equilibria with calcite, dolomite (and gypsum depending on location). Illite edge sites were excluded from calculations at this stage. For the benchmarking, the same synthetic porewater systems were implemented in both codes and calculations of porewater equilibria checked using the same thermodynamic database (PSI TDB 2020) and input porewater compositions at 1 bar and 25 °C. Phreeqc results for a range of clay contents from 1% to 99% were collected into CSV files (as well as ClaySorDif results). A Python Jupyter notebook was written to read these CSV files along with the experimental data (also provided in CSV files), and to plot them together using matplotlib with export into PNG or PDF graphical files.

MPDL models in Phreeqc and in ClaySorDif differ in the implementation of ion exchange and treatment of clay charge acting onto the Donnan layer. The former uses the 'free' planar site charge species X^- as part of the balance defined by CEC to provide the DL charge, the density of which can be set by adjusting the cation binding reaction constants (see Tab. 2.3.2). The latter uses the site-binding cation exchange model from ClaySor model with the cation binding capacity CBC equal to CEC as given in ClaySor; the illite permanent charge density acting onto the Donnan layer is defined by an adjustable parameter FCC for illite, treated independently of CBC or CEC.

Keeping in mind the differences between models, before any benchmarking or verification, a calibration has been performed using the experimental data and Phreeqc results for $D_{e,HTO}$, $D_{e,Cl}$, $D_{e,Na}$ for each of four locations (BUL, TRU, STA, BOZ) (Van Loon et al., 2023). The calibration consisted in trial calculations of ClaySorDif curves for these properties while adjusting the FCC parameter in the range $0.1 < FCC < 0.225$ eq·kg^{-1} until a perfect match with the Phreeqc curve is achieved. This process for each dataset has led to FCC = 0.17 ± 0.01 eq·kg^{-1}, i.e. practically the same for all locations. Hence, in all subsequent calculations, the calibrated value FCC = 0.17 eq·kg^{-1} for OPA illite is used. This value is reasonable, making 76% of the CEC = 0.225 eq·kg^{-1} used in ClaySor model as the CBC for illite ion exchange. Similar calibration procedures for MX-80 and Volclay bentonites have led to FCC = 1.05 eq·kg^{-1} of montmorillonite, only slightly less than the measured CEC = 1.056 to 1.16 eq·kg^{-1} (ClaySor model for montmorillonite uses CBC = CEC = 0.87 eq·kg^{-1}).

At the verification stage, comparison of ClaySorDif and Phreeqc profiles demonstrates that starting from $D_{e,HTO}$, the match is (almost) perfect in all cases, also showing a good description of experimental data. ClaySorDif provides the same quality of fit for experimental α_{Cl-} (anion-accessible porosity) values as the Phreeqc model, but yields a significantly better fit (without any additional adjustment) for the experimental α_{Na+} rock capacity factor values than that provided by the Phreeqc model (not shown). This may be due to a better calibration of the ClaySor model for ion exchange than the augmented (with the 'free charge' X^- species) ion exchange model implemented in Phreeqc.

The ClaySorDif model provides full equilibrium speciation in both 'free' porewater (i.e. model porewater) and Donnan layer porewater at given clay content. Along with the DwDB database of bulk diffusion coefficients for ca. 60 elements (compiled as part of the ClaySorDif development), this leads to possibilities to plot and analyse the impact of aqueous speciation onto profiles of D_e for chemical elements in clayrock as function of clay content. In Fig. 5.6, the total-element D_e curves show a perfect match between Phreeqc and ClaySorDif modelling for all three elements (S, Na, Sr), with details for predominant species of those elements. The counter-intuitive result for S that the $D_{e,S}$ curve is similar to curves for monovalent anions despite sulfate SO_4^{2-} being a divalent anion is due to the speciation in clayrock porewaters: a large fraction of sulfate is bound in neutral ($CaSO_4$, $MgSO_4$) and anionic ($NaSO_4^-$) complexes of major cations, so the 'free' SO_4^{2-} ion is only minor. For Sr, the bicarbonate $SrHCO_3^+$ complex makes 10-15% and neutral $SrSO_4$ complex about 10% of the total Sr, so the $D_{e,Sr}$ values are between those for di- and monovalent cations.

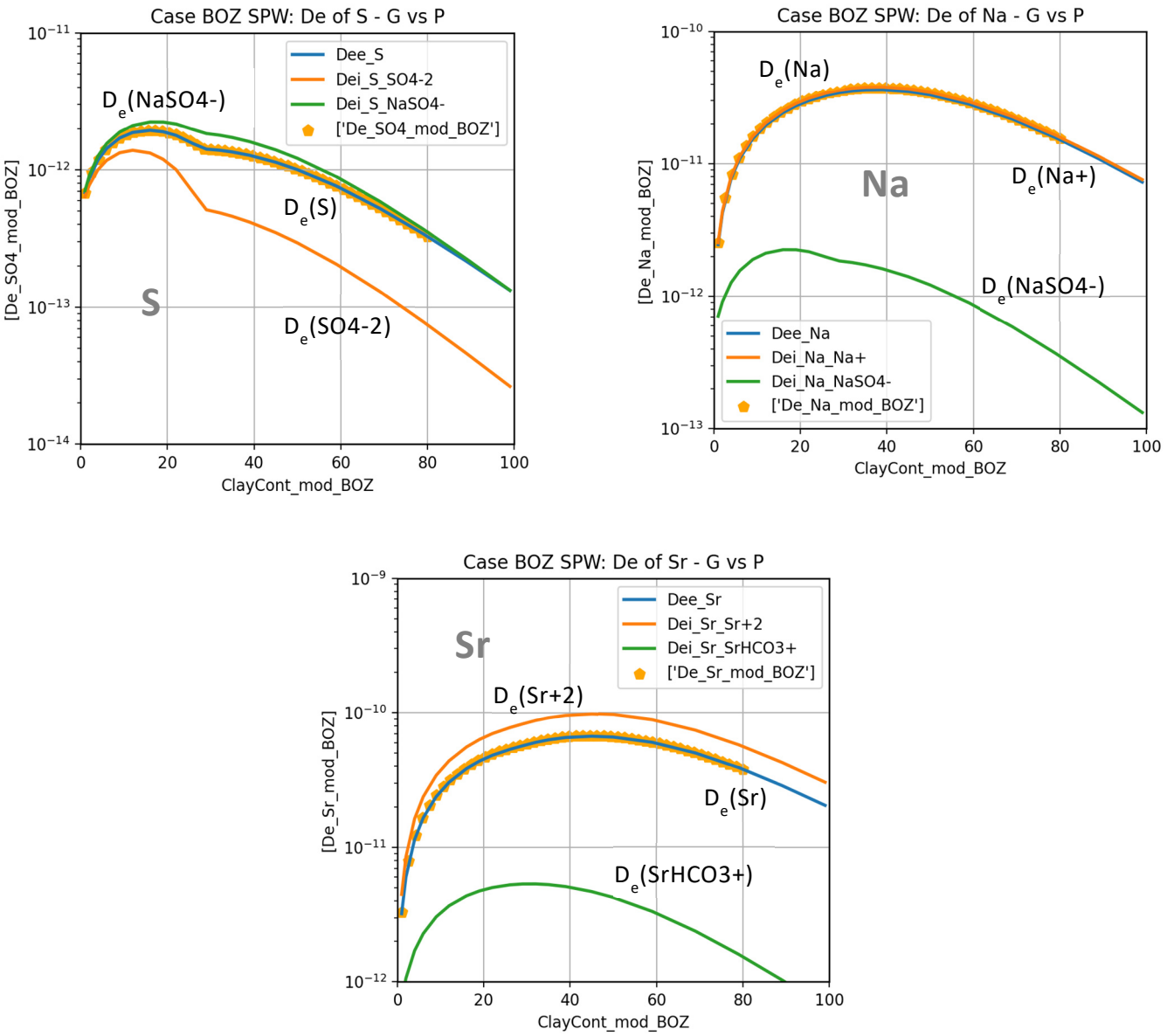

Fig. 5.6: ClaySorDif vs Phreeqc: impact of aqueous speciation on D_e of S, Na, Sr. Location: BOZ (Bözberg). Orange hexagons: Phreeqc results (Glaus et al., 2024a); solid curves: ClaySorDif results (Glaus et al, 2024b).

5.4 Modelling saline systems with Thereda and GEM-Selektor

Thereda (Moog et al., 2015) is an internally consistent thermodynamic database that focuses on the solubility of radionuclides and other radioactive waste disposal relevant processes in highly saline systems. Most of the core data of standard state thermodynamic properties for elements and species related to low soluble solids are consistent with the PSI Nagra TDB (Hummel et al., 2002; Thoenen et al., 2014).

For modelling high salinity aqueous solutions, the database supports the Pitzer ion-interaction model and provides a polythermal set of model parameters for a selection of elements (https://www.thereda.de). The Pitzer activity model (Pitzer, 1973) is a set of equations that calculates the activity coefficients of solutes as a function of composition by accounting for different interactions between aqueous species. Only binary and ternary interactions are considered, with binary interactions between species of different charge being mostly relevant in low to intermediate concentrations. Qualitatively, the Specific Interactions Theory (SIT) model, used in the PSI Nagra TDB 2020 (Hummel & Thoenen, 2023), can produce similar results to the Pitzer model when used in binary systems to model solubility in low to moderate concentrations of a single background electrolyte. The Pitzer model can accurately model data in multi-component highly concentrated salt solutions, yielding activity

coefficients and solubilities of multiple salts, but requires a large number of parameters. These interaction parameters can be derived from various experimental data obtained from isopiestic, aqueous complexation and solubility measurements.

The database has an extensive set of polythermal interaction parameters for the oceanic salts system revised and extended by Voigt et al. (2011), as well as datasets for several actinides and fission products. To extend its application for modelling interactions between cementitious materials and highly saline solutions the database needed to be extended with relevant properties for cement hydrates and missing interaction parameters for the Si and Al species. Data for cement hydrate phases is taken from the Cemdata18 database (Lothenbach et al., 2019) using the reported solubility constants and the aqueous species from Thereda. A set of polythermal interaction parameters for Si and Al aqueous species consistent with the oceanic salts system is derived from the available experimental data and estimation methods where no data are available. This work is funded by BGE (Federal Company for Waste Disposal, Germany).

The newly derived consistent parameter dataset will support the modelling of equilibrium solid- and pore-water composition in hydrated (blended) cement materials in a wide range of conditions up to highly saline systems relevant for cement-brine interactions, alkali activated materials, and concentrated pore solutions.

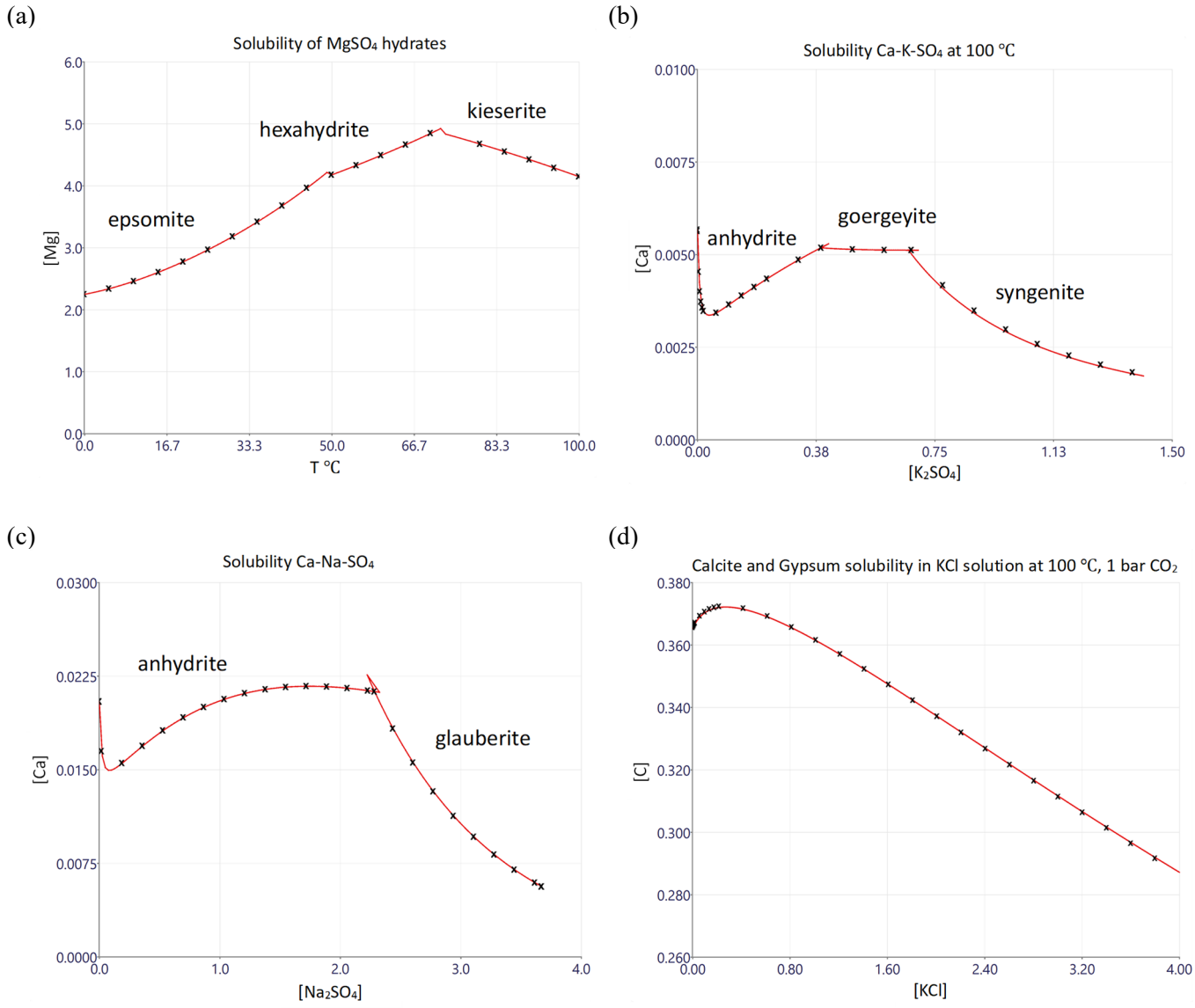

Fig. 5.7: Comparison between calculations using the Pitzer activity model and the Thereda database (release 2020) implemented in GEM-Selektor (curves) and in Phreeqc (symbols x) codes. Concentrations [] in mol/kg H_2O, temperature in °C.

The Pitzer activity model is accessible in GEM-Selektor as part of the TSolMod library of solution models (Wagner et al., 2012). To be used in calculations, the model needs to be accompanied by a dataset of parameters relevant for the systems on interest. For this, the Thereda database was converted from the JSON format that is available for download on https://www.thereda.de into the GEM-Selektor format using the ThermoMatch (https://thermohub.org/thermomatch) import scripts, making the Thereda database now also compatible with the GEMS codes and ready to be officially distributed for GEMS. This expands the field of applications and reachability of the GEMS codes and of the THEREDA database.

The Pitzer model implementation in GEM-Selektor v.3.9.6 (Kulik et al., 2013) was benchmarked against results from Phreeqc (interactive 3.7.3) (Parkhurst & Appelo, 2013) using the Thereda database (release 2020). After minor fixes and extensions (e.g., removing hardcoded parameters) and implementation of the Bradley & Pitzer (1979) water dielectric constant model, identical calculated values are now obtained with both codes (Fig. 5.7).

5.5 The SOREDA Sorption reference database

The SOREDA project aims to develop a sorption database of radionuclides, relevant for the safety case of a deep geological repository, on a range of minerals of argillaceous host rocks and buffer materials, such as clay minerals, quartz, carbonates and iron-bearing minerals (Tab. 5.2). An important weight will be put on the physicochemical feasibility of its constituent sorption models and the spectroscopically evident surface complexes.

Based on many years of experience in the study of radionuclide sorption processes on clay rich rocks, as well as in the development of mechanistic sorption models, PSI LES is responsible for the development of clay minerals part of the database within the project. Sorption modelling on quartz, carbonates and iron-bearing minerals is carried out by The Helmholtz-Zentrum Dresden-Rossendorf (HZDR). A fundamental part of the database development is the collection, critical evaluation, and digitalisation of radionuclides sorption data, namely pH edges and isotherms. A significant amount of the raw sorption data come from the experimental studies conducted over several decades at PSI, augmented with the raw data that is compiled into the Lawrence Livermore National Laboratory (LLNL) experimental dataset. For systems with no experimental data, gaps in the model will be filled out by use of chemical analogies. In certain cases, the use of linear free energy relationships will be considered to derive surface complexation constants (Bradbury and Baeyens, 2011). Since the surface complexation constants are directly related to the protolysis constants of minerals, their values will be fitted against reliable titration data.

Modelling of radionuclide sorption on clay minerals will be carried out using the sorption model and chemical thermodynamic database developed in LES: ClaySor as the GEMS implementation of the two site protolysis non electrostatic surface complexation cation exchange model (2SPNE SC/CE) (Bradbury & Baeyens, 2017) and the PSI2020 thermodynamic database (Hummel & Thoenen, 2023) in GEMS format (Kulik et al., 2013). Fitting to experimental data and the uncertainties estimation of surface complexation constants will be carried out using the GEMSFITS package (Miron et al., 2015). For quartz, carbonates, and iron-bearing minerals the DDL is consistently applied by HZDR. Currently the 2SPNE SC/CE is nonelectrostatic, i.e., the thermodynamic properties in the STDB 2023 have no electrostatic correction, and data for sorption of ligands other than hydroxide were not updated. The extension of the 2SPNE SC/CE model with electrostatic models such as DDL is also considered for clay minerals. Ternary carbonate as well as silicate surface complexes of lanthanides and actinides will be also examined in the SOREDA project. The project funded by BGE (Federal Company for Waste Disposal) will result in a reliable reference sorption database that can be applied for the safety analysis of radioactive waste disposal.

Tab. 5.2: Minerals phases and radionuclides considered for the SOREDA project.

Mineral phases	Calcite, Dolomite, Quartz, Kaolinite, Illite, Montmorillonite, Ferrihydrite, Goethite, Hematite, Magnetite, Pyrite
Radionuclides	U(IV/VI), Am(III), Cm(III), Pu(III/IV), Np(IV/V), Th(IV), Sn(IV), Tc(IV/VII), Ni(II), I(-I/0/V), Ra(II), Sr(II), Cs(I), Se(IV/VI)

5.6 References

Appelo C.A.J., Van Loon L.R., Wersin P. (2010)
Multicomponent diffusion of a suite of tracers (HTO, Cl, Br, I, Na, Sr, Cs) in a single sample of Opalinus Clay. Geochimica et Cosmochimica Acta 74, 1201–1219.

Appelo A., Wersin P. (2007)
Multicomponent diffusion modeling in clay systems with application to the diffusion of tritium, iodide, and sodium in Opalinus Clay. Environmental Science and Technology 41, 5002–5007.

Baeyens B., Bradbury M.H. (2017)
The development of a thermodynamic sorption data base for montmorillonite and the application to bentonite. Nagra Technischer Bericht, NTB 17-13.

Baeyens B., Marques Fernandes M. (2018)
Adsorption of heavy metals including radionuclides. Developments in Clay Science 9, 125–172.

Bradbury M.H., Baeyens B. (2011)
Predictive sorption modelling of Ni(II), Co(II), Eu(IIII), Th(IV) and U(VI) on MX-80 bentonite and Opalinus Clay: A "bottom-up" approach. Applied Clay Science 52, 27–33.

Bradbury M.H., Baeyens B. (2017)
The development of a thermodynamic sorption data base for illite and the application to argillaceous rocks. Nagra Technischer Bericht, NTB 17-14.

Bradley D.J., Pitzer K.S. (1979)
Thermodynamics of electrolytes. 12. Dielectric properties of water and Debye-Hückel parameters to 350 °C and 1 kbar. Journal of Physical Chemistry, 83(12), 1599–1603.

Gimmi T., Alt-Epping P. (2018)
Simulating Donnan equilibria based on the Nernst-Planck equation. Geochimica et Cosmochimica Acta 232, 1–13.

Glaus M.A., Aertsens M., Appelo C.A.J., Kupcik T., Maes N., Van Laer L., Van Loon L.R. (2015)
Cation diffusion in the electrical double layer enhances the mass transfer rates for Sr^{2+}, Co^{2+} and Zn^{2+} in compacted illite. Geochimica et Cosmochimica Acta 165, 376–388.

Glaus M.A., Kulik D.A., Miron G.D., Van Loon L.R., Wüst R. (2024b)
Diffusion databases for Opalinus Clay, confining units and bentonite for the use in RBG: Methods and concepts. Nagra Technischer Bericht, NTB 23-08 (in prog.).

Glaus M.A., Kulik D.A., Van Loon L.R., Wüst R.A.J. (2023)
Verification of new ClaySorDif model for sorption and diffusion in argillaceous media against Phreeqc results and experimental data. Abstract C2-2, Migration 2023 Conference, 25-29 September 2023, Nantes, France.

Glaus M.A., Van Loon L.R., Wüst R. (2024a)
Diffusion of HTO, $^{36}Cl^-$ and $^{22}Na^+$ in the Mesozoic rocks of northern Switzerland. II: Data interpretation in terms of an electrical double layer model. Applied Geochemistry, 162, 105842.

Hummel W., Berner U., Curti E., Pearson F.J., Thoenen T. (2002)
Nagra/PSI Chemical Thermodynamic Data Base 01/01. Radiochimica Acta, 90, 805–813.

Hummel W., Thoenen T. (2023)
The PSI Chemical Thermodynamic Database 2020. Nagra Technischer Bericht, NTB 21-03.

Kulik D.A., Fernandes M.M., Baeyens B. (2018)
The 2SPNE SC/CE sorption model in GEM-Selektor v.3.4 code package (ClaySor): Implementation, tests, and user guide. Nagra Arbeitsbericht, NAB 18-27.

Kulik D.A., Glaus M.A., Gimmi T., Van Loon L.R., Wüst R. (2023)
GEMS implementation of an integrated ClaySorDif model for radionuclide sorption and diffusion in argillaceous media. Abstract C2-2, Migration 2023 Conference, 25-29 September 2023, Nantes, France.

Kulik D.A., Wagner T., Dmytrieva S.V., Kosakowski G., Hingerl F.F., Chudnenko K.V., Berner U.R. (2013)
GEM-Selektor geochemical modeling package: Revised algorithm and GEMS3K numerical kernel for coupled simulation codes. Computational Geosciences, 17(1), 1–24.

Lothenbach B., Kulik D.A., Matschei T., Balonis M., Baquerizo L., Dilnesa B., Miron G.D., Myers R.J. (2019)
Cemdata18: A chemical thermodynamic database for hydrated Portland cements and alkali-activated materials. Cement and Concrete Research, 115, 472–506.

Marques Fernandes M., Baeyens B. (2020)
Competitive adsorption on illite and montmorillonite: Experimental and modelling investigations. Nagra Technischer Bericht, NTB 19-05.

Miron G.D., Kulik D.A., Dmytrieva S.V., Wagner T. (2015)
GEMSFITS: Code package for optimization of geochemical model parameters and inverse modeling. Applied Geochemistry, 55, 28–45.

Moog H.C., Bok F., Marquardt C.M., Brendler V. (2015)
Disposal of nuclear waste in host rock formations featuring high-saline solutions – Implementation of a thermodynamic reference database (THEREDA). Applied Geochemistry, 55, 72–84.

Parkhurst D.L., Appelo C.A.J. (2013)
Description of Input and Examples for PHREEQC Version 3 — A Computer Program for Speciation, Batch-Reaction, One-Dimensional Transport, and Inverse Geochemical Calculations. U.S. Geological Survey.

Pitzer K.S. (1973)
Thermodynamics of electrolytes. I. Theoretical basis and general equations. J. Phys. Chem., 77(2), 268–277.

Thoenen T., Hummel W., Berner U.R., Curti E. (2014)
The PSI / Nagra Chemical Thermodynamic Database 12 / 07, PSI Bericht Nr. 14-04, 417 pp., ISSN 1019-0643.

Van Loon L.R., Bunic P., Frick S., Glaus M.A., Wüst R.A.J. (2023)
Diffusion of HTO, $^{36}Cl^-$ and $^{22}Na^+$ in the Mesozoic rocks of northern Switzerland. I: Effective diffusion coefficients and capacity factors across the heterogeneous sediment sequence. Applied Geochemistry, 159, 105843.

Voigt W. (2011)
Chemistry of salts in aqueous solutions: Applications, experiments, and theory. Pure and Applied Chemistry, 83(5), 1015–1030.

Wagner T., Kulik D.A., Hingerl F.F., Dmytrieva S.V. (2012)
GEM-Selektor geochemical modeling package: TSolMod library and data interface for multicomponent phase models. Canadian Mineralogist, 50(5), 1173–1195.

6 LANDFILLS GEOCHEMISTRY AND METAL RECOVERY

Churakov S.V., Eggenberger U., Weibel G., Wolffers M., Ingold P. (PhD Student), Dörfler P. (MSc Student)

6.1 Introduction

The Competence Center for Secondary Raw Materials (German: Fachstelle Sekundärrohstoffe, FSSR) at the Institute of Geological Sciences (University of Bern) conducts applied research in the field of environmental geochemistry and secondary raw materials. The core competencies of the FSSR include the topics of recycling management and disposal quality of conventional non-radioactive waste. The sustainable implementation of recycling technologies is waste type specific, and requires detailed knowledge of the chemical and phase composition of the materials, their long-term leaching behaviour, and process couplings controlling material degradation. To close material cycles and conserve primary raw material reserves, new approaches and processes are needed to use secondary raw materials on a larger scale and in new areas.

In Switzerland, an annual quantity of approximately 800’000 t of bottom ash and 80’000 t of fly ash arise from Municipal Solid Waste Incineration (MSWI). These solid residues are deposited at landfills in Switzerland as they do not currently meet the quality criteria for recycling due to high metal contents. Under the latest Swiss Waste Ordinance (Swiss Confederation, 2016), the requirements for residues have been increased and metal recovery must be implemented by 2026 for e.g. MSWI fly ash, by acid leaching (e.g. FLUWA process (Bühler & Schlumberger 2010)). The recovery and recycling of these heavy metals represent a valuable contribution to the sustainable closure of material cycles, as the metals from primary raw material mining can be partially replaced. However, for metal recycling from MSWI residues, detailed knowledge of the formation and composition of the incineration residues (bottom ash, fly ash) is essential to maximise the metal recovery and responsible disposal of residues in landfills. The partial replacement of primary resources with secondary raw materials, for example in cement production, can also represent a major environmental benefit due to an improved CO_2 balance.

6.2 Comparison of different metal recovery technologies for waste incineration bottom ashes in Switzerland

In Switzerland, the recovery of non-ferrous (NF) metals from the bottom ash of municipal solid waste (MSW) prior to landfilling has been legally required for more than 10 years according to the state of the art technology. Today’s processing technologies and the resulting metal recovery have reached a high level of efficiency. The current threshold limit value of 1 wt% for non-ferrous metals in the grain size range 2-16 mm is, in some cases, fulfilled with significant margins. Various new technologies contribute to the development, so that today residual bottom ashes with comparatively low residual metal contents are produced. In the near future, decisions on the implementation of specific bottom ash processing technologies will be made in several waste incineration plants. To support the decision making process with operational performance data, a comparative study of the different processing technologies was carried out on behalf of the Swiss Federal Office for the Environment (FOEN). The comparison includes treatment technologies from dry and wet discharge with different process stages: conventional technologies such as crushing, grinding, eddy current separators and density separation tables, as well as electrodynamic processes for the liberation of metals from the bottom ash components.

To ensure representativeness and to represent standard operation conditions, large sample quantities and adapted sampling concepts were applied. Approximately 100 tonnes of non-ferrous fractions were recovered at each of the four plants, subsequently referred to as Q1 quality. The four plants use wet electrodynamic fragmentation (Plant A), conventional wet discharged processing (B and C), and dry processing (D). Sampling time ranged from 1 to 9 weeks, depending on the throughput of the plant. The fractions were then processed individually in a subsequent processing step in a metal refining plant,

each producing 18 concentrates, including different grain size classes of non-ferrous heavy and non-ferrous light, two mineral fractions and oversize fractions. The refined fractions are referred to as Q2 grade. The metal contents and yields of the NE-light and NE-heavy fractions < 8 mm and 8-20 mm were determined by metal melting on 10-20 kg composite samples in the laboratory, and the fractions >20 mm were sorted and recorded manually by trained personnel. The residual slags R1 from Q1 metal processing and the bottom ash adhesions during Q2 refining (R2S and R2E) were analysed for total contents by XRF analysis. The entire process and the resulting fractions for the mass balance are shown schematically in Fig. 6.1.

The results of mechanical Q2 refining show that there are large differences in the metal contents of the various separated Q1-NE fractions from the different technologies (Fig. 6.2). The non-ferrous metal recoveries vary between 42 and 81 wt%, with electrodynamic fragmentation and dry-processed fractions showing significantly higher non-ferrous metal contents in the Q1 fractions. The residual metal contents in the R1 residual bottom ashes all meet the limits, with Plant B having an extremely low residual metal content of 0.11 wt%.

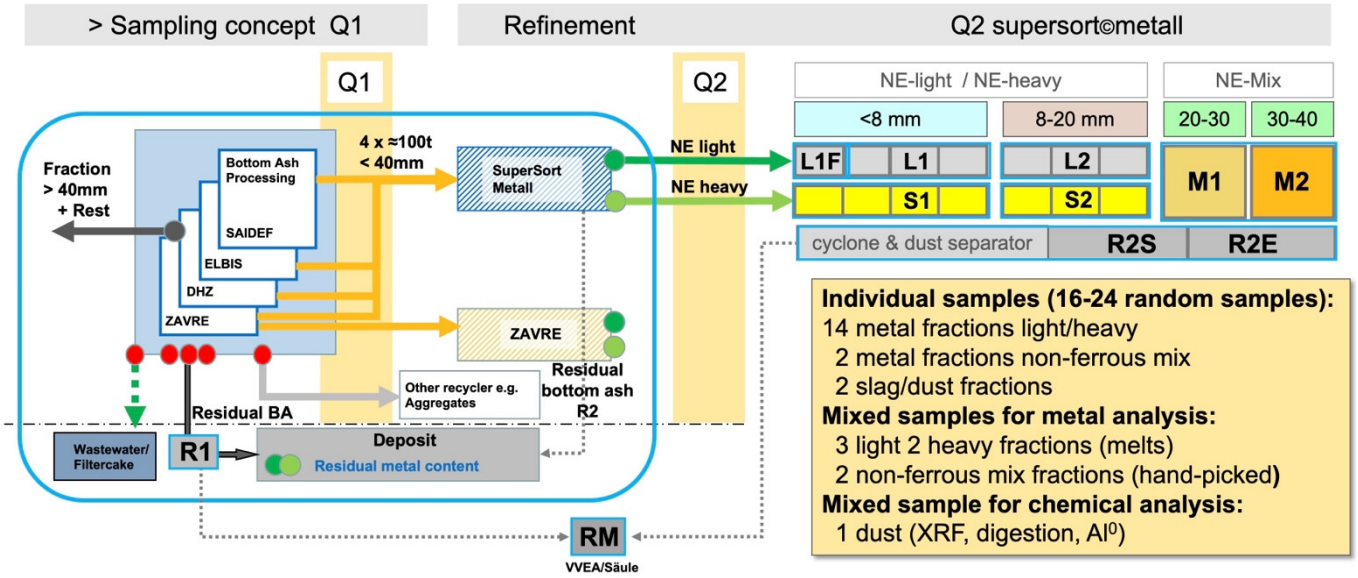

Fig. 6.1: Schematic representation of the sampling and testing concept.

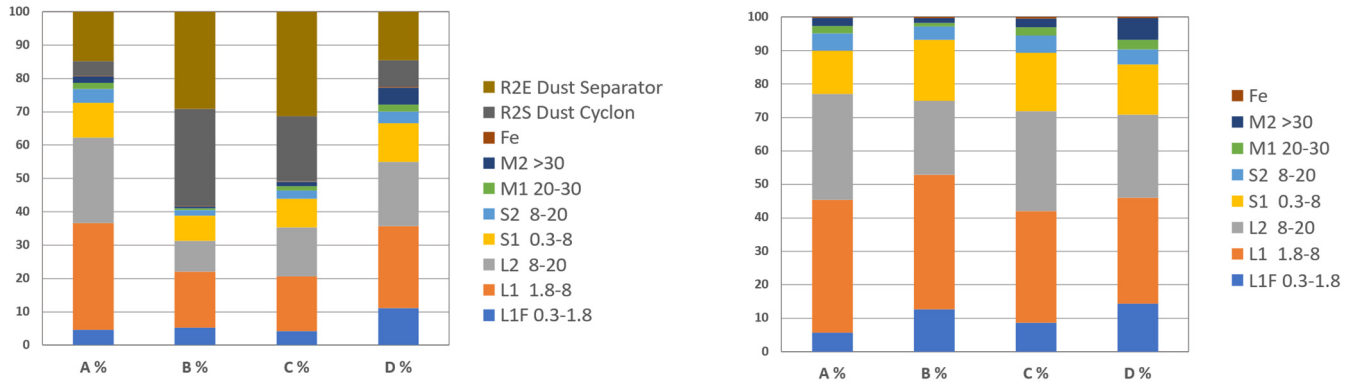

Fig. 6.2: Distribution of fractions after refining; Sx = heavy fractions, Lx = light fractions Mx = mixed fractions, R2E and R2S = non-metallic fraction separated during refinement. Right: metal distribution without mineral fraction.

In the overall balance of the plants, there are very large differences in the coarse fractions (iron parts, coils, stainless steels, etc.), and therefore the comparison of the recovery was calculated on the basis of 100 tonnes of deposited R1 bottom ash in order not to distort the comparison (Fig. 6.3). Comparatively large differences of more than 30 % can be seen.

If the recoveries in Fig. 6.3 are compared with the metals remaining in the residual bottom ashes (Fig. 6.4), it becomes clear that only aluminium is efficiently recovered (i.e., depleted in the residual bottom ashes).

It should be noted here that aluminium was determined in its metallic form by the hydrogen release method; Cu, Zn and Pb were measured chemically as total contents in the residual bottom ashes R1 and R2. In the calculation of efficiency (Fig. 6.5), the deposited metals are related to the initial total contents of the input bottom ashes. Here, the differences are much smaller and range, for example, from 59 % to 81 % for aluminium and from 36 % to 58 % for copper. This representation also largely compensates for the regionally varying initial contents of metals in the waste input and in the bottom ashes.

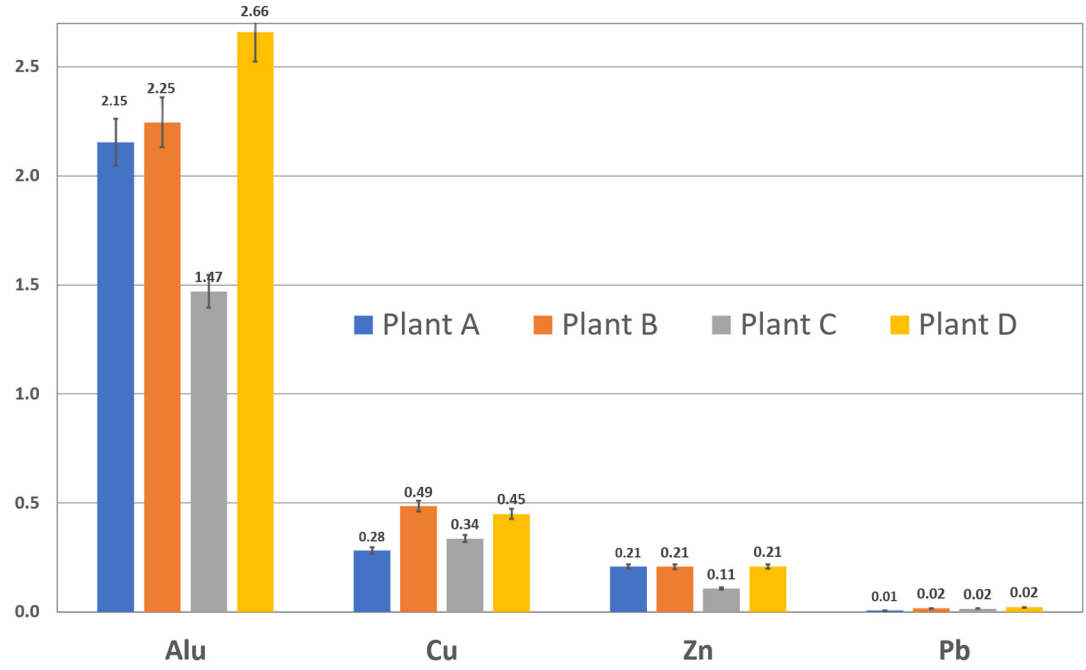

Fig. 6.3: Recovered metals, in tonnes per 100 tonnes of bottom ash deposited.

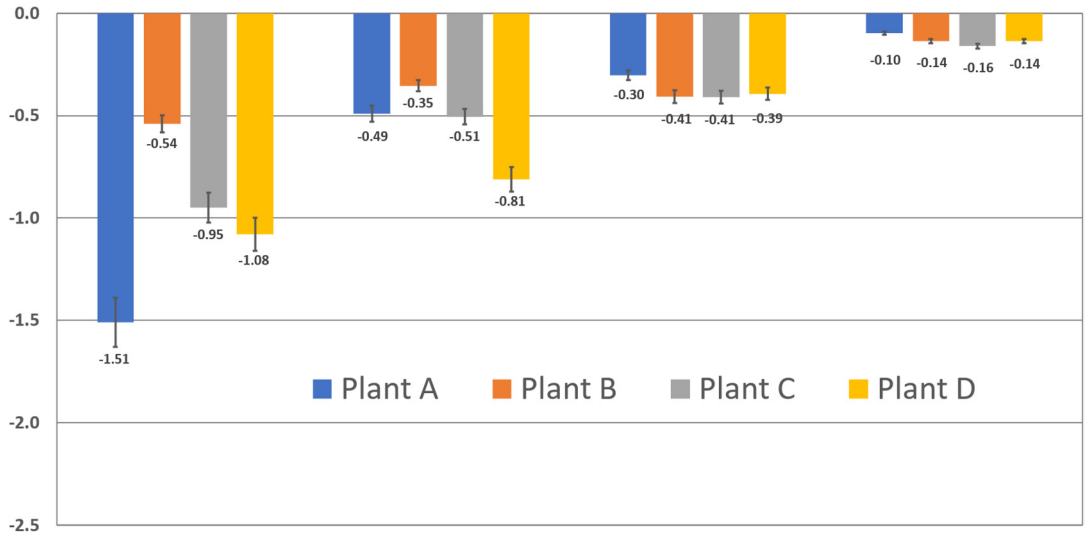

Fig. 6.4: Metals recovered in the deposited bottom ashes (Al metallic and Cu, Zn, Pb chemically determined), in tonnes per 100 tonnes of bottom ash deposited, with error estimation bars. The quantities are plotted as negative value to illustrate recovery potential.

In general, it was found that dry processing and "wet" electrodynamic fractionation produce Q1 metal fractions with very low adhesion of bottom ash components. This can be an advantage in the further refinement or sale of the Q1 fractions, but this could not be determined within the scope of this project. If, on the other hand, the recovery rate is considered in relation to the total contents, it becomes clear that processes which operate a more intensive mechanical processing with conventional separation technology in combination with a less selective Q1 metal separation (plant B) work very efficiently. Although all four plants are technically very mature and state of the art, a total of about 50% of the metals Al, Cu, Zn and Pb are still deposited unrecovered with the "depleted" bottom ash in type C landfills, and represent a potential hazard for the environment.

6.3 Mineral wastes as CO_2-neutral raw materials in clinker production

In Switzerland, an annual amount of ca. 80-90 Mio. tonnes of mineral wastes arise (Tab. 6.1.). Through recycling of mineral wastes in the sense of a circular economy, valuable primary resources and scarce landfill space can be conserved, which results in positive effects on the environment. Recycling of mineral wastes may also reduce the carbon footprint of construction materials. The main contribution to the carbon footprint of building materials such as concrete is caused by the decarbonisation of limestone in clinker production. The substitution of limestone, with *geogenic* CO_2, thus offers significant potential CO_2 savings potential: for each tonne of calcium oxide substituted by *CO_2-free* or *CO_2-neutral raw materials*, 785 kg of CO_2 can be saved.

However, the amount of limestone that can be substituted is limited by the maximum allowed SiO_2 input of the alternative raw material to meet the required lime saturation factor of the raw meal blend. Therefore, CaO-rich mineral wastes such as wood and paper ashes, as well as construction/demolition wastes with high cement paste content, offer the greatest potential to substitute limestone (Fig. 6.6). Wood and paper ashes are assumed to be *CO_2-free* as they originate from a thermal process. However, both wood and paper ashes are enormously reactive and can hydrate within a very short time and carbonate via CO_2-uptake from the air. They should therefore be considered as *CO_2-neutral* raw materials. *CO_2-neutral* raw materials are materials which are largely *CO_2-free* at the initial stage, but which incorporate CO_2 from the air within short timescales during their use, storage and processing into an alternative raw material. The short-term bound CO_2, which is emitted during clinker production, does not contribute to the greenhouse effect and should be regarded as *climate-neutral*.

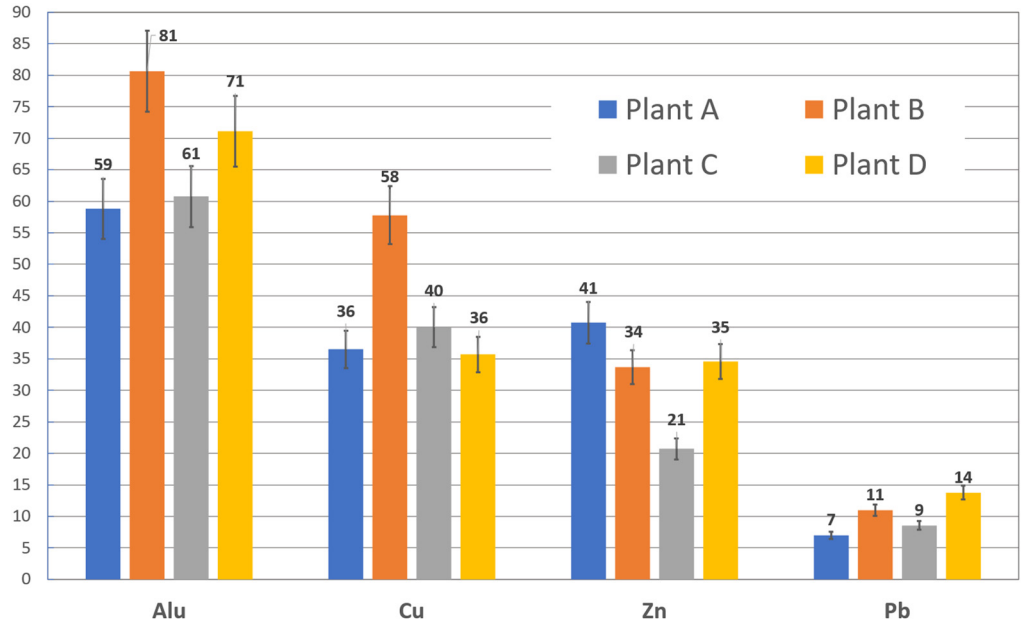

Fig. 6.5: Efficiency of metal recovery, in percent, relative to the initial metal contents of the slags with error propagation.

Tab. 6.1: Overview of the quantities of the major mineral waste streams in Switzerland and their recycling situation.

Mineral Waste	Amount (t/y)	Situation, Estimated Recycling Degrees
Excavation Material	58 Mio. t/y [1]	Estimated recovery approx. 15%, mainly for recultivation of gravel pits and other extraction sites[1]
Waste Concrete	5 Mio. t/y [2]	Processing into concrete granules; recycling of approx. 85% in recycled concrete[3]
Mixed Demolition Waste	2.4 Mio. t/y [4]	Processing into RC granules and recycling in (lean) recycled concrete or partly in the cement plant. Recycling degrees between 50-85 %[4] (regionally fluctuating)
Waste Asphalt	2.5 Mio. t/y [5]	Processing into asphalt granulate and recycling into RC asphalt (approx. 60 %)[5]
Gravel Washing Sludge	2.5 Mio. t/y [6]	Mainly used for refilling gravel pits (60%) or landfilling (30%), although great potential for agricultural applications (7%) as well as in different construction material production[6]
MSWI Bottom Ash	800‘000 t/y [7]	Recovery of metals, landfilling of the mineral fraction (85%[8]). First ongoing trials for recycling of processed fractions
Gypsum	350‘000 t/y [9]	Processing to RC gypsum only approx. 1 %; approx. 15 % remains in the cycle as mixed demolition waste, the rest is landfilled[9]
Steel Slags	170‘000 t/y [10]	No established recycling routes yet[11], possibility of recycling electric furnace slag as aggregate, coffer material, or in floor slabs
Wood Ash	75‘000 t/y [12]	Increasing utilisation of grate and bed ashes in the cement plant, estimated ca. 5%
Paper Sludge Ash	30‘000 t/y *	Almost complete utilisation of paper fly ash as a raw material substitute in the cement plant

[1]Rubli and Schneider, 2020, [2]Hiltbrunner, 2017, [3]Matasci et al., 2019, [4]Rubli, 2021, [5]Rubli, 2020, [6]Bunge, 2013, [7]Christen and Fasko, 2017, [8]Mehr et al., 2021, [9]Rubli, 2014, [10]Zeltner, 2020, [11]BAFU, 2018, [12]Fromm et al., 2021, *estimated

As of today, only the use of *CO_2-free* raw materials can be accounted for in the Swiss emissions trading system, but not the use of *CO_2-neutral* raw materials. The use of *CO_2-neutral* raw materials therefore does not result in a CO_2 reduction in the current monitoring system, or only to a limited extent. Ensuring the accountability of *climate-neutral* CO_2 in clinker production on the raw material side would create additional incentives to use secondary CaO-sources in clinker production and could represent a decisive turning point in the utilisation of mineral waste. The achieved CO_2 reduction can also lead to attribution of additional financial value to the mineral waste, which enables further investments in technologies for quality optimisation.

6.4 Influence of hydraulic effects on leachate quality of bottom ash landfills

Since the year 2000, Switzerland has committed itself to the full thermal treatment of its approximately 4 million tonnes per annum of municipal waste from industry and households. A total of 30 waste incineration plants produce around 670,000 tons of MSW bottom ash (BAFU, 2021). In thermal recycling, the focus is on reducing the pollutant hazard of the waste by destroying and/or immobilising substances (Swiss Confederation, 2023b). The bottom ash is usually quenched and discharged directly after incineration with the help of a water bath. In recent years, various Swiss plants have switched to dry discharge. The advantages of dry discharge are seen in the higher purity of the separated metal fractions. Physical treatment processes (magnetic separation, induction separation processes, etc.) enable the reduction of the residual metal content and recovery of valuable metals. The bottom ash is then temporarily stored in open landfill sites, usually for several weeks, and then placed in the landfill in layers of around 50 cm and compacted with a roller. Due to the open landfill structure, contaminated leachate is produced when infiltrating rainwater encounters the highly reactive bottom ash. This is collected in a controlled manner and discharged into the sewage system in accordance with the guidelines of the Swiss Water Protection Act (Swiss Confederation, 2023a). After completion of the bottom ash deposition in the landfill, a legally defined surface cover is applied (Swiss Confederation, 2023b).

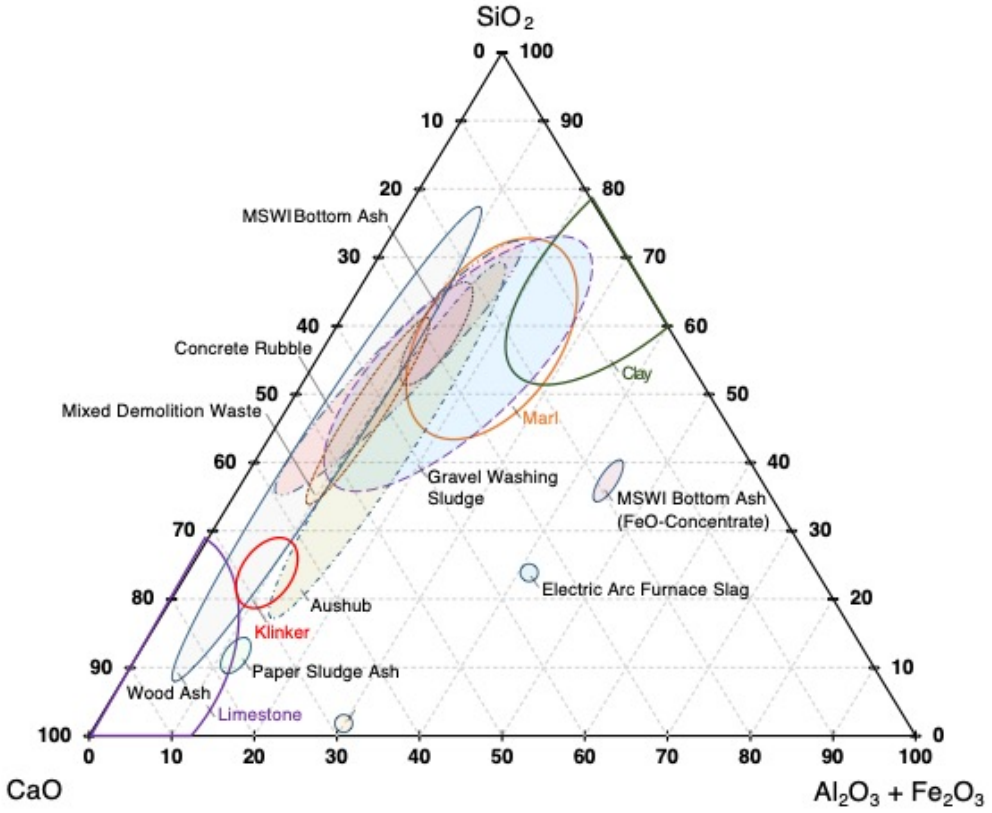

Fig. 6.6: Overview of the chemical compositions of selected mineral wastes in the pseudo-ternary system CaO-SiO_2–(Al_2O_3+Fe_2O_3). For reference, the chemical compositions of Portland cement clinker, and clinker raw materials limestone, clay and marl, are shown.

Tracer experiments have provided insights into the landfill structure, the infiltration of water, and its flow in bottom ash landfills (Fig. 6.7). The structure of a bottom ash landfill resembles a natural, layered soil. The generally horizontal structure is due to the installation technique used. The repetitive compaction of the individual installation sequences is manifested by a fine-grained compacted layer (5-15 cm), which is created by rolling. This is followed in each case by a coarse-grained, skeletally supported layer (20-35 cm), which is essentially produced by backfilling. The density of the bottom ash is about 1.50 t/m^3 and shows a porosity of 50 vol.%. The water content of the incorporated bottom ash varies as a function of weather conditions, but on average at the investigated site it is about 14.6 wt.%, while the saturated water content is about 25 wt.%. This shows that unsaturated conditions prevail in the landfill, similar to natural soils.

The use of a tracer solution allows division of the landfill body into four different hydraulic zones. The applied solution shows homogenous infiltration in the uppermost 5-10 cm of the landfill (Fig. 6.7, zone A). With increasing depth, the flow pattern becomes increasingly heterogeneous and generates locally preferential flow zones (Fig. 6.7, zone B), which show a predominantly vertical flow direction. These exhibit saturated conditions during precipitation events, resulting in high flow velocities (mm/s to cm/s). This leads to a rapid increase in leachate volume shortly after a precipitation event. Fine-grained, compacted sections form dams in which a rather homogeneous, horizontal spreading of the coloured tracer solution can be observed. Such damming systems are essential for the formation of preferential flow paths. Due to insufficient water supply from these sequences, the homogeneous flow field collapses in the coarser-grained underlying section, creating a "fingering" pattern. The stained zones are surrounded by an unstained wet zone (Fig. 6.7, zone C), which can be explained by wettin.g of the surface before the staining experiment, or by diffusive effects. With increasing distance from the preferential flow system, the water content decreases steadily until pre-test conditions with an average water content of 14.6 wt.% are reached. This part of the landfill (Fig. 6.7, zone D) is not affected by the test performed and therefore shows no change in water content.

The coloured areas (Fig. 6.7, zones A and B) occupy about 10 vol.% of the profile, while the zone influenced by the test but not coloured (Fig. 6.7, zone C) occupies about 20 vol.%. The largest part of the landfill section (approx. 70 vol.%) shows no influence by the test (Fig. 6.7, zone D).

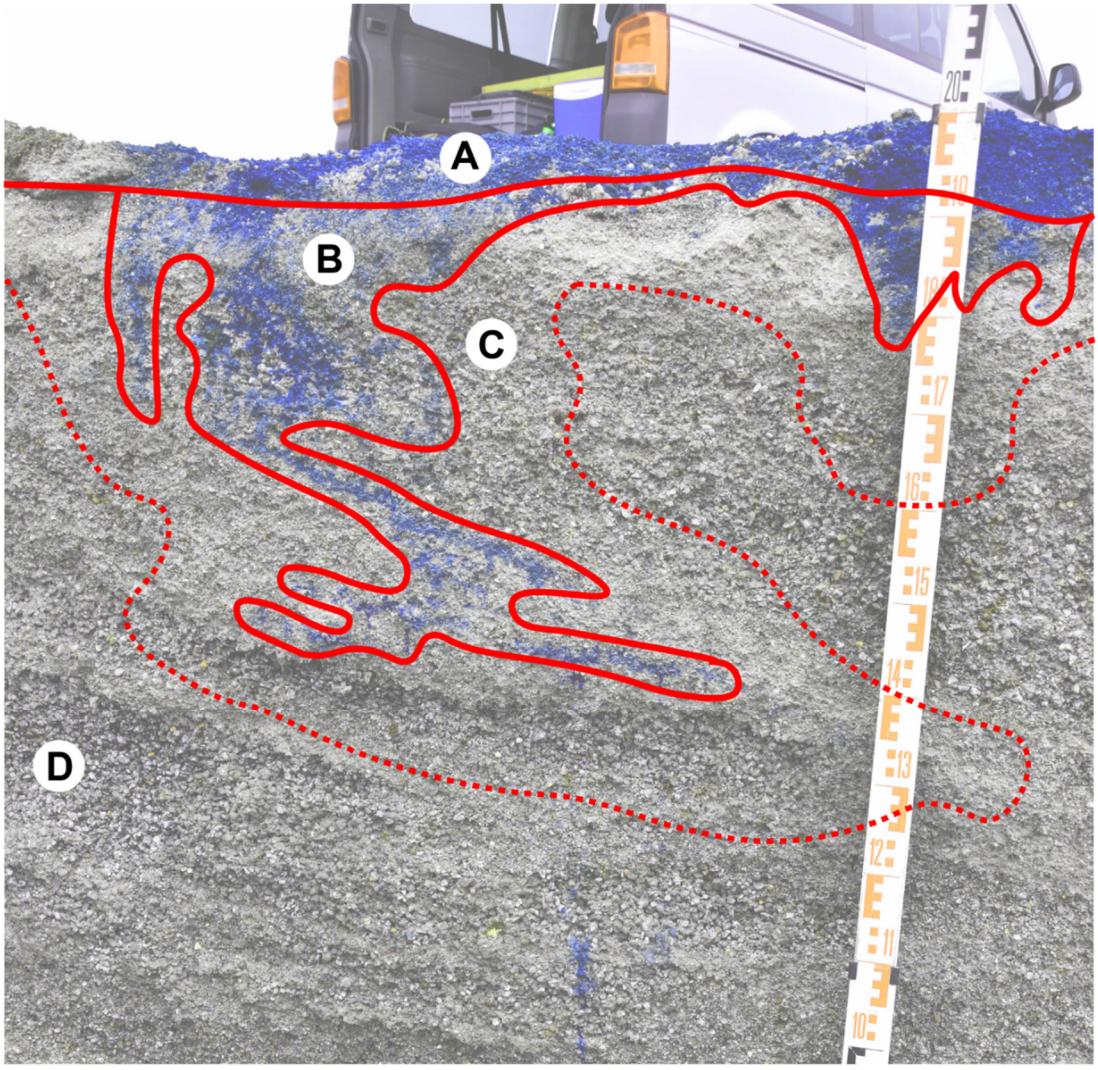

Fig. 6.7: Cross-section of a bottom ash deposit after a staining test with Brilliant Blue FCF. The different infiltration sequences and flow zones are visible. The infiltration zone (A) describes the zone localized at the surface into which the dye solution homogeneously penetrates. With increasing depth, preferential flow zones are visible (B), which are surrounded by a diffusive, moist zone (C). With increasing distance from the coloured zone, the water content decreases steadily until pre-test conditions (initial water content before application of the tracer solution) are reached, which is designated as zone D.

Leachate samples taken at two-week intervals over several months at the various landfill sites provide a comprehensive overview of the average, weather-independent pollutant concentrations after several years of bottom ash deposition (detailed data sets in (Ingold et al., 2023)). All leachates exhibit consistently alkaline pH conditions (pH 7.2-9.3) with high electrical conductivity values (LF 5.6-37.5 mS/cm). LF and pH are shown to increase during dry periods (i.e., decrease in discharge (Q)). Sodium (Na), potassium (K) and calcium (Ca) are represented as major cations, and together with chloride (Cl) and sulfate (SO_4) on the anionic side form the largest fraction of the leachate. Heavy metals and other parameters with limit values (e.g. dissolved organic carbon (DOC)) (Swiss Confederation, 2023a), contribute only a small part to the load. It is shown that heavy metals generally have low concentration values and no exceedances during moderate weather conditions, except for copper (Cu) (limit value = 0.5 mg/L), molybdenum (Mo) (limit value = 1 mg/L) and DOC (limit value = 10 mg/L) (Swiss Confederation, 2023a).

Sampling during heavy precipitation events revealed significant changes in leachate composition. Table 6.2 shows the average pollutant concentrations during the year (mean, min, max) as well as the concentrations resulting from an event at the highest runoff volume at one of the investigated landfill sites. In addition, Fig. 6.8 shows time histories of pH, LF, and Q, as well as concentrations of selected parameters during the precipitation event are shown. As the runoff volume increases, the electrical conductivity decreases, while

the pH of the leachate shows an increase. The decrease in LF is also reflected in the concentrations of the main elements (Na, K, Ca, Cl, SO_4), which decrease steadily with increasing flow. Decreasing trends are also observed for molybdenum (Mo). In contrast, numerous heavy metals such as aluminium (Al), iron (Fe), chromium (Cr), copper (Cu), lead (Pb), antimony (Sb), and zinc (Zn) show an increase in concentration with increasing flow.

The findings enable us to reveal the details of the water balance in a bottom ash landfill. While geochemical processes determine the range of concentrations in which the leachate composition lies, the hydraulic component of the system is responsible for the observed fluctuations (Johnson et al., 1999).

To explain the weather-dependent dynamics of leachate concentrations, a closer look at the pore water system in the landfill body is essential. Compared to a saturated system, unsaturated conditions, as is usually the case in bottom ash landfills, tend to allow longer residence times of the water in the landfill body (lower hydraulic conductivity). This allows for increased degrees of interaction of the bottom ash with the water, resulting in increased pollutant concentrations in the leachate. Despite this significant interaction time between water and the deposited bottom ash, a thermodynamic equilibrium of the pore waters can hardly be assumed. In this context, the degree of interaction depends largely on the hydraulic conditions in the landfill body. Thus, it can be assumed that micropore water is closer to equilibrium with the deposited bottom ash than macropore water. The capillary forces provide longer residence times, which results in a higher degree of interaction in smaller pore systems. This manifests itself in a leachate composition closer to equilibrium, for which the pH of the solution is considered the most dominant factor. Eluate tests help to describe the chemical equilibrium between bottom ash and water. Such laboratory tests show highly alkaline conditions (pH 12) (Glauser, 2021), while the pH values of the landfill leachates are in the range of 7.2-9.3. Furthermore, kinetically limited dissolution reactions of heavy metals in micropore systems are to be expected to a higher degree, since on the one hand the higher residence time leads to more interaction with the bottom ash, This is also clearly shown in the strongly increased concentration values of heavy metals in equilibrium eluate tests (Glauser, 2021). The distinction of the chemical composition of the pore waters helps to explain the increasing pH and LF values during dry phases.

Table 6.2: Average, minimum, and maximum concentration values of selected parameters in leachate at one of the investigated landfill sites. Additionally, shown are concentration values during a heavy precipitation event at maximum discharge (Q).

	Unit	Concentration or measured parameter			Heavy precipitation event
		Mean	Min	Max	
Q	L/min	12.58	9.50	15.21	824
pH	-	7.85	7.60	8.09	8.76
EC	mS/cm	22.40	19.39	26.60	6.35
Na	mg/L	4‘006	3‘496	4‘498	1‘446
K	mg/L	1‘198	1‘086	1‘325	296
Ca	mg/L	494	410	576	280
Mg	mg/L	19.4	15.0	21.5	10.8
Cl	mg/L	6‘804	5‘771	7‘683	1‘391
SO_4	mg/L	1‘910	1‘699	2‘241	999
HCO_3	mg/L	149	112	193	97.3
NO_3	mg/L	150	99.1	181	45.6
Al	mg/L	0.14	0.05	0.56	1.29
B	mg/L	1.64	1.43	2.15	0.84
Cr	mg/L	0.02	0.02	0.02	0.02
Cu	mg/L	0.04	0.03	0.06	0.02
Fe	mg/L	0.20	0.02	0.52	0.32
Mo	mg/L	1.16	1.01	1.36	0.28
Ni	mg/L	<0.01	-	-	<0.01
Pb	mg/L	0.02*	-	-	0.02
Sb	mg/L	0.06	0.05	0.08	0.06
V	mg/L	0.02	0.01	0.02	0.04
Zn	mg/L	0.05	0.02	0.14	0.08
DOC	mg/L	10.4	5.64	28.2	6.46

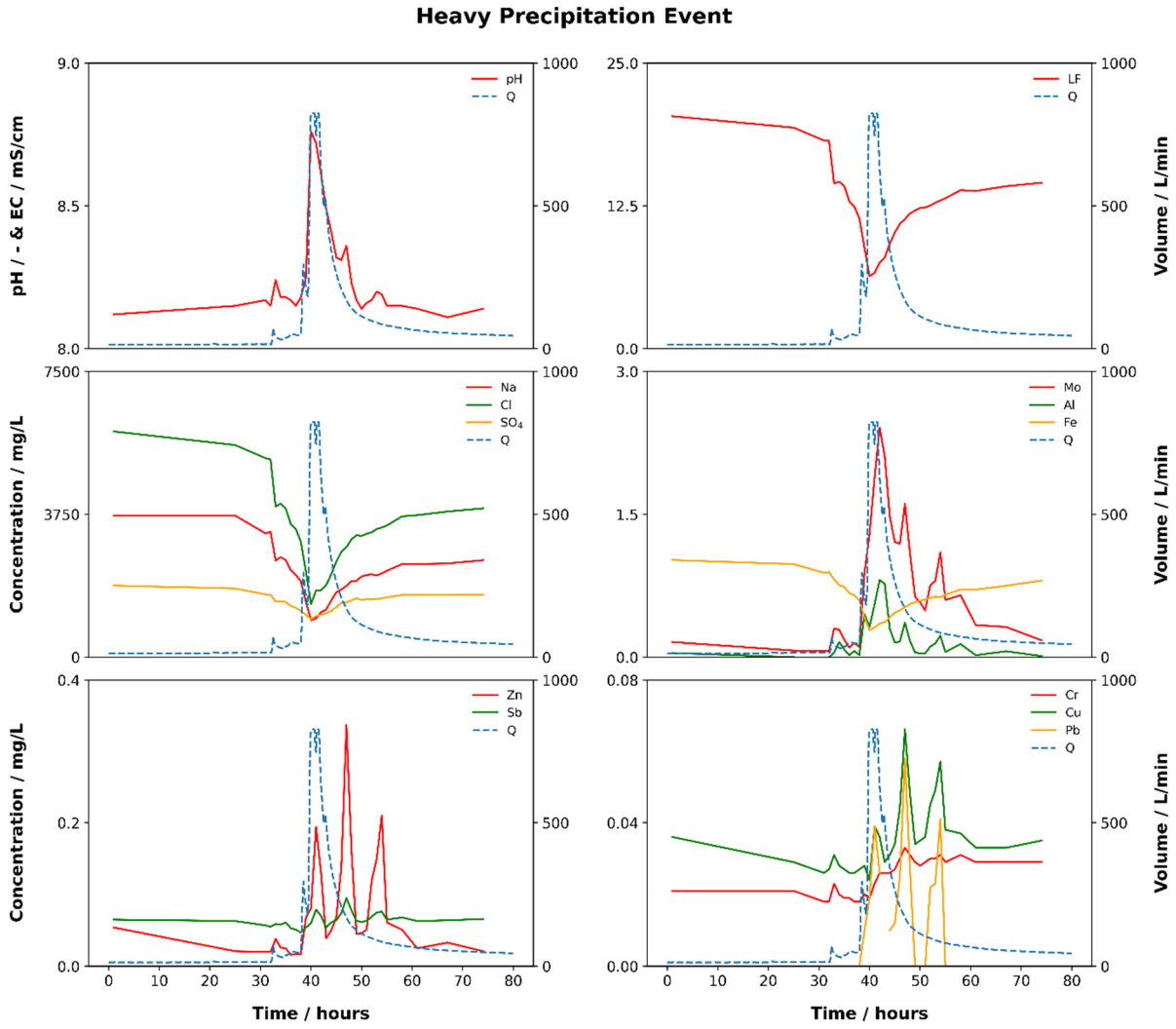

Fig. 6.8: Measured pH, conductivity (EC) and discharge (Q) values, as well as concentration curves of Na, Cl, SO_4, Mo, Al, Fe, Zn, Sb, Cr, Cu and Pb of leachate from a bottom ash landfill during a heavy precipitation event in September 2022. Hour 0 = 14.09.2022 05:00.

Decreases in the volumes draining from macropores steadily increase the proportion of micropore water in the landfill leachate, which changes the mixing ratio between the pore waters. As a consequence, the pH and concentration values of the landfill leachate in the runoff change.

Analogous to the increasing pH and LF values with decreasing runoff during dry phases, the high pH values and heavy metal concentrations during precipitation events can also be explained by the chemical composition of the pore water system and the hydraulics (Table 6.2, Fig. 6.8). With the activation of preferential flow systems during heavy precipitation events, water moves through the landfill at high flow rates under saturated conditions. Consequently, it can be assumed that this large volume of water hardly interacts with the deposited solids and thus carries low loads. As a result, the concentrations in the landfill effluent decrease and the observed dilution effects during heavy precipitation events become apparent (Fig. 6.8). This results in a decrease of the electrical conductivity as well as the decrease of the concentrations of the main elements (Na, K, Ca, Cl, SO_4). Furthermore, pore waters that have been in contact with the bottom ash for a long time are mobilised and flushed out by the water masses in the preferential flow zones. These are similar in composition to the eluate tests from laboratory investigations (Glauser, 2021) and, compared with the "average values" (Table 6.2), are characterised by similar concentration values in the main elements, but with greatly increased pH values and heavy metal concentrations. Furthermore, dissolution and desorption effects due to the preferential flow systems are possible explanations for the observed phenomena.

Our investigations show that the hydraulic aspects of a bottom ash landfill have a great impact on the leachate quality. Due to the heterogeneous nature of the landfill and the water flow, a varying degree of interaction between infiltrating rainwater and the deposited bottom ash is to be expected. An exact prediction of the pollutant load in the leachate therefore requires the inclusion of hydraulic aspects in the future development. The current leachate loads show an instantaneous picture of the meteorological, hydraulic and geochemical interaction of the landfill. In the further course of the study, an attempt is made to identify generally valid processes from the investigations of the various bottom ash dumps and to represent them with the aid of hydraulic and geochemical models. The model representation forms the basis for more precise predictions of the future development of the bottom ash landfill system.

6.5 References

Bundesamt für Umwelt, BAFU (2018)
Verwertung von Elektroofenschlacke (EOS).

Bundesamt für Umwelt, BAFU (2021)
Einheitliche Heizwert- und Energiekennzahlenberechnung der Schweizer KVA nach europäischem Standardverfahren.

Bunge R. (2013)
Abklärung zum Inventar an umweltrelevanten Schlämmen in der Schweiz 41.

Christen C., Fasko R. (2017)
Einheitliche Heizwert- und Energiekennzahlen-berechnung der Schweizer KVA nach europäischem Standardverfahren.

Fromm S., Zucha W., Schlumberger S., Eggenberger U. (2021)
Metallrückgewinnung aus Filteraschen der thermischen Altholzverwertung.

Glauser A. (2021)
Factors influencing the quality of bottom ash from municipal solid waste incineration in Switzerland. PhD Thesis, Universität Bern, Bern, 245 pp.

Hillel D., Baker R. (1988)
A descriptive theory of fingering during infiltration into layered soils. Soil Science, 146, 1, 51-56.

Hiltbrunner D. (2017)
Das Bauwerk als Rohstofflager. Swiss Bulletin for Applied Geology 22, 65–69.

Ingold P., Weibel G., Wanner C., Gimmi T., Churakov S.V. (2024)
Hydraulic and geochemical characterization of bottom ash landfills. Environmental Earth Sciences, 83, 180.

Johnson C.A., Kaeppeli M., Brandenberger S., Ulrich A., Baumann W. (1999)
Hydrological and geochemical factors affecting leachate composition in municipal solid waste incinerator bottom ash Part II: The geochemistry of leachate from Landfill Lostorf, Switzerland. Journal of Contaminant Hydrology, 40, 3, 239-259.

Johnson C.A., Schaap M.G, Abbaspour K.C. (2001)
Model comparison of flow through a municipal solid waste incinerator ash landfill. Journal of Hydrology, 243, 1-2, 55-72.

Matasci C., Gauch M., Böni H. (2019)
Material - und Energieflüsse der schweizerischen Volkswirtschaft 89.

Mehr J., Haupt M., Skutan S., Morf L., Raka Adrianto L., Weibel G., Hellweg S. (2021)
The environmental performance of enhanced metal recovery from dry municipal solid waste incineration bottom ash. Waste Management 119, 330–341.

Rubli S. (2021)
Mischabbruchverwertung in der Schweiz - Schlussbericht 2020.

Rubli S. (2020)
Modellierung der Asphaltflüsse in der Schweiz 39.

Rubli S. (2014)
Modell zur Beschreibung der Entwicklung der Gipsflüsse in der Schweiz 48.

Rubli S., Schneider M. (2020)
KAR-Modell - Modellierung der Kies-, Rückbau- und Aushubmaterialflüsse: Bezugsjahr 2018.

Zeltner C., Niederberger E., Glauser A., Eggenberger U. (2020)
Übersichtspublikation EOS-Granulat in der Schweiz • Bau und Umwelt.

7 FUNDAMENTAL ASPECTS OF MINERAL REACTIVITY AND STRUCTURAL TRANSFORMATIONS

Churakov S.V., Cametti G., Katheras A., Karalis K., Adams D.

7.1 Introduction

PSI/LES and the Institute for Geological Science at the University of Bern (UBERN/IfG) collaborate in the field of mineralogy, crystallography and environmental geochemistry. The research field of the Mineralogy group at the University of Bern covers fundamental aspects of mineral reactivity, crystal structure stability, and temperature driven phase transitions in minerals. The dedicated laboratories operated by the group are equipped with powder and single-crystal diffractometers for structural studies of minerals, and an atomic force microscopy laboratory for in-situ characterisation of mineral surfaces. The experimental studies are widely supported by modelling activities. In particular, we develop and apply numerical methods for investigation of reaction mechanisms and theoretical predictions of mineral thermodynamics. The main research activities are focused on the characterisation of mineral structure transformations in natural and synthetic microporous minerals (e.g. zeolites) as result of dehydration and cation exchange processes. These structural characterisation studies are conducted by combining single crystal X-ray diffraction experiments, spectroscopic measurements, and molecular simulations. Dedicated laboratory nucleation and re-crystallisation experiments, surface characterisation, and geochemical modelling are applied to develop sustainable strategies for heavy metal extraction from contaminated water via carbonates precipitation.

In collaboration with colleagues from University of Silesia in Poland, a new phase in apatite mineral group has been discovered and refined (see section 7.2). In collaboration with the University of Urbino Carlo Bo (Italy), the dehydration and hydration behaviour of a natural zeolite with the YUG framework type was investigated as a function of water vapour pressure and temperature by *in situ* single crystal X-ray diffraction (see section 7.3).

In the framework of an interactional project on retention of radionuclides by minerals, the surface stability and the speciation of magnetite is investigated by ab initio calculations. The obtained surface stability phase diagrams are the basis for further investigations of radionuclides absorption on magnetite surface (see section 7.4). In collaboration with the Holcim Foundation, the reactivity of ASR is investigated by ab initio molecular dynamics (see section 7.5).

Dynamic tilting in perovskite structures is responsible for their peculiar physical properties, such as superconductivity, ferroelectricity and photo-activity. An extensive analysis of the structural data for perovskites reported in recent scientific literature has been conducted to facilitate identification of the dynamic tiling phenomena. To simplify structural analysis of such systems, space groups for simple perovskites ABX_3 with dynamical octahedral tilting have been derived (see section 7.6).

7.2 Crystal structure refinement of new mineral phases in the apatite group

The apatite supergroup minerals can be described by the general formula $^{IX}M1_2{}^{VII}M2_3(^{IV}TO_4)_3X$ (Z = 2), where the Roman numbers indicate the ideal coordination number; M and T are cationic sites, and X is the anionic site. The high flexibility of the chemical composition characterises the apatite structure-type. Currently, the following elements are mentioned as the species-defining ones: $M = Ca^{2+}$, Sr^{2+}, Ba^{2+}, Pb^{2+}, Mn^{2+}, Cd^{2+}, Na^{+}, Y^{3+}, La^{3+}, Ce^{3+}, Nd^{3+}, Bi^{3+}; $T = P^{5+}$, As^{5+}, V^{5+}, Si^{4+}, S^{6+}, B^{3+}; $X = F^{-}$, $(OH)^{-}$, Cl^{-}, O^{2-} (Pasero *et al.*, 2010). In the frame of a joined project with the *Institute of Earth Sciences, Faculty of Natural Sciences, University of Silesia, Poland*, we identified a new Ba-phosphate mineral belonging to the apatite supergroup (Krzątała et al., 2023). The new phase, Fluoralforsite, was named according to the Commission on New Minerals, Nomenclature and Classification (CNMNC) recommendations for the new minerals of the apatite supergroup (Pasero et al., 2010; Hatert et al., 2013). The new mineral has been found in the rankinite-rich paralava (the holotype locality 31˚11.3' N, 35˚16.6' E) from the upper reaches of the tributary of the Wadi Zohar. The identification was conducted by applying different experimental techniques, i.e. Raman spectroscopy, SEM-EDX, and single crystal X-ray Diffraction (Krzątała et al., 2023).

The chemical analyses reveal a significant substitution of Ca^{2+}, nearly equal to one atom per formula unit. Moreover, V^{5+}, Si^{4+}, and S^{6+} occur at the tetrahedral site. Thus, the simplified and ideal formula can be written as $(Ba,Ca)_2Ba_3(PO_4)_3F$ and $Ba_5(PO_4)_3F$, respectively. Several subgroups of the $P6_3/m$ space group were tested to reveal eventual symmetry lowering due to cation ordering at the $M1$ site. However, test refinements pointed to $P6_3/m$. Based on

crystal-chemical considerations, we concluded that the ordered arrangement of Ba/Ca at the M1 site presumably occurs within individual columns (Fig. 7.1). However, the disordered distribution within adjacent columns preserves the $P6_3/m$ symmetry.

7.3 A new dehydrated topology of the small pores in zeolite YUG

The dehydration and hydration behaviour of a natural zeolite with the **YUG** framework type was investigated as a function of water vapour pressure (P_{H2O}) and temperature (T) by *in situ* single crystal X-ray diffraction. The chemical composition of the sample is $CaAl_2Si_6O_{16}{\cdot}nH_2O$, with *n* varying as a function of T and P_{H2O}. Under ambient conditions (T= 302 K and relative humidity RH = 60%) the structure contains four H_2O molecules per formula unit. After exposure to dry air for 30 minutes, 1 H_2O is released (Fig. 7.2). Prolongation of the exposure time to 60 minutes does not induces further dehydration. The H_2O can easily be taken up by exposing the crystal to ambient conditions for few minutes.

The temperature-dependent experiments were conducted under N_2 flow from 299 to 673 K, in steps of 50 K. In the investigated T range, the unit-cell volume is reduced by 13% and the space group *Pc* is maintained. Two main structural changes were observed: i) at 523 K, the release of 2.5 H_2O is accompanied by the doubling of one unit-cell parameter (*a*-axis); ii) at 573 K, the structure becomes anhydrous, the *c*-axis triples, and two T-O-T connections of the framework break, leading to the formation of an interrupted framework (Fig. 7.3). This topology (called the HT-B phase) was never reported before. Moreover, the breaking process takes place by a different mechanism compared to that reported for other zeolites, and it is here described for the first time (Cametti & Giordani, 2024).

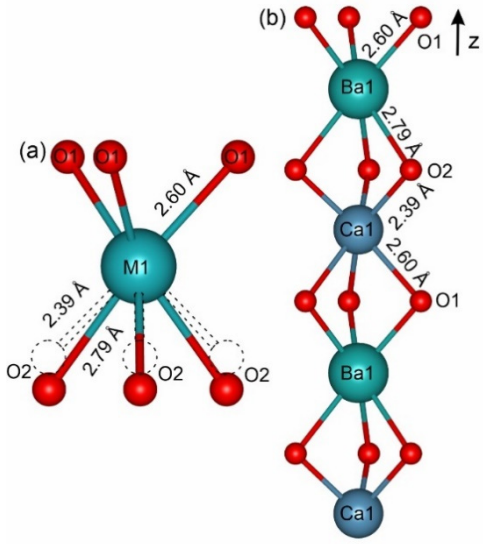

Fig. 7.1: (a) Two variants of the apatite M1 metaprism coordinated by O1 and O2, displaced off the mirror plane; (b) ordered M1 column arrangement along [001] (b). The radii proportions of Ca/Ba have been preserved.

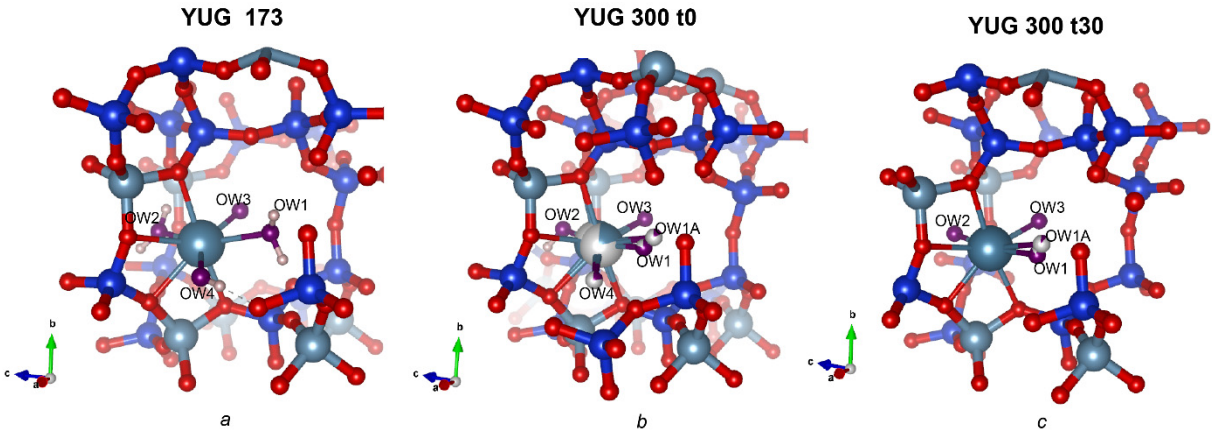

Fig. 7.2: Detail of the crystal structure of yugawaralite under different experimental conditions. a) under N_2 at 173 K; b) under dry-air flow at room temperature; c) after 30 minutes exposure to dry-air flow at room temperature. Si and Al are represented as blue and light blue spheres respectively. Ca atoms are displayed in dark cyan. Oxygen atoms of the framework are shown in red and those of the water molecules in dark purple. Light pink spheres represent hydrogen atoms. Partially coloured spheres correspond to partially occupied crystallographic sites.

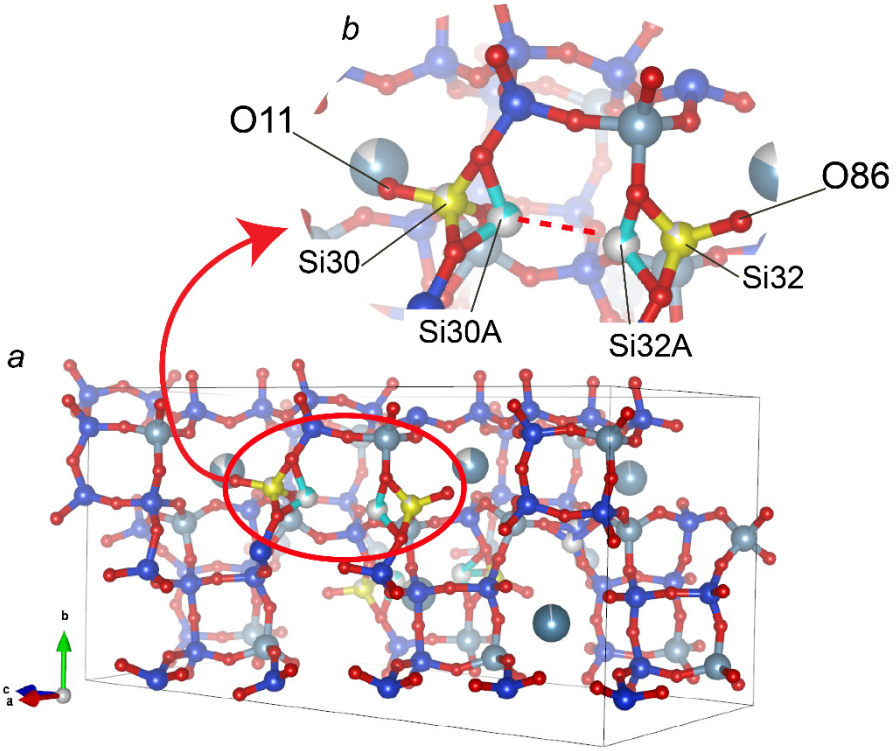

Fig. 7.3: Crystal structure of the High Temperature HT-B phase observed at 573 K during heating of yugawaralite. a) Perspective view of the unit-cell content projected along [10-0.5]. The yellow spheres represent the tetrahedral sites T (occupied by Si) originally connected and forming the 4mr in the low temperature (LT) phase. b) Magnification of the HT-B structure, highlighting the part of the framework which experiences the T-O-T breaking mechanism. Light cyan spheres represent the relic of the T sites which were connected in the HT-A phase and formed the 4mr. The two oxygen apices O11 and O86 do not connect to any Si or Al site, indicating that the framework is interrupted.

7.4 Modelling of magnetite surfaces for radionuclide retention

Magnetite, a mixed Fe(II,III) oxide Fe_3O_4, is the main corrosion product of steel in deep geological repositories. It can act as a matrix for sorption or incorporation of radionuclides, and hence contribute to the retention of these hazardous ions. Speciation, structure and stability of the most common magnetite crystal face {111} were investigated by *ab initio* simulations considering four different octahedral and tetrahedral terminations under *in situ* conditions relevant for the repository. The simulation systems were prepared as 2D slabs with two symmetric surfaces interfaced with vacuum and subject to periodic boundary conditions (Fig. 7.4). Depending on the oxidation state of the Fe atoms in the outermost surface layer, a number of hydrogen atoms and OH groups were added to impose overall charge neutrality on the system.

The speciation of the magnetite surface (structure, redox state, relaxation) strongly influences the surface reactivity and interactions with aqueous ions. Accordingly, the stability analysis of surfaces with different terminations over a wide Eh and pH range was conducted, comparing the total energies of the systems. Oct1- and Tet2-surfaces were found to be the most stable (Fig. 7.5, left). The preferential stability of the oxidised Fe cations close to the surface is in line with higher Eh values. To account for presence of the solvent, classical molecular dynamic (MD) simulations were conducted to estimate the surface-water interaction energy used to correct the stability plot for the solvent effect (Fig. 7.5, right). The preference for the octahedral termination is in line with experimental results of magnetite in water (Petitto et al., 2010) and suggested magnetite surface terminations for radionuclide sorption (Kirsch et al., 2011; Yalçıntaş et al., 2016). The obtained results (Katheras et al., 2024) further validate the computer model and allow for the detailed investigation of radionuclide sorption complexes at the magnetite (111) surface under repository conditions.

7.5 Dissolution mechanism of ASR products

Alkali-silica reaction (ASR) widely occurring in concrete is referred to as “concrete cancer”. ASR is one of the most important degradation mechanisms resulting in durability problems and premature loss of serviceability of massive concrete infrastructure (i.e., bridges, dams etc.). Despite decades of analysis of ASR and its products, ASR chemistry remains poorly understood, especially at the molecular and nanometre scale. This study aims at the understanding the ASR mechanism, which is critical and essential to predict and prevent deleterious ASR expansion behaviour and develop effective mitigation measures.

The atomistic mechanism of shlykovite surface dissolution, which shares a similar structure with crystalline ASR products, is investigated through large-scale ab initio molecular dynamic simulations using the CP2K code and reactive molecular dynamics simulations using LAMMPS. Since the dissolution of ions from mineral surfaces is a rare event with a high free energy barrier (greater than the thermal fluctuations), the MetaDynamics (MetaD) method was utilised. In this approach, the reaction progress is monitored by a set of collective variables (CVs) that accurately describe the change between reactants and products.

From the analysis of the MetaD simulations, the dissolution mechanisms of K, Si and Ca were identified, along with the activation energies for these rare events. The simulations predict that the release and incorporation of K ions in the structure has a very low activation energy whereas the dissolution mechanism of Si tetrahedra is comparable to the mechanism observed in the studies of clay minerals (Schliemann & Churakov, 2021). Furthermore, the results of the two approaches were compared, and it was found that using the ReaxFF force field, relatively accurate dissolution energies were calculated. Ultimately, we determined the swelling pressure of shlykovite concerning basal spacing when it was solvated in pure water, by employing the spring model.

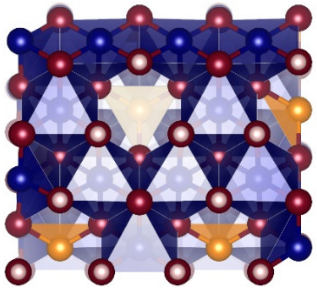

Fig. 7.4: Top view of the expected magnetite (111) termination under repository conditions including surface-water interaction. The surface shows octahedrally coordinated Fe(III) (blue) closest to the surface, O red and H white. The number of attached H can control the change of the bulk-like mixed (II,III) charged Fe in octahedral coordination; the actual H position can change the total energy of the system obtained by simulations.

7.6 Classification of perovskite structural types with dynamical octahedral tilting

A classical picture of a solid assumes that the atomic nuclei are localised at well defined minima of the potential energy. In many systems, such a minimum can be well described by a harmonic approximation. The quantum mechanical treatment of solids reveals that even in the limit of very low temperature the probability density of the nucleons is not point-like, but is extended over a finite range (Heisenberg uncertainty principle). Thermal excitations lead to the statistical occupation of higher vibrational energy levels in the corresponding discrete energy spectrum.

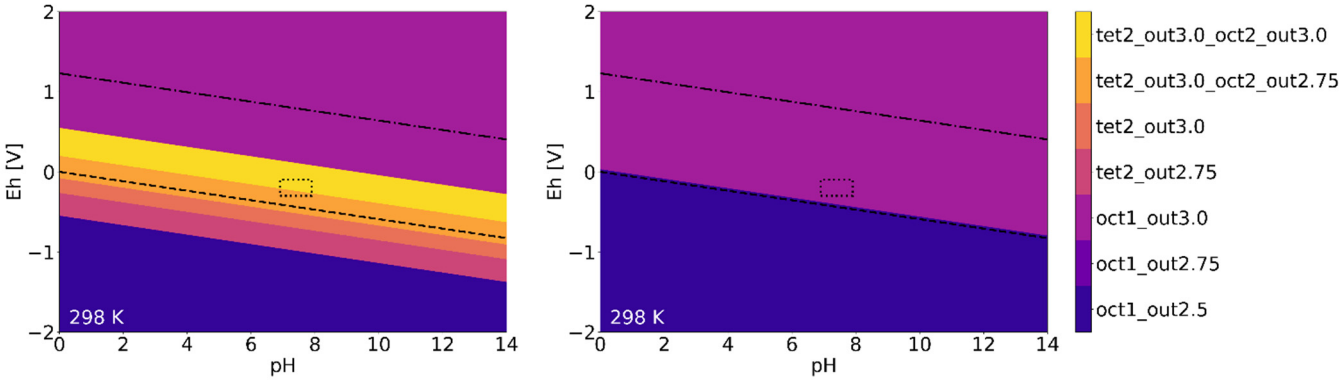

Fig. 7.5: Surface stability analysis of magnetite (111) terminations with lowest surface energy at 298 K as a function of Eh and pH. The dotted box represents the expected repository conditions. Left: Expected surface terminations based on vacuum simulations, right: with surface-water interaction obtained from classical MD.

Eventually the atomic probability density is smeared out over a broad spatial range. Perovskites ABX_3 with delocalized positions of the X atoms represent a distinct class of dynamically distorted structures with peculiar structural relations and physical properties. The delocalization originates from atoms crossing shallow barriers of the potential energy surface. Quantum mechanically, they can be treated similar to light atoms in diffusive states. Many of these perovskite structures are widely used functional materials thanks to their particular physical properties, such as superconductivity, ferroelectricity and photo-activity. A number of these properties are related to static or dynamic motion of octahedral units. However, a full understanding of the relationships between perovskite crystal structure, chemical bonding and physical properties is currently missing. Several studies indicate the existence of dynamic disorder generated by anharmonic motion of octahedral units, e.g. in halide perovskite structures.

Extensive analysis of the structural data for perovskites reported in recent scientific publications, reveals ubiquity of dynamical tilting. The structures with dynamic tilting are characterised by one of several properties such as: (a) volume increase upon a lowering of temperature, (b) apparent distortion of octahedra (where Jahn–Teller distortions can be ruled out), (c) mismatch between observed instantaneous symmetry and average symmetry, (d) deviation of the experimental space group from the theoretically predicted structures for static tilting, (e) inconsistency of lattice parameters with those suggested by the theory of static tilts, and (f) large displacement parameters for atoms at the X and B sites.

To simplify structural analysis of such systems we derive a set of space groups for simple perovskites ABX_3 with dynamical octahedral tilting (Adams & Churakov, 2023). The derived space groups extend the well established space group tables for static tiltings by Glazer (1972) & Aleksandrov (1976).

7.7 References

Aleksandrov K. (1976)
The sequences of structural phase transitions in perovskites. Ferroelectrics, 14, 801-805.

Cao C., Chong S., Thirion L., Mauro J.C., McCloy J.S., Goel A. (2017)
Wet chemical synthesis of apatite-based waste forms-A novel room temperature method for the immobilization of radioactive iodine. Journal of Materials Chemistry, A 5, 14331.

Cametti G., Giordani M. (2024)
Humidity- and temperature-dependent study of YUG type zeolite. A new dehydrated topology. Microporous and Mesoporous Materials, 263, 112811.

Hatert F., Mills S.J., Pasero M., Williams P.A. (2013)
CNMNC guidelines for the use of suffixes and prefixes in mineral nomenclature, and for the preservation of historical names. European Journal of Mineralogy, 25, 113–115.

Glazer A.M. (1972)
The classification of tilted octahedra in perovskites. Acta Cryst, B28, 3384-3392.

Katheras A.S., Karalis K., Krack M., Scheinost A., Churakov S.V. (2024)
Stability and speciation of hydrated magnetite {111} surfaces from ab initio simulations with relevance for geochemical redox processes. Environmental Science & Technology, 58 (1), 935-946.

Kirsch R., Fellhauer D., Altmaier M., Neck V., Rossberg A., Fanghänel T., Charlet L., Scheinost A. C. (2011)
Oxidation state and local structure of plutonium reacted with magnetite, mackinawite, and chukanovite. Environmental Science & Technology, 45 (17), 7267–7274.

Krzątała A, Skrzyńska K, Cametti G, Galuskina I, Vapnik Y, Galuskin E. (2023)
Fluoralforsite, $Ba_5(PO_4)_5F$ – a new apatite group mineral from the Hatrurim Basin, Negev Desert, Israel. Mineralogical Magazine, 87 (6), 866-877.

Noh J., Osman O.I., Aziz S.G., Winget P., Brédas J.-L. (2015)
Magnetite Fe_3O_4 (111) surfaces: Impact of defects on structure, stability, and electronic properties. Chemistry of Materials, 27 (17), 5856–5867.

Pasero M., Kampf A.R., Ferraris C., Pekov I.V., Rakovan J., White T.J. (2010)
Nomenclature of the apatite supergroup minerals. European Journal of Mineralogy, 22, 163–179.

Petitto S.C., Tanwar K.S., Ghose S.K., Eng P.J., Trainor T.P. (2010)
Surface structure of magnetite (111) under hydrated conditions by crystal truncation rod diffraction. Surface Science 604 (13-14), 1082–1093.

Schliemann, R., Churakov, S.V. (2021) Atomic scale mechanism of clay minerals dissolution revealed by ab initio simulations. Geochimica et Cosmochimica Acta, 293, 438-460.

Yalçıntaş E., Scheinost A.C., Gaona X., Altmaier M. (2016)
Systematic XAS study on the reduction and uptake of Tc by magnetite and mackinawite. Dalton Transactions, 45 (44), 17874–17885.

8 PUBLICATIONS

8.1 Peer reviewed research articles

Adams D.J.[1], Churakov S.V. (2023)
Classification of perovskite structural types with dynamical octahedral tilting. IUCrJ, 10, 309-320.
[1] University of Bern, Bern, Switzerland

Bernard E.[1], Nguyen H.[2], Kawashima S.[3], Lothenbach B.[1], Manzano H.[4], Provis J.L.[5,6], Scott A.[7], Unluer C.[8], Winnefeld F.[1], Kinnunen P.[2] (2023)
MgO-based cements – Current status and opportunities. RILEM Technical Letters 8, 65-78.
[1] Empa, Concrete & Asphalt Laboratory, Dübendorf, Switzerland
[2] Fibre and Particle Engineering Research Unit, University of Oulu, Oulu, Finland
[3] Department of Civil Engineering and Engineering Mechanics, Columbia University, New York, USA
[4] Department of Physics, University of the Basque Country UPV/EHU, Bilbao, Spain
[5] Department of Materials Science and Engineering, The University of Sheffield, Sheffield, United Kingdom
[6] Laboratory for Waste Management, Paul Scherrer Institut, 5232 Villigen PSI, Switzerland
[7] Department of Civil and Natural Resources Engineering, University of Canterbury, Christchurch, New Zealand
[8] Department of Mechanical, Aerospace and Civil Engineering, University of Manchester, Manchester, United Kingdom

Caron R.[1,2], Patel R.A.[1,2], Miron G.D., Le Galliard C.[3], Lothenbach B.[4], Dehn F.[1,2] (2023)
Microstructure development of slag activated with sodium silicate solution: Experimental characterization and thermodynamic modeling. Journal of Building Engineering 71, 106398.
[1] Karlsruhe Institute of Technology (KIT), Institute of Building Materials and Concrete Structures (IMB), Karlsruhe, Germany
[2] Materials Testing and Research Institute Karlsruhe (MPA), Karlsruhe Institute of Technology (KIT), Karlsruhe, Germany
[3] Department of Materials Science and Engineering, The University of Sheffield, Sheffield, United Kingdom
[4] Empa, Concrete & Asphalt Laboratory, Dübendorf, Switzerland

Cevirim-Papaioannou N.[1], Androniuk I.[1], Miron G.D., Altmaier M.[1], Gaona X.[1] (2023)
Beryllium solubility and hydrolysis in dilute to concentrated $CaCl_2$ solutions: thermodynamic description in cementitious systems. Frontiers in Nuclear Engineering 2, 1192463.
[1] Institute for Nuclear Waste Disposal, Karlsruhe Institute of Technology, Karlsruhe, Germany

Chen P., Churakov S.V., Glaus M., Van Loon L.R. (2023)
Impact of Fe(II) on ^{99}Tc diffusion behavior in illite. Applied Geochemistry, 156, 105759.

Chidiac T.J.,[1] Ukrainczyk N.[2], Prentice D.P.[3], Provis, J.L.[1,4] (2023)
Probabilistic service life prediction of alkali activated concretes exposed to chloride induced corrosion. Journal of Advanced Concrete Technology, 21(12), 1020-1035.
[1] Department of Materials Science and Engineering, The University of Sheffield, Sheffield, United Kingdom
[2] Institute of Construction and Building Materials, Technical University of Darmstadt, 64287 Darmstadt, Germany
[3] Laboratory for the Chemistry of Construction Materials, and Institute for Carbon Management (ICM), University of California, Los Angeles, USA
[4] Laboratory for Waste Management, Paul Scherrer Institut, 5232 Villigen PSI, Switzerland

He X.[1], Peng H., Zhang J.[1] (2023)
A lattice Boltzmann investigation of liquid viscosity effects on the evolution of a cavitation bubble attached to chemically patterned walls. Physics of Fluids, 35(9), 093303.
[1] State Key Laboratory of Hydraulics and Mountain River Engineering, Sichuan University, Chengdu, China

Hu G., Pfingsten W. (2023a)
Data-driven machine learning for disposal of high-level nuclear waste: A review. Annals of Nuclear Energy, 180, 109452.

Hu G., Pfingsten W. (2023b)
Machine learning-assisted heat transport modelling for full-scale emplacement experiment at Mont Terri underground laboratory. International Journal of Heat and Mass Transfer, 213, 124290.

Jäger T.[1], Keup J.[1], Prasianakis N.I., Leyer S.[1] (2023)
Theoretical and numerical constant mean curvature surface and liquid entry pressure calculations for a combined pillar–pore structure. Coatings, 13(5), 865.
[1] Faculty of Science, Technology and Medicine, University of Luxembourg, Luxembourg

Katheras A.S.[1], Karalis K.[1], Krack M.[2], Scheinost A.C.[3,4], Churakov S.V. (2024)
Stability and speciation of hydrated magnetite {111} surfaces from ab initio simulations with relevance for geochemical redox processes. Environmental Science and Technology, 58, 935-946.
[1] Institute of Geological Sciences, University of Bern, Bern, CH-3012, Switzerland
[2] Laboratory for Materials Simulations (LMS), Paul Scherrer Institute (PSI), Villigen PSI, CH-5232, Switzerland
[3] The Rossendorf Beamline (BM20), European Synchrotron Radiation Lab, Grenoble, FR-38043, France
[4] Institute of Resource Ecology, Helmholtz-Zentrum Dresden-Rossendorf, Rossendorf, Dresden, DE-01328, Germany

Kolditz O.[1,16], Jacques D.[2], Claret F.[3], Bertrand J.[4], Churakov S.V.[5,6], Debayle C.[7], Diaconu D.[8], Fuzik K.[9], Gracia D.[10], Graebling N.[1], Grambow B.[11], Holt E.[12], Idiart A.[10], Leira P.[15], Montoya V.[2], Niederleithinger E.[13], Olin M.[12], Pfingsten W.[5], Prasianakis N.I.[5], Rink K.[1], Samper J.[14], Szöke I.[15], Szöke R.[15], Theodon L.[4], Wendling J.[4] (2023)
Digitalisation for nuclear waste management: predisposal and disposal. Environmental Earth Sciences 82(1), 42.

[1] Helmholtz Centre for Environmental Research - UFZ, Leipzig, Germany
[2] Belgium Nuclear Research Centre (SCK CEN), Mol, Belgium
[3] BRGM, Orléans, France
[4] Andra, Chatenay-Malabry, France
[5] Laboratory for Waste Management, Paul Scherrer Institute, Villigen, Switzerland
[6] Institute of Geological Sciences, University of Bern, Bern, Switzerland
[7] IRSN, Fontenay-aux-Roses, France
[8] Institute for Nuclear Research Pitesti, Mioveni, Romania
[9] SSTC NRS, Kyiv, Ukraine
[10] Amphos 21, Barcelona, Spain
[11] SUBATECH (IMT Atlantique, CNRS, Nantes University), Nantes, France
[12] Technical Research Centre of Finland (VTT), Espoo, Finland
[13] Bundesanstalt für Materialforschung und -prüfung (BAM), Berlin, Germany
[14] CICA & Civil Engineering, University of A Coruña, Coruña, Spain
[15] Institute for Energy Technology (IFE), Halden, Norway
[16] Technische Universität Dresden, Dresden, Germany

Krejci P., Gimmi T., Van Loon L.R., Glaus M. (2023)
Relevance of diffuse-layer, Stern-layer and interlayers for diffusion in clays: A new model and its application to Na, Sr, and Cs data in bentonite. Applied Clay Science, 244, 107086.

Krzątała A.[1], Cametti G.[2], Galuskina I.[1], Vapnik Y.[3], Galuskin E.[1] (2023)
Gismondine-Sr, $Sr_4(Al_8Si_8O_{32})9H_2O$, a new strontium dominant, orthorhombic zeolite of the gismondine series from the Hatrurim Complex, Israel. American Mineralogist, 108, 249-258.

[1] Institute of Earth Sciences, Faculty of Natural Sciences, University of Silesia, Sosnowiec, Poland
[2] Institute of Geological Sciences, University of Bern, Bern, Switzerland
[3] Department of Geological and Environmental Sciences, Ben-Gurion University of the Negev, Beer-Sheva, Israel

Krzątała A.[1], Skrzyńska K.[1], Cametti G.[2], Galuskina I.[1], Vapnik Y.[3], Galuskin E.[1] (2023)
Fluoralforsite, $Ba_5(PO_4)_5F$ – a new apatite group mineral from the Hatrurim Basin, Negev Desert, Israel. Mineralogical Magazine, 87 (6), 866-877.

[1] Institute of Earth Sciences, Faculty of Natural Sciences, University of Silesia, Sosnowiec, Poland
[2] Institute of Geological Sciences, University of Bern, Bern, Switzerland
[3] Department of Geological and Environmental Sciences, Ben-Gurion University of the Negev, Beer-Sheva, Israel

Mazurek M.[1], Gimmi T.[1], Zwahlen C.[1], Aschwanden L.[1], Gaucher E.C.[1], Kiczka M.[1], Rufer D.[1], Wersin P.[1], Marques Fernandes M., Glaus M.A, Van Loon L.R., Traber D.[2], Schnellmann M.[2], Vietor T.[2] (2023)
Swiss deep drilling campaign 2019–2022: Geological overview and rock properties with focus on porosity and pore-space architecture. Applied Geochemistry, 159, 105839.

[1] RWI, Institute of Geological Sciences, University of Bern, 3012 Bern, Switzerland
[2] Nagra, 5430 Wettingen, Switzerland

Miron G.D., Leal A.M.M.[1], Dmytrieva S.[2], Kulik D.A (2023)
ThermoFun: A C++/Python library for computing standard thermodynamic properties of substances and reactions across wide ranges of temperatures and pressures. Journal of Open Source Software 8(83), 4624.

[1] Geothermal Energy and Geofluids Group, Institute of Geophysics, ETH Zurich, Switzerland
[2] Cosylab Switzerland GmbH, Brugg, Switzerland

Mundra S.[1], Tits J., Wieland E., Angst U.M.[1] (2023)
Aerobic and anaerobic oxidation of ferrous ions in near-neutral solutions. Chemosphere, 335, 138955.

[1] Institute for Building Materials (IfB), ETH Zurich, Stefano-Franscini-Platz 3, 8093, Zurich, Switzerland

Owusu J.P., Karalis K.[1], Prasianakis N.I., Churakov S.V. (2023)
Diffusion and gas flow dynamics in partially saturated smectites. Journal of Physical Chemistry C, 127 (29), 14425 – 14438.

[1] Institute of Geological Sciences, University of Bern, Bern, Switzerland

Poonoosamy J.[1], Obaied A.[1], Deissmann G.[1], Prasianakis N.I., Kindelmann, M.[2], Wollenhaupt B.[3], Bosbach D.[1], Curti E. (2023)
Microfluidic investigation of pore-size dependency of barite nucleation. Communications Chemistry, 6(1), 250.

[1] Institute of Energy and Climate Research (IEK-6): Nuclear Waste Management, Forschungszentrum Jülich GmbH, Jülich, 52425, Germany
[2] Ernst Ruska-Centre for Microscopy and Spectroscopy with Electrons (ER-C 2): Materials Science and Technology, Forschungszentrum Jülich GmbH, Jülich, 52425, Germany
[3] Institute of Bio- and Geosciences (IBG-1): Biotechnology, Forschungszentrum Jülich GmbH, Jülich, 52425, Germany

Qian Y.[1,2], Scheinost A.C.[3], Grangeon S.[4], Greneche J.M.[5], Hoving A.[6], Bourhis E.[7], Maubec N.[4], Churakov S.V.[1,2], Marques Fernandes M.[1] (2023)
Oxidation state and structure of Fe in nontronite: from oxidizing to reducing conditions. ACS Earth and Space Chemistry **7** (10), 1868–1881.

[1] Laboratory for Waste Management, Paul Scherrer Institut, Villigen PSI, Switzerland
[2] Institute for Geological Sciences, University of Bern, Bern, Switzerland
[3a] The Rossendorf Beamline at the European Synchrotron Radiation Facility (ESRF), Grenoble, France
[3b] Helmholtz Zentrum Dresden Rossendorf, Institute of Resource Ecology, Dresden, Germany
[4] BRGM – French Geological Survey, Orléans, France
[5] Institut des Molécules et Matériaux du Mans IMMM UMR CNRS 6283, Le Mans Université, France
[6] TNO Geological Survey of the Netherlands, TA Utrecht, the Netherlands
[7] Interfaces, Confinement, Matériaux et Nanostructures (ICMN), CNRS/Université d'Orléans, Orléans, France

Sarraf F.[1,2], Churakov S.V.[2,3], Clemens F.[1] (2023)
Preceramic polymers for additive manufacturing of silicate ceramics. Polymers, 15(22), 4360 (29 pp.).

[1] Empa-Swiss Federal Laboratories for Materials Science and Technology, Ueberlandstrasse 129, Dübendorf, CH-8600, Switzerland
[2] Institute of Geological Sciences, University of Bern, Hochschulstrasse 6, Bern, CH-3012, Switzerland
[3] Paul Scherrer Institute, Forschungsstrasse 111, Villigen, CH-5232, Switzerland

Sarraf F.[1,2], Hadian A.[1], Churakov S.V.[2,3], Clemens F.[1] (2023)
EVA-PVA binder system for polymer derived mullite made by material extrusion based additive manufacturing. Journal of the European Ceramic Society, 43(2), 530-541.

[1] Empa-Swiss Federal Laboratories for Materials Science and Technology, Ueberlandstrasse 129, Dübendorf, CH-8600, Switzerland
[2] University of Bern, Hochschulstrasse 6, Bern, CH-3012, Switzerland
[3] Paul Scherrer Institute, Forschungsstrasse 111, Villigen, CH-5232, Switzerland

Skrzyńska K.[1], Cametti G.[2], Juroszek R.[1], Schäfer C.[3], Galuskina I.[1] (2023)
New data on minerals with the **GIS** framework-type structure: gismondine-Sr from the Bellerberg volcano, Germany, and amicite and Ba-rich gismondine from the Hatrurim Complex, Israel. Mineralogical Magazine, 87(3), 443-454.

[1] University of Silesia, Faculty of Natural Sciences, Institute of Earth Sciences, Sosnowiec, Poland
[2] University of Bern, Institute of Geological Science, Bern, Switzerland
[3] Independent researcher, Untereisesheim, Germany

Van Loon L.R.[1], Bunic P.[1], Frick S.[2], Glaus M.A.[1], Wüst R.A.J.[3,4] (2023)
Diffusion of HTO, ^{36}Cl and ^{22}Na in the Mesozoic rocks of northern Switzerland. I: Effective diffusion coefficients and capacity factors across the heterogeneous sediment sequence. Applied Geochemistry, 159, 105843.

[1] Laboratory for Waste Management, Paul Scherrer Institut, 5232 Villigen, Switzerland
[2] Departement Bau, Verkehr und Umwelt, Aarau, Switzerland
[3] Nagra, 5430 Wettingen, Switzerland
[4] Earth and Environmental Science, James Cook University, Townsville, Australia

Wei X.[1,2], Pan D.[1,2], Tan Q.[2], Shi X.[2], Hou J.[2], Tang Q.[2], Xu Z.[2], Wu W.[1,2], Ma B. (2023)
Surface charge property governing co-transport of illite colloids and Eu(III) in saturated porous media. Chinese Chemical Letters, 108275.

[1] Frontiers Science Center for Rare Isotopes, Lanzhou University, Lanzhou, China
[2] School of Nuclear Science and Technology, Lanzhou University, Lanzhou, China

Wersin P.[1], Gimmi T.[1,2], Ma J.[1], Mazurek M.[1], Zwahlen C.[1], Aschwanden L.[1], Gaucher E.[1], Traber D.[3] (2023)
Porewater profiles of Cl and Br in boreholes penetrating the Mesozoic sequence in northern Switzerland. Applied Geochemistry 159, 105845.

[1] Univ Bern, Inst Geol Sci, Rock Water Interact, Baltzerstr 1, CH-3012 Bern, Switzerland
[2] Paul Scherrer Inst, Lab Waste Management, CH-5132 Villigen, Switzerland
[3] Nagra, Wettingen, Switzerland

Wieland E., Miron G.D., Ma B., Geng G.[1], Lothenbach B.[2,3] (2023)
Speciation of iron(II/III) at the iron-cement interface: a review. Materials and Structures, 56(2), 31.

[1] Department of Civil and Environmental Engineering, National University of Singapore, Singapore, Singapore
[2] Concrete & Asphalt Laboratory, Empa, Dübendorf, Switzerland
[3] Institute of Geological Sciences, University of Bern, Bern, Switzerland

Wolffers M.[1], Kulik D.A., Miron G.D., Eggenberger U.[1], Churakov S.V. (2023)
Thermodynamic model of MSWI flue gas cooling path: Effect of flue gas composition on heavy metal binding forms. Waste Management & Research, 734242X231178213.

[1] Institute of Geological Sciences, University of Bern, Bern, Switzerland

Yan Y.[1,2], Bernard E.[1], Miron G.D., Rentsch D.[3], Ma B., Scrivener K.[2], Lothenbach B.[1,4,5] (2023)
Kinetics of Al uptake in synthetic calcium silicate hydrate (C-S-H). Cement and Concrete Research, 172, 107250.

[1] Empa, Swiss Federal Laboratories for Materials Science and Technology, Laboratory for Asphalt and Concrete, Dübendorf, Switzerland
[2] EPFL STI IMX LMC, MXG 230, Lausanne, Switzerland
[3] Empa, Swiss Federal Laboratories for Materials Science and Technology, Laboratory for Functional Polymers, Dübendorf, Switzerland
[4] University of Bern, Institute of Geological Sciences, Bern, Switzerland
[5] NTNU, Department of Structural Engineering, Trondheim, Norway

Zhu X.[1], Zhang Y.[1], Chen L.[1], Wang L.[2], Ma B., Li J.[3], Poon C.S.[1,4], Tsang D.C.W.[1,2] (2023)
Bonding mechanisms and micro-mechanical properties of the interfacial transition zone (ITZ) between biochar and paste in carbon-sink cement-based composites. Cement and Concrete Composites, 139, 105004.

[1] Department of Civil and Environmental Engineering, The Hong Kong Polytechnic University, Hong Kong, China
[2] State Key Laboratory of Clean Energy Utilization, Zhejiang University, Hangzhou, China
[3] Atmospheric, Earth, and Energy Division, Lawrence Livermore National Laboratory, United States
[4] Research Centre for Resources Engineering Towards Carbon Neutrality, The Hong Kong Polytechnic University, Hong Kong, China

8.2 Technical reports

Curti E. (2023)
Aqueous Corrosion of Vitrified Nuclear Waste: Current Process Understanding, Literature Review and Recommended Rates. Nagra Arbeitsbericht NAB 23-09.

Curti E. (2023)
Bentonite Pore Waters (BPW) for SGT-E3: Model Development, Testing and Final Calculations. Nagra Arbeitsbericht NAB 23-43.

Curti E., Thoenen T., Kosakowski G., Baeyens B., Van Loon L.R., Leupin O.X[1], Martin L.[1] (2023)
The long-term geochemical evolution of the near-field of the HLW/SF repository. Nagra Technical Report NTB 23-02.

[1] Nagra, Wettingen, Switzerland

Gaucher E.[1], Aschwanden L.[1], Gimmi T., Jenni A.[1], Kiczka M.[1], Mazurek M.[1], Wersin P.[1], Zwahlen C.[1], Mäder U.[1], Traber D.[2] (2023)
TBO Bachs-1-1: Data report Dossier VIII. Rock properties, porewater characterisation and natural tracer profiles. Nagra Arbeitsbericht NAB 20-09.

[1] RWI, Institute of Geological Sciences, University of Bern, Bern, Switzerland
[2] Nagra, Wettingen, Switzerland

Glaus M.A., Frick S., Van Loon L.R. (2023)
Diffusion and retention of moderately and strongly sorbing tracers in compacted illite. Nagra Arbeitsbericht NAB 23-12.

Hummel W., Kulik D.A., Miron G.D. (2023)
Solubility limits for Bentonite Near Field (Update of NTB 14-06). Nagra Technical Report NTB 14-06.

Johnson L.[1], Curti E., Spahiu K.[1] (2023)
A Radionuclide Release Model for Spent UO_2 and MOX Fuel for Safety Assessment with Application to Waste to be Disposed of in a Deep Geological Repository in Switzerland. Nagra Arbeitsbericht NAB 23-10.

[1] Nagra, Wettingen, Switzerland

Kosakowski G. (2023)
Reactive Transport Modelling of Material Interface Evolution in the HLW Near-field. Nagra Arbeitsbericht NAB 23-33.

Kosakowski G., Churakov S.V., Glaus M.A., Typhaine G.[1], Hummel W., Kulik D.A., Ma B., Martin L.[1], Miron G.D., Prasianakis N.I. (2023)
Geochemical Evolution of the L/ILW - Near Field. Nagra Technical Report NTB 23-03.

[1] Nagra, Wettingen, Switzerland

Martin L.[1], Kosakowski G., Papafotiou A.[1], Smith P.A.[2] (2023)
Evolution of the Sealing System Porosity and its Impact on Performance. Nagra Arbeitsbericht NAB 23-21.

[1] Nagra, Wettingen, Switzerland
[2] Safety Assessment Management (Switzerland) GmbH, Klingnau, Switzerland

Prasianakis N.I., Gimmi T., Owusu J., Boiger R., Pfingsten W., Churakov S.V. (2023)
Upscaling and Uncertainty Analysis of Geological and Transport Parameters. Nagra Arbeitsbericht NAB 23-06.

Tits J., Kunz D., Lechleitner F.[1], Szidat S.[1], Guillemot T.[2] (2023)
2nd annual report of the IGD-TP Project: "LOng-term Monitoring of C-14 compounds released during corrosion of IRradiated steel" (LOMIR). IGD-TP Report 2023/Report/1, Nagra, Wettingen, Switzerland (available on request).

[1] University of Bern, Bern, Switzerland
[2] Nagra, Wettingen, Switzerland

Tits J., Wieland E. (2023)
Radionuclide Retention in the Cementitious Near-field of a Repository for Low- and Intermediate-level Waste: Development of the Cement Sorption Database. Nagra Technical Report, NTB 23-07, Nagra, Wettingen, Switzerland.

Weibel G. (2023)
Erarbeitung von Methodischen Grundlagen zur Beurteilung von Kesselaschen am Beispiel der Renergia, Renergia Zentralschweiz AG (available on request).

Wolffers M., Dörfler P., Eggenberger U. (2023)
Bestandsaufnahme der Holzaschentypen für die Verwertung im Zementwerk. On behalf of the Wyss Academy for Nature and the Federal Office for the Environment (available on request).

Wolffers M., Dörfler P., Weibel G. (2023)
Jahresbericht AWA-1 Projekt «Ersatzrohstoffe in der Kreislaufwirtschaft», Wyss Academy for Nature (available on request).

Zappatini A.[1], Eggenberger U.[1], Roth S.[2], Kündig T.[2], Evangelou M.[3] (2023)
Studie Verwertungspotential von Molasseausbruch. Im Auftrag von Amt für Abfall. Wasser, Energie und Luft, AWEL, Sektion Abfall-wirtschaft, Kt. Zürich (available on request).
[1] University of Bern, Bern, Switzerland
[2] Jäckli AG, Winterthur
[3] Eberhard Recycling AG, Kloten, Switzerland

8.3 Conferences/workshops/presentations

Cametti G. (2023)
Tracking *in situ* the structural transformations occurring in zeolites as a function of temperature. 50th Meeting "Italian Crystallographic Association", Bologna, Italy, 5-8 September 2023.

Chen Y., Miranda de Lima L., Li Z., Ma B., Lothenbach B., Yin S., Yu Q., Ye G. (2023)
Synthesis, characterization and solubility of sodium aluminosilicate hydrate (N-A-S-H) gel. 16th International Congress on the Chemistry of Cement, Bangkok, Thailand, 18-22 September 2023.

Chen P., Van Loon L.R., Koch S., Alt-Epping P., Reich T., Churakov S.V. (2023)
Reactive transport modelling of TcO_4^- diffusion in Opalinus Clay with Pflotran. 18th International Conference on the Chemistry and Migration Behaviour of Actinides and Fission Products in the Geosphere, Nantes (F), 24-29 September 2023. Poster presentation.

Claret F., Pepin G., Cances C., Kolditz O., Prasianakis N., Baksay A., Lukin D. (2023)
Development and improvement of numerical methods and tools for modelling coupled processes, Migration Conference 2023, Nantes, France, 24-29 September 2023.

Dähn R., (2023)
EURATOM PREDIS Experimental characterizations of 30-year-old radioactive waste packages and its use for the development of digital twins, DigiDECOM 2023, Helsinki, Finland, 24-26 October 2023.

Dähn R., Miron D. (2023)
WP7.4. Step towards Digital Twins, Predis annual workshop, Mechelen Belgium, 22-26 May 2023.

Di Lorenzo F., Stotskyi V., Lanson M., Scheinost A.C., Marques Fernandes M. (2023)
Understanding nickel sorption on saponite with polarized EXAFS, ROBL Workshop 2023, Dresden, Germany, 25 January 2023.

Gimmi T., Aschwanden L., Waber H.N., Gaucher E.C., Ma J., Traber D. (2023)
Profiles of $\delta^{18}O$ and $\delta^{2}H$ in porewater of a Mesozoic rock sequence: Regional variability and relation to large-scale transport regimes. EGU General Assembly, 23-28 April 2023, Vienna, Austria.

Glaus M.A., Kulik D.A., Van Loon L.R., Wüst R.A.J. (2023
Verification of new ClaySorDif model for sorption and diffusion in argillaceous media against Phreeqc results and experimental data. Abstract C2-2, Migration 2023 Conference, 25-29 September 2023, Nantes, France.

Glaus M.A., Zerva D., Van Loon L.R., Wüst R.A.J. (2023)
A sensitive method to measure geometry factors for diffusion on small samples of clay rock. 18th International Conference on the Chemistry and Migration Behaviour of Actinides and Fission Products in the Geosphere, Nantes (F), 24-29 September 2023. Poster presentation.

Gysi A., Hurtig N., Ruiguang P., Harlov D., Miron G.D., Kulik D. (2023)
Ore-forming processes and metasomatism: combining experimental and modeling methods to interpret field observations 2-DAY IN-PERSON WORKSHOP, Goldschmidt conference, 9-14 July, Lyon, France.

Hu G., Pfingsten W. (2023)
Investigation of machine learning assisted thermal-hydraulic processes in FE experiment at Mont Terri URL. EURAD MODATS Work Package Annual Meeting 5, September 19-September 21, Leuven, Belgium.

Hu G., Pfingsten W. (2023)
Machine learning-assisted heat transport modelling for full-scale emplacement experiment at Mont Terri underground laboratory. EURAD MODATS Work Package Workshop 4, February 1-2, Baden, Switzerland.

Hu G., Pfingsten W. (2023)
Summary of progress in Sub-Tasks 2.2, 2.3 and 2.4 FE experiment/Mont Terri. EURAD MODATS Work Package Annual Meeting 3, May 29-June 3, Helsinki, Finland.

Hu G., Prasianakis N., Pfingsten W. (2023)
Comparison of physical informed neural network and other machine learning methods for simulating heat transport in a nuclear waste disposal system. Goldschmidt 2023 Conference, July 9-15, Lyon, France.

Ingold P., Weibel G.. (2023)
Einfluss von hydraulischen Effekten auf die Sickerwasserqualität von Schlackendeponien in der Schweiz In: Berliner Konferenz Mineralische Nebenprodukte und Abfälle (pp. 296-303). Thomé-Kozmiensky Verlag GmbH, 12 June 2023.

Jacques D., Kolditz O., Szoke I., Churakov S.V., Garcia D., Laloy E., Montoya V., Prasianakis N.I., Samper J. (2023)
Digitalization and digital twins in long term management of radioactive waste, International Conference on Environmental Remediation and Radioactive Waste ICEM 2023, Stuttgart, Germany, 3-6 October 2023.

Jacques D., Kolditz O., Szoke I., Churakov S.V., Garcia D., Laloy E., Montoya V., Prasianakis N.I., Samper J. (2023)
A glance to the future digitization and digital twins in long term management of radioactive waste, EURAD ACED-DONUT Workshop: Assessing the long term evolution of engineered barrier systems of waste disposal systems, Mechelen, Belgium, 8-10 November 2023.

Jenni A., Gimmi T., Mäder U. (2023)
Coupling of porosity and transport at highly reactive cement interfaces: Open issues. 6th International Workshop on Mechanisms and Modelling of Waste / Cement Interactions, 20-24 November 2023, Prague, Czech Republic.

Jenni A., Mäder U., Gimmi T. (2023)
Electrostatic effects and reactive transport in different clay materials: observations and modelling approaches. Goldschmidt 2023, 9-13 July 2023, Lyon, France.

Katheras A.S., Karalis K, Krack M., Scheinost A.C., Churakov S.V. (2023)
Ab initio modelling of magnetite surfaces for plutonium retention. AcE methods Workshop, Dresden, Germany, 20-22 March 2023.

Katheras A.S., Karalis K, Krack M., Scheinost A.C., Churakov S.V. (2023)
Ab initio modelling of magnetite surfaces for radionuclide retention. Goldschmidt Conference Lyon, France, 09-14 July 2023.

Katheras A.S., Karalis K, Krack M., Scheinost A.C., Churakov S.V. (2023)
Magnetite surface modelling for radionuclide retention. Decay Days, Braunschweig, Germany, 26-29 September 2023.

Kolditz O., Jacques D., Claret F., Garcia D., Montoya V., Churakov S.V., Prasianakis N.I., Samper J., Nagel Th., Idiart A., Simo E., Ziefle G. (2023)
Model development and application to European radioactive waste disposal within EURAD, Second International DEvelopment of COupled models and their VALidation against EXperiments Symposium, DECOVALEX 2023, Troyes, France, 14-16 November 2023.

Kosakowski G. (2023)
Waste package modelling with a mixing tank approach, EURAD ACED-DONUT Workshop: Assessing the long term evolution of engineered barrier systems of waste disposal systems, Mechelen, Belgium, 8-10 November 2023.

Kosakowski G. (2023)
Modeling waste Package evolution and gas generation. Special Seminar at Kochi University, 6 October 2023, Kochi, Japan.

Krejci P., Gimmi T., Van Loon L.R., Glaus M.A. (2023)
Relevance of diffuse-layer, Stern-layer and interlayer transport in diffusion experiments with various clays and ions. Goldschmidt2023, 9-13 July 2023, Lyon, France.

Kulik D.A., Glaus M.A., Gimmi T., Van Loon L.R., Wüst R.A.J. (2023)
ClaySorDif: A new model for radionuclide sorption and diffusion in argillaceous media (GEMS implementation and verification against Phreeqc results and experimental data). 18th International Conference on the Chemistry and Migration Behaviour of Actinides and Fission Products in the Geosphere, Nantes (F), 24-29 September 2023. Oral presentation.

Kulik D.A., Glaus M.A., Gimmi T., Van Loon L.R., Wüst R. (2023)
GEMS implementation of an integrated ClaySorDif model for radionuclide sorption and diffusion in argillaceous media. Abstract C2-2, Migration 2023 Conference, 25-29 September 2023, Nantes, France.

Latimer S, Provis J.L., Butcher E. (2023)
Learning from multi-decade aged cement samples. 6th International Workshop on Mechanisms and Modelling of Waste / Cement Interactions, 20-24 November 2023, Prague, Czech Republic.

Lothenbach B., Nedyalkova L., Tits J., Wieland E., Rojo H., Mäder U. (2023)
Modelling Se(IV) and Se(VI) sorption on AFm phases. 6th International Workshop on Mechanisms and Modelling of Waste / Cement Interactions, 20-24 November 2023, Prague, Czech Republic.

Macé N., Fayette E., Tits J., Kunz D., Bleyen N. (2023)
Effect of cellulosic degradation products onto radionuclide transport in cementitious matrices. 6th International Workshop on Mechanisms and Modelling of Waste / Cement Interactions, 20-24 November 2023, Prague, Czech Republic.

Mazurek M., Gimmi T. (2023)
Clay Club project CLAYWAT: Interaction of water and minerals in the nanometric pore space of clays and shales. Meeting of the NEA Integration Group for the Safety Case (IGSC), October 2023 (virtual, pre-recorded).

Miron G.D., Kulik D.A., Wüst R. (2023)
The PSI chemical thermodynamic database TDB 2020 to support Nagra safety assessments for deep geological repository. Abstract PC1-6, Migration 2023 Conference, 25-29 September 2023, Nantes, France.

Miron G.D., Lothenbach B., Kulik D.A. (2023)
Thermodynamic Modeling of cementitious systems: Cemdata18, CemGEMS, ongoing C-(A)-S-H model development, and integration with THEREDA. AKB-Workshop „Zementbasierte Verschlussbauwerke im Salinar“, 5-7 September 2023, Braunschweig, Germany.

Miron G.D., Marinich O., Marques Fernandes M., Kulik D.A., Baeyens B., Wüst R. (2023)
The optimized GEMS ClaySor Model and databases to support Nagra safety assessments for a deep geological repository. Abstract A5-12, Migration 2023 Conference, 25-29 September 2023, Nantes, France.

Mokos A., Peng H., Miron G.D., Kulik D.A., Griffa M., Ma B., Prasianakis N.I., Churakov S.V. (2023)
Pore-level modelling of cement paste degradation due to cement-clay interaction. Goldschmidt 2023, Lyon, France, 9-14 July 2023.

Mokos A., Prasianakis N.I., Churakov S.V. (2023)
Lattice Boltzmann simulations of cementitious materials. MAGIC Task 3 Annual Meeting, 11 January 2023.

Mundra S., Tits J., Wieland E., Angst U.M. (2023)
The fate of ferrous ions in corroding steel reinforced concretes. 16th International Congress on the Chemistry of Cement, Bangkok, Thailand, 18-22 September 2023.

Peng H., Rajyaguru A., Curti E., Grolimund D., Churakov S.V., Prasianakis N.I. (2023)
Digital Twin of Crystallization in Porous Media: An Integrated Physics-based Machine-Learning Framework for inverse modeling of mass transport processes. CrysPom VIII - The 8th International Workshop on Crystallization in Porous Media, Ghent, Belgium, 13-15 June 2023.

Peng H., Rajyaguru A., Curti E., Grolimund D., Churakov S.V., Prasianakis N.I. (2023)
Towards Digital Twin of Counter-Diffusion Experiments: An Integrated Physics-based Machine-Learning Framework for Reactive Transport Simulations. Goldschmidt 2023, Lyon, France, 9-14 July 2023.

Pfingsten W. (2023)
Reactive transport modelling within a statistical framework to quantify sorption parameter uncertainties for Ni diffusion in clay. Goldschmidt 2023 Conference, July 9-15, Lyon, France.

Pfingsten W., Hu G. (2023)
Data-driven model for full-scale emplacement experiment at Mont Terri underground laboratory. EURAD Third Annual Meeting, March 13-16, Larnaca, Cyprus.

Poonoosamy J., Lönartz M.I., Yang Y., Deissmann G., Kosakowski G., Bosbach D. (2023)
Reactive transport modeling for assessing coupled hydrogeochemical processes at interfaces in deep geological repositories: from the laboratory to the real world. Safety of Nuclear Waste Disposal, 2, 123–124.

Poonoosamy J., Obaeid A., Curti E., Prasianakis N., Deissmann G., Churakov S.V., Bosbach D. (2023)
Towards a process-based model describing transport induced co-precipitation and radionuclide retention. Lab on chip experiments and reactive transport modelling diagnostics (invited), Migration Conference 2023, Nantes, France, 24-29 September 2023.

Poonoosamy J., Obaeid A., Kaspor A., Curti E., Prasianakis N., Deissmann G., Bosbach D. (2023)
Developing a process-based model describing transport-induced co-precipitation and retention of radionuclides (invited), American Geophysical Society annual meeting, AGU 2023 San Francisco, CA, USA, 11-15 December 2023.

Poonoosamy J., Prasianakis N., Curti E., Deissmann G., Bosbach D. (2023)
A lab on a chip concept for rationalizing hydro-geochemical processes at the pore scale. Interpore 2023, Edinburgh, Scotland 22-25 May 2023.

Prasianakis N. (2023)
Machine Learning enhanced scientific computing and modelling, 2-4-6 October 2023, Tokyo University, Hiroshima University, Kochi University, Japan.

Prasianakis N.I., Laloy E., Jacques D., Meeussen J.C.L., Tournassat C., Miron G.D., Kulik D. A., Idiart A., Demirer E., Cochepin B., Leconte M., Savino M., Marques-Fernandes M., Samper J. II, De Lucia M., Yang C., Churakov S.V., Montoya V., Samper J., Kolditz O., Claret F. (2023)
Geochemistry and Machine Learning benchmark within EURAD joint project, Migration Conference 2023, Nantes, France, 24-29 September 2023.

Prasianakis N.I., Laloy E., Jacques D., Meeussen J.C.L., Tournassat C., Miron G.D., Kulik D.A., Idiart A., Demirer E., Cochepin B., Leconte M., Savino M., Marques-Fernandes M., Samper J. II, De Lucia M., Yang C., Churakov S.V., Samper J., Kolditz O., Claret F. (2023)
Overview of the geochemistry and machine learning benchmark within EURAD Joint Project, EURAD ACED-DONUT Workshop: Assessing the long term evolution of engineered barrier systems of waste disposal systems, Mechelen, Belgium, 8-10 November 2023.

Qian Y., Scheinost A.C., Grangeon S., Hoving A., Greneche J.M., Churakov S.V., Marques M.M. (2023)
Retention of redox-sensitive Tc and Se on Fe-bearing clay minerals. ROBL workshop, Helmholtz-Zentrum Dresden-Rossendorf (HZDR), Germany, 25 January 2023.

Qian Y., Scheinost A.C., Grangeon S., Hoving A., Greneche J.M., Churakov S.V., Marques M.M. (2023)
Retention of redox-sensitive Tc and Se on Fe-bearing clay minerals. EURAD 3rd Annual Event, Larnaca, Cyprus, 14-16 March 2023.

Stefanini L., Ansari D., Walkley B., Provis J.L. (2023)
Characterisation of calcined waste clays and utilisation in alkali-activated blends with GGBFS. 42nd Cement and Concrete Science Conference, London, UK, 11-12 September 2023.

Stotskyi V., Di Lorenzo F., Marques Fernandes M., Krack M., Scheinost A.C., Lanson M., Lanson B., Churakov S.V. (2023)
Molecular scale understanding of Ni^{2+} adsorption on swelling clay minerals. Goldschmidt Conference 2023, Lyon, France, 9-14 July 2023.

Stotskyi V., Di Lorenzo F., Marques Fernandes M., Krack M., Scheinost A.C., Lanson M., Lanson B., Churakov S.V. (2023)
Molecular scale understanding of Ni^{2+} adsorption on swelling clay minerals. Migration Conference 2023/18th International Conference on the Chemistry and Migration Behaviour of Actinides and Fission Products in the Geosphere, Nantes, France, 24-29 September 2023.

Tits J., Curti E., Laube A., Wieland E. (2023)
Sorption of ^{32}Si and ^{45}Ca by isotopic exchange during recrystallisation of cement phases. 6th International Workshop on Mechanisms and Modelling of Waste / Cement Interactions, 20-24 November 2023, Prague, Czech Republic.

Tits J., Kunz D. (2023)
Heterogeneous hydrolytic degradation of cellulose and stability of ISA under alkaline, reducing conditions. EURAD – CORI Annual Workshop, Barcelona, Spain, 09-11 May, 2023.

Tits J., Kunz D., Salazar G., Rauber M., Lechleitner F., Szidat S., Wieland E., Guillemot T. (2023)
Long-term monitoring of C-14 compounds released during corrosion of irradiated steel. Lomir Annual Meeting, Nagra, Wettingen, Switzerland, 15.05.2023.

Vehling F., Kosakowski G., Shao H. (2023)
Two phase reactive transport modelling of heterogeneous gas production in low and intermediate level radioactive waste repository, EURAD ACED-DONUT Workshop: Assessing the long term evolution of engineered barrier systems of waste disposal systems, Mechelen, Belgium, 8-10 November 2023.

Wei X., Glaus M.A., Van Loon L.R., Marques Fernandes M., Ma B. (2023)
Zinc(II) transport in compact illite in the presence of organic ligands. 18th International Conference on the Chemistry and Migration Behaviour of Actinides and Fission Products in the Geosphere, Nantes (F), 24-29 September 2023. Poster presentation.

Weibel G., Ingold P., Kämpfer P. (2023)
FSSR-Lab Verbrennungsrückstände. Universität Bern, 17. November 2023.

Weibel G., Wolffers M. (2023)
Workshop Sekundärrohstoffe in Betonanwendungen mit Fokus KVA-Schlacke, Universität Bern, 20. October 2023.

Wolffers M., Häseli U., Dörfler P., Weibel G., Eggenberger U. (2023)
Mineralische Abfälle als CO_2-neutrale Rohmaterialien in der Klinkerproduktion. In: Berliner Konferenz Mineralische Nebenprodukte und Abfälle (pp. 258-269). Thomé-Kozmiensky Verlag GmbH, 12 June 2023.

Wolffers M., Weibel G. (2023)
Urban Mining. In: Fokus Forschung-Podcast #3: Urban Mining. Universitätsbibliothek Bern.

Wüst R.A.J., Van Loon L.R., Glaus M.A., Kulik D.A., Marques Fernandes M., Li X. (2023)
Approach of handling the sorption and diffusion heterogeneity across the Opalinus Clay and adjacent confining units in the safety case for the Swiss deep geological repository. 18th International Conference on the Chemistry and Migration Behaviour of Actinides and Fission Products in the Geosphere, Nantes (France), 24-29 September 2023. Oral presentation.

Yang Y., Patel R., Deissmann G., Prasianakis N.I., Churakov S.V., Poonoosamy J., Bosbach D. (2023) Pore-scale modelling of solute transport in partially and fully saturated porous media, EURAD ACED-DONUT Workshop: Assessing the long term evolution of engineered barrier systems of waste disposal systems, Mechelen, Belgium, 8-10 November 2023.

Zerva D., Glaus M.A., Churakov S.V. (2023)
Diffusion and retention of divalent transition metal tracers in compacted illite converted to different cationic forms. 18th International Conference on the Chemistry and Migration Behaviour of Actinides and Fission Products in the Geosphere, Nantes (France), 24-29 September 2023. Poster presentation.

Zhan B., Baral A., Provis J.L., Hanein T. (2023) Evaluating the thermodynamic properties of iron-containing siliceous hydrogarnet. 42nd Cement and Concrete Science Conference, London, UK, 11-12 September 2023.

Zwahlen C., Gimmi T., Jenni A., Kizcka M., Mazurek M., Van Loon L.R., Mäder U., Traber D. (2023) Chloride accessible porosity fractions across the Jurassic sedimentary rocks of northern Switzerland. Goldschmidt2023, 9-13 July 2023, Lyon, France.

8.4 Invited Talks

Cametti G. (2023)
Tracking *in situ* the structural transformations occurring in zeolites as a function of temperature. 50th Meeting "Italian Crystallographic Association", Bologna, Italy, 5-8 September 2023. (Key Note Lecture).

8.5 Teaching

Cametti G.
Bachelor Course: Einführung in Röntgenmethoden, Universität Bern, Fall semester.

Cametti G.
Master Course: Natural Zeolites, Universität Bern, Fall semester.

Cametti G.
Master Block Course: Single Crystal X-Ray Diffraction, Universität Bern, Spring semester.

Churakov S.V., Di Lorenzo F.
Master Course: Mineral Surface Characterization with AFM, Universität Bern, Fall semester 2023.

Churakov S.V.
Bachelor Course: Kristallographie I+II,
Universität Bern, Spring and Fall semester.

Churakov S.V.
Bachelor Course: Kristalloptik, Universität Bern, Fall semester.

Churakov S.V.
Master Course: Atomistic simulations of fluids and solids, Universität Bern, Fall semester.

Eggenberger U., Wolffers M., Gfeller F.
Master Course: X-Ray Powder Diffraction, Universität Bern, Spring semester 2023.

Eichler R., Churakov S.V., Leupin O., Robers L.
Master Course: Fuel Cycle and Waste Management, ETH Zürich, Spring semester 2023.

Gimmi T., Alt-Epping P.
Master Course: Geochemical Modelling II: Reactive Transport, Universität Bern, Spring semester 2023.

Kosakowski G.
Master Course: Geostatistics, Universität Bern, Spring semester 2023.

Kosakowski G.
Master Course: Chemical modelling of cement degradation, Civil and Environmental Engineering Program, Graduate. School of Advanced Science and Engineering, Hiroshima University, 21-27 September 2023.

Prasianakis N.I., Churakov S.V.
Master Course: Pore scale reactive transport simulation in porous and fractured media, Universität Bern, Spring semester 2023.

Weibel G., Wolffers M.
Master Excursion: From Waste to Resources and the Challenges in Between, Universität Bern, Spring semester 2023.

Weibel G., Wolffers M.
Master Course: Geochemical Analysis of Rocks, Universität Bern, Fall semester 2023.

Wolffers M., Weibel G.
Master Course: Waste Materials & Circular Economy, Universität Bern, Fall semester 2023.

8.6 PhD thesis defences

March 2023: Philipp Krejci
Diffusion of sorbed cations in clays: Development, improvement and application of new and existing models.

August 2023: Jerry Peprah Owusu
Numerical simulations of gas transport in argillaceous rocks: A molecular dynamics and pore-scale simulation study.

September 2023: Fateme Sarraf
Fabrication of dense polymer derived mullite ceramics by fused deposition modelling (FDM) method.

October 2023: Ping Chen
Technetium retention and migration in clay systems in presence of iron.

8.7 Outreach

Boiger R., Modini R. (2023)
Retrieval of aerosol properties from in situ, multi-angle light scattering measurements using invertible neural networks, Online Talk, LEAP ML Climate Journal Club, 25 May, 2023.

Dörfler P., Gfeller F., Wolffers M. (2023)
Mein abc ist sekundär [Exhibition]. In: Mein abc ist sekundär. Sitterwerk, St. Gallen. 8.6-30.6.2023.

Provis J.L. (2023)
Global developments in the drive for carbon net-zero cement production, NDA Sustainability Week “Lunch and Learn” seminar, Nuclear Decommissioning Authority, UK, 12 September 2023.

Provis J.L. (2023)
Can we focus cements research to benefit both the environment and human development?, Seminar, Institute of Geological Sciences, University of Bern, 6 November 2023.

Weibel G. (2023)
Den Überblick behalten! Welche Massenströme mit welchen Materialqualitäten gelangen auf unsere Deponien. Waste Vision, 8.9.2023.

Paul Scherrer Institut :: Forschungsstrasse 111 :: 5232 Villigen PSI :: Switzerland :: Tel. +41 56 310 21 11 :: www.psi.ch